論文 / 著書情報
Article / Book Information

題目(和文)	
Title(English)	ALMA observational studies on the origins of the axisymmetric ring-gap structures in the protoplanetary disks
著者(和文)	KIM Seongjoong
Author(English)	Seongjoong Kim
出典(和文)	学位:博士(理学), 学位授与機関:東京工業大学, 報告番号:甲第11384号, 授与年月日:2020年3月26日, 学位の種別:課程博士, 審査員:奥住 聡,野村 英子,井田 茂,中本 泰史,佐藤 文衛,中島 淳一,武藤 恭之
Citation(English)	Degree:Doctor (Science), Conferring organization: Tokyo Institute of Technology, Report number:甲第11384号, Conferred date:2020/3/26, Degree Type:Course doctor, Examiner:,,,,,,
学位種別(和文)	博士論文
Type(English)	Doctoral Thesis

ALMA observational studies on the origins of the axisymmetric ring-gap structures in the protoplanetary disks

Department of Earth and Planetary Sciences

Tokyo Institute of Technology

Seongjoong Kim

ALMA observational studies on the origins of the axisymmetric ring-gap structures in the protoplanetary disks

A Ph.D.'s Dissertation
Submitted to the Department of Earth and Planetary Sciences,
School of Science at Tokyo Institute of Technology
in partial fulfillment of the
requirements for the degree of
Ph.D. of Science

Seongjoong Kim

January 2020

ACKNOWLEDGEMENTS

I would like to express my sincere gratitude to my supervisors Prof. Hideko Nomura for the continuous support of my Ph.D. research, for her patience, motivation, immense knowledge, and advice. Her guidance helped me in all the time when I was in the trouble of my research projects. Not only for the research, but I also get many bits of help for life in Tokyo, Japan.

Besides my supervisor, I would like to thank the colleagues of my research projects: Prof. Satoshi Okuzumi, Prof. Takayuki Muto, Dr. Takashi Tsukagoshi, Dr. Ryohei Kawabe, Dr. Sanemichi Takahashi, and all the coauthors of my published papers, for their insightful comments and creative ideas which make my research and perspectives much wider. My sincere thanks also go to all the faculty members of the Department of Earth and Planetary Sciences at the Tokyo Institute of Technology. By following their ways of scholars, I can improve my skills and knowledge for research. Without their precious guidance, it would not be possible to conduct my research.

I thank my mates at the Graduate school of Science, Chen-En Wei, Sota Arakawa, Kazumasa Ohno, Shoji Mori, Takahiro Ueda, Ayano Nakajima, Akihisa Yamakawa, and Harumi Minamoto, in all the fun moments we have had during the last three years. All the memories which share with you are the most precious moments for me. Especially, I appreciate the members of coffee time I have held for making various conversations about the research topics and Japanese cultures. Although some of them do not remain in Academia, I hope all of my mates are live their happy life and see you soon at the conference. I also thank Korean students in the Department, Beomsik Kim, Yohan Park, and Sanghee Lee, for being helpful adapting myself to a life in Tokyo. I hope everyone can finish his/her degree safely. Also, I thank all the graduate students in the Earth and Planetary Science Department who share the memories in the Tokyo Institute of Technology.

Lastly, I would like to thank my family for supporting me spiritually and physically throughout writing this thesis and my life in general. I sincerely appreciate your trust to keep studying Planetary sciences and my career. And I am sorry that I could not contact you often even though I am in Japan where there is no time lag. I do not know where I am going to go as a postdoctoral position, but I swear I often contact you there.

Seongjoong Kim

Contents

ACKNOWLEDGEMENTS i

CONTENTS iii

LIST OF FIGURES vi

LIST OF TABLES ix

ABSTRACT x

1 INTRODUCTION **1**

1.1 Backgrounds 1

1.1.1 Protoplanetary disks 1

1.1.2 The dust growth in protoplanetary disks 6

1.2 The origins of the axisymmetric ring-gap structures in protoplanetary disks 10

1.2.1 The planet-disk interaction 11

1.2.2 The instabilities 13

1.2.3 Molecular Snowlines 14

1.3 Overviews of Target disks 15

1.3.1 The CR Cha protoplanetary disk 16

1.3.2 The TW Hya protoplanetary disk 18
1.4 Scientific Goals 21

2 ALMA observation toward the CR Cha protoplanetary disk 24
2.1 Recent high-resolution ALMA Observation toward the CR Cha disk . . 25
2.2 The high-resolution images of the CR Cha disk 27
2.3 The azimuthally averaged intensity radial profiles 38
2.4 The peak brightness temperatures of the optically thick ^{12}CO and ^{13}CO lines 40

3 Two possible origins of the ring-gap structure in the CR Cha disk 49
3.1 The dust gap structure in the CR Cha disk 50
3.2 The C^{18}O gas column density 53
3.3 The dust-to-CO-gas mass ratio 58
3.4 The formation of dust ring-gap structure 63
3.4.1 Gap opening by a planet 63
3.4.2 Dust trapping at the gas pressure bump 68
3.4.3 The other possible origins 80

4 The synthetic ALMA multiband analysis on the TW Hya protoplanetary disk 82
4.1 Background and Motivation 83
4.2 The synthetic ALMA multiband analysis 84
4.2.1 The model intensity at the ALMA bands 85
4.2.2 The sensitivity analysis 86
4.3 The result of the synthetic multiband analysis 87
4.4 Physical interpretations of the synthetic ALMA multiband results 92

4.4.1 τ_ν effect . . . 92

4.4.2 β effect . . . 95

4.4.3 T_d effect . . . 95

4.4.4 Frequency intervals between the bands in the set . . . 98

4.5 Applications of the ALMA multiband analysis to the archival data of the TW Hya disk . . . 99

4.5.1 Application to Band [7,6,4] set . . . 104

4.5.2 Application to Band [9,6,4] set . . . 105

4.5.3 The possible origins of the gap structures in the TW Hya disk . . . 107

5 Future aspects of the ALMA multiband analysis **110**

5.1 The application to various protoplanetary disks . . . 111

5.2 Extension to ALMA Band 1 . . . 116

5.3 The synthetic ALMA multiband analysis with four ALMA bands . . . 117

5.4 The limitation of the ALMA multiband analysis . . . 123

5.4.1 The vertical structure of the disk . . . 123

5.4.2 The frequency dependency of β . . . 128

6 Summary **131**

BIBLIOGRAPHY . . . 137

List of Figures

1.1 The schematic pictures of star formation processes 2

1.2 The schematic picture of the classification of disk spectral energy distributions 4

1.3 The schematic picture of the protoplanetary disks 6

1.4 The dust continuum maps of the DSHARP samples observed by ALMA 10

1.5 The spectral index α of the CR Cha disk in mm-wavelengths 17

1.6 The dust continuum image of the TW Hya protoplanetary disk at ALMA Band 7 20

2.1 The dust continuum image of the CR Cha disk at 225 GHz 28

2.2 The moment 0 map of the ^{12}CO $J = $ 2-1 emission line in the CR Cha disk 29

2.3 The moment 0 map of the ^{13}CO $J = $ 2-1 emission line in the CR Cha disk 30

2.4 The moment 0 map of the C^{18}O $J = $ 2-1 emission line in the CR Cha disk 31

2.5 The averaged spectra of the CO isotopologue lines in the CR Cha disk . 33

2.6 The channel maps of the ^{12}CO line 34

2.7 The channel maps of the ^{13}CO line 35

2.8 The channel maps of the $C^{18}O$ line 36
2.9 The azimuthally averaged intensity radial profiles of the dust continuum and the CO isotopologue emission lines in the CR Cha disk 41
2.10 The line ratios between the CO isotopologue molecules 42
2.11 The moment 8 map of the ^{12}CO emission line 43
2.12 The moment 8 map of the ^{13}CO emission line 44
2.13 The azimuthally averaged $I_{\nu,\mathrm{peak}}$ of the ^{12}CO and ^{13}CO lines 47
2.14 The radial profiles of the $T_{\mathrm{B,peak}}$ for the ^{12}CO and ^{13}CO gases 48

3.1 The $\tau_{225\ \mathrm{GHz}}$ and Σ_{dust} radial profiles of the CR Cha disk 51
3.2 The $\tau_{\mathrm{C^{18}O,peak}}$ and $\Delta v_{\mathrm{C^{18}O}}$ radial profiles of the CR Cha disk 55
3.3 The $N_{\mathrm{C^{18}O}}$ and Σ_{dust} radial profiles of the CR Cha disk 56
3.4 The normalized dust-to-CO-gas mass ratio of the CR Cha disk 59
3.5 The Toomre's Q parameter of the CR Cha disk 62
3.6 The model Σ_{dust} profile around the gap opened by a planet in the CR Cha disk 65
3.7 The fitted Σ_{dust} and $\mathrm{N_{C^{18}O}}$ profiles for the radiative transfer calculation 70
3.8 The T_{gas} distribution in the disk r-z plane 73
3.9 The $\mathrm{T_{dust}}$ distribution at the disk midplane 74
3.10 The dust opacity models of the dust grains used for the radiative transfer calculation 75
3.11 The $\mathrm{T_{gas}}$ distribution at the photosphere of the ^{12}CO and ^{13}CO lines . . 78

4.1 The normalized average deviation of $T_{\mathrm{d,syn,max}}$ from $T_{\mathrm{d,model}}$ within 20 au$\leq r \leq$ 45 au 89
4.2 The constraint ranges of the synthetic dust properties in the TW Hya disk 90

4.3 The τ_ν effect on the constraint ranges of $T_{\rm d,syn}$ radial profiles 93
4.4 The β effect on the constraint range of $T_{\rm d,syn}$ profiles 96
4.5 The blackbody curves at the different $T_{\rm d}$ 97
4.6 The azimuthally-averaged de-projected radial profiles of intensity and brightness temperature of the TW Hya disk 102
4.7 The constraint ranges of $T_{\rm d}$, $\tau_{\rm B4}$, and β derived from the ALMA archival data by the ALMA multiband analysis 103

5.1 The 3D and 2D scatter plots of $T_{\rm d,syn}$, $\tau_{\rm 190\ GHz,syn}$, and $\beta_{\rm syn}$ 113
5.2 The constraining uncertainties of $T_{\rm d,syn}$, $\tau_{\rm 190\ GHz,syn}$, and $\beta_{\rm syn}$ for various model dust properties 114
5.3 The constraint ranges of the synthetic dust properties with ALMA Band 1 118
5.4 The normalized average derivations of $T_{\rm d,syn,max}$ within 20 au $\leq r \leq$ 45 au for the four ALMA band combinations 120
5.5 The synthetic ALMA multiband analysis results with the four band combinations 121
5.6 The synthetic ALMA multiband analysis results of the Band (10,7,6,3) and their sub-combinations of three bands 124
5.7 The vertical temperature structure model with different dust sizes 126
5.8 The dust opacity κ_ν and the opacity power-law index β_ν models of amorphous silicate spheres 130

List of Tables

2.1 The summary of new high-resolution ALMA observational data of the CR Cha disk 27

2.2 The fitting parameters for the spectra of the CO isotopologue lines in the CR Cha disk 38

2.3 The fitting parameters for the $T_{\rm B,peak}$ profiles of the ^{12}CO and ^{13}CO gases in the CR Cha disk 46

3.1 The fitting parameters for the dust gap in the CR Cha disk 52

4.1 Summary of the ALMA Band 85

4.2 The information of ALMA archival data used for the ALMA multiband analysis 100

ABSTRACT

Disk substructures in protoplanetary disks (PPDs), such as axisymmetric ring-gap structures, spiral arms, and lopsided dust accumulations, are considered as possible signposts of forming planets in the disks. Recent high-resolution Atacama Large Millimeter/Submillimeter Array (ALMA) observations have revealed that these disk substructures are very common in PPDs. To understand the origins of these disk substructures, especially focusing on the axisymmetric dust ring-gap structures, I study the dust and gas properties using ALMA observational data.

First, I detect the axisymmetric dust ring-gap structure of the CR Cha PPD by the recent high-resolution ALMA observation at Band 6. It is the first time resolving the CR Cha disk with $\sim 0''.09$ beam size ($\sim$ 16 au in the physical scale at the distance of $d \sim 187.5$ pc). The CO isotopologue (^{12}CO, ^{13}CO, and C^{18}O) emission lines are also observed with $\sim 0''.2$ resolution for obtaining gas properties. There is a bump-like structure in the peak brightness temperature radial profile of the ^{13}CO line at the location of the dust ring but not in the ^{12}CO line. To explain these observed features in the CR Cha disk, I suggested two possible mechanisms. First possible scenario is the gap opening by a planet. The empirical relation between the planet mass and the gap structure indicates that a Jupiter-mass planet is required to reproduce the observed gap structure in the CR Cha disk. Once the dust gap is opened by a planet, the stellar radiations make a temperature bump at the dust ring location because they easily reach to the outer wall of the gap directly by the low optical depth. Another possible scenario is dust trapping at a gas pressure bump. When the dust disk becomes more compact than the gas disk due to radial drifts of dust grains, the gas temperature bump is formed at the outer edge. The radiations emitted from the central star and the hot disk surface layer penetrate to the disk midplane due to the small optical depth outside of the dense

dust disk. The radiative transfer calculation reproduces the observed gas temperature bump at the outer edge of the dust disk. A gas pressure bump could be created by this temperature bump, then the dust grains would be trapped at this gas pressure bump during their radial drifts from the outer disk, eventually making a dust ring structure.

The multiwavelength analysis of the observational data is one of the powerful tools to constrain the dust properties more accurately than the single wavelength. The TW Hya disk is the best object to test the synthetic ALMA multiband analysis because it has many ALMA archival data. I study the synthetic ALMA multiband analysis to find the best three ALMA band combination for deriving the accurate dust temperature $T_{\rm dust}$, optical depth τ_ν, and dust opacity power-law index β ($\kappa_\nu \propto \nu^\beta$) using the ALMA archival data of the TW Hya disk. Through this approach, I can directly derive the three unknowns ($T_{\rm dust}$, τ_ν, β) without any assumptions on dust temperature and optical depth. The synthetic multiband analysis results show that the Band [10,6,3] set is the best combination for minimizing the constraining uncertainties of the dust properties from the model dust properties of the TW Hya disk. The band combinations with Band 9 or 10 and with the large frequency intervals between the bands in the set give us narrow constraint ranges on the dust properties. These are related to the conditions which give good constraints on dust properties: the combination of optically thick and thin bands, large β, and low dust temperature.

To examine the consistency of the synthetic analysis results, I apply the multiband analysis to ALMA archival data of the TW Hya disk at Band 4, 6, 7, and 9. The Band [9,6,4] set provides the dust properties close to the model profile, while the Band [7,6,4] set gives the dust properties deviating from the model at all radii with a very broad constraint range. These features are well consistent with the synthetic ALMA multiband analysis results.

Chapter 1

INTRODUCTION

1.1 Backgrounds

1.1.1 Protoplanetary disks

Since 1995, when the first exoplanet 51 Peg b was detected, thousands of exoplanets have been detected by various methods, such as the radial velocity method (e.g., Mayor & Queloz 1995), the transit photometry (e.g., Seager 2008), direct imaging with coronagraph (e.g., Kalas et al. 2008), microlensing by planet gravity (e.g., Beaulieu et al. 2006), and stellar astrometry (e.g., Benedict et al. 2002). The detected planets have various masses, sizes, and orbital properties [1]. Furthermore, their host stars are not only isolated stars but multiple stellar systems (e.g., Santos et al. 2003; Udry & Santos 2007; Borucki et al. 2010; Bergfors et al. 2012; Everett et al. 2013; Batalha 2014, etc). It indicates that the existence of planets around star(s) is a quite general feature in the Universe.

To understand the diversity of the detected exoplanet systems, where the planets are

[1] exoplanets.eu

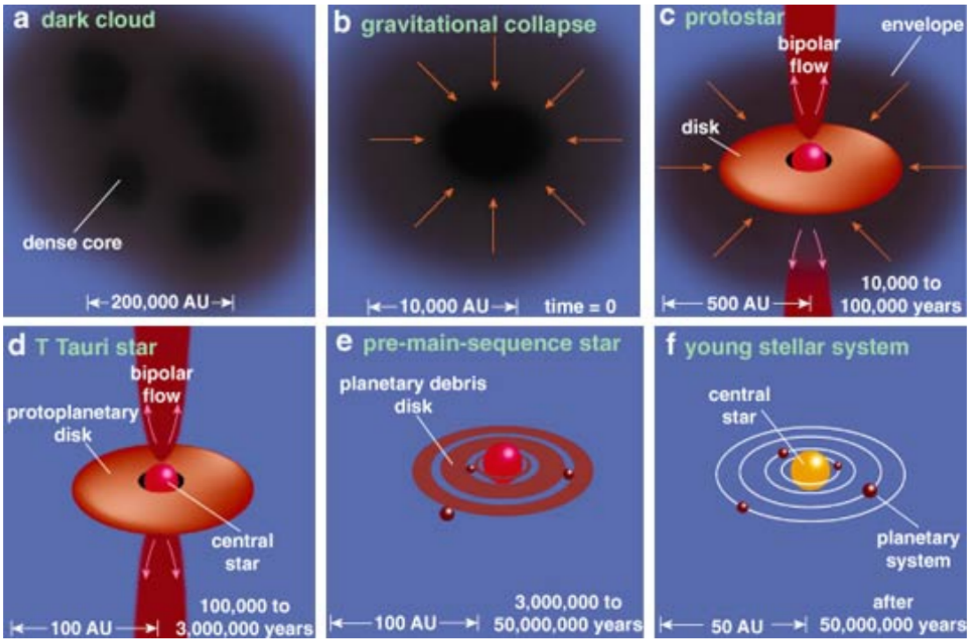

Figure 1.1. The schematic picture of the star formation processes (Greene 2001). The materials are collapse to the central stellar core by self-gravity and create the accretion disk surrounding the core called circumstellar/protoplanetary disks. Inside the protoplanetary disks, the solid materials grow to the large bodies by collisions as a seed of the planet. Eventually, the planetary systems are created after dissipating the disk materials.

formed and how they evolve are essential topics in the star and planet formation research field. Recently, planet formation theories have actively studied with the breakthrough of observational and computational tools. However, the detailed physical processes of the planet formation are still ambiguous. Although the planet formation processes are not completely unveiled, there is one consensus that planets are formed in the dust and gas disks surrounding (proto)stars, which is called protoplanetary disks (e.g., Safronov 1972; Weidenschilling 1977). Figure 1.1 presents the schematic pictures of the star-forming stages from molecular clouds to exoplanetary systems with their typical evolution time scales and physical size scales in the bottom (Greene 2001). During the gravitational collapses of the parent molecular clouds into the central core, the accretion disk is created by the angular momentum conservation of the materials and coupling with magnetic fields. Even though many researchers have studied very actively, the dissipation mechanisms of the angular momentum of the disk materials and the effects of stellar and cloud magnetic fields are not completely understood yet (e.g., Girart et al. 2006; Attard et al. 2009; Frank et al. 2014). Once the protoplanetary disk is born, they survive typically $t \sim$ 1-3 Myr. It is derived from the decay of the detection fraction of the protoplanetary disks surrounding the late-type stars in some nearby star-forming and young stellar clusters (e.g., Haisch et al. 2001; Hernández et al. 2007, 2008). Inside the protoplanetary disks, the solid materials grow into the seeds of planets by aggregates and collisions. When the central core becomes a pre-main sequence star, the disk gases start to be dissipated by stellar radiation, thermal evaporations, and accretions into planets. After all the disk materials are dissipated, various planetary systems have remained as a result.

During the star-forming stages, the circumstellar/protoplanetary disks are detected by the spectral energy distribution (SED) in the infrared (IR) observations (e.g., Lada

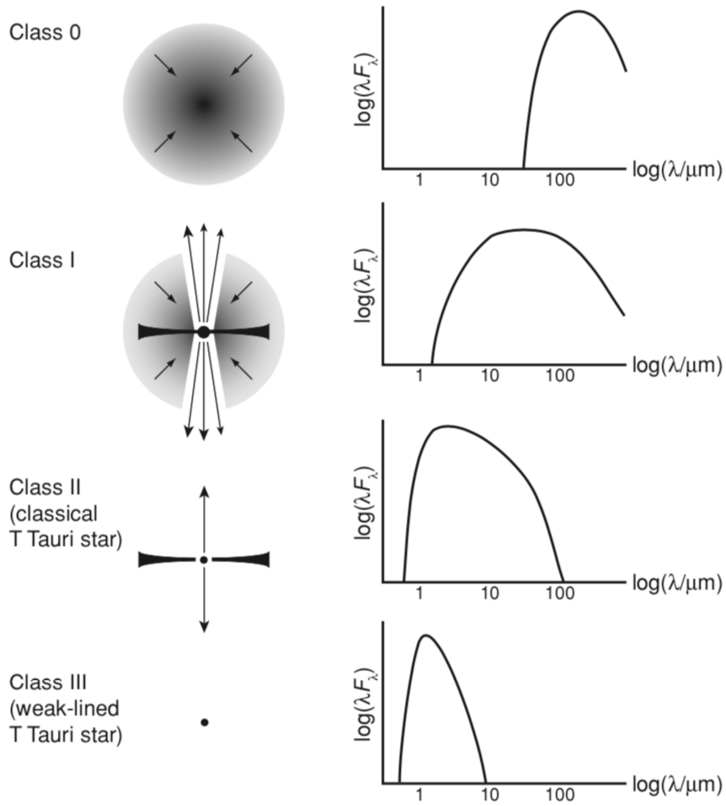

Figure 1.2. The schematic picture of the classification of disk spectral energy distributions (SED) in infrared (IR) wavelength regime (Armitage 2010). Class 0 has an intensity peak at the wavelengths of $\lambda \gtrsim 100$ μm, mainly emitted from the cold envelope materials. The SED of Class I objects extends to a much shorter wavelength up to $\lambda \sim$ 1-10 μm with a flat spectrum in the mid-IR to the far-IR regimes. The SED of Class II objects is composed of the blackbody radiation of central star and dust emission from the surrounding disk. The Class III SED shows mainly the stellar blackbody radiation because the most disk materials are already dissipated.

& Wilking 1984; Andre et al. 1993; Andre & Montmerle 1994). Based on the observed SED of the disks in the nearby star-forming regions, the disks are typically classified as four different classes depending on the spectral index $\alpha_{\rm IR}$ between ~ 2 μm and ~ 10 μm or 24 μm (e.g., Armitage 2010). Figure 1.2 presents the schematic pictures of the disk classifications with their SED and corresponding star-forming stages. Protoplanetary disks are usually considered from late Class I to early Class III stages.

Class 0 objects have an intensity peak at the wavelengths of $\lambda \gtrsim 100$ μm, mainly emitted from the cold envelope materials, without any IR emission from the central core. As the materials gravitationally collapse into the central core, the SED is extended to the shorter wavelengths up to $\lambda \sim$ 1-10 μm with the flat spectral index or positive slopes of $\alpha_{\rm IR} \gtrsim -0.3$. It is classified as Class I objects. As the disks evolve further, the disks become Class II objects. The SED of Class II objects is mainly composed of the blackbody radiation of the central star and the dust emission from the surrounding disk. The excess emissions in the IR regime from the surrounding disk make a negative spectral index of $\alpha_{\rm IR} \lesssim -0.3$. In the end, only stellar blackbody radiations remain in the SED of Class III objects because the most disk materials are gone by various dissipation mechanisms.

The SED shows the integrated and averaged information of the central star and the surrounding disk. When the disk is spatially resolved, it shows very broad ranges of temperature and density distributions along the disk radial and vertical directions. Figure 1.3 shows the schematic picture of the protoplanetary disks. The different wavelengths trace different disk parts. The IR wavelengths regime mainly trace the hot regions in the disks, such as the very inner disk radii and the hot upper surface layer. Meanwhile, the (sub)millimeter wavelengths are the most suitable wavelengths to trace the thermal emissions of the cold large dust grains in the disk midplane. Since the long-

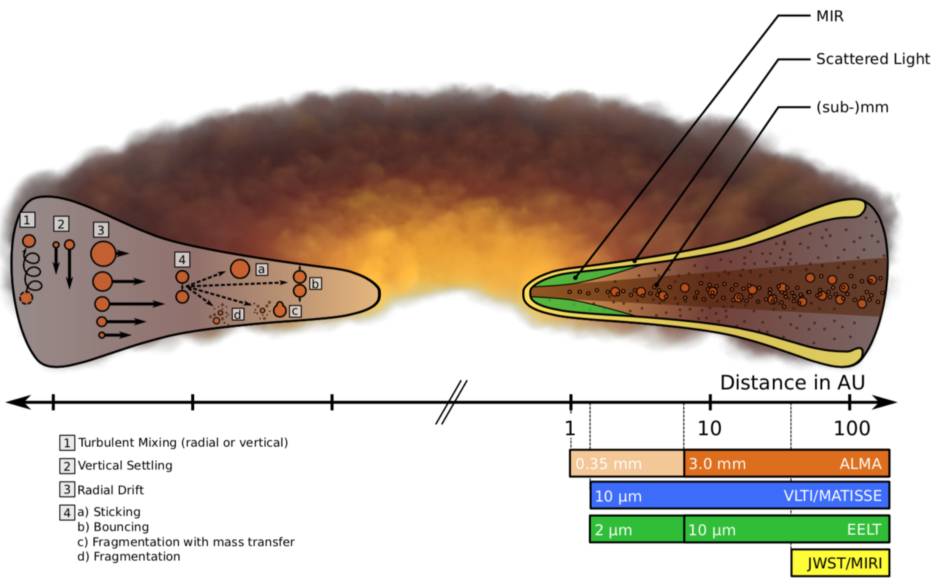

Figure 1.3. The schematic picture of the protoplanetary disks (Testi et al. 2014). Inside the disks, the dust grains tend to settle down to the midplane and radially drift to the central star by the interaction with disk gases. During those movements, the grains grow from small particles to large bodies by colliding with each other.

wavelength lights can see much deeper parts of the disk than the short wavelengths, (sub)millimeter wavelengths mainly trace relatively dense cold regions like the disk midplane more easily than IR wavelengths. Also, if I use the observing wavelengths as proxies of dust grain sizes, the long-wavelength observations trace large dust grains in the disks.

1.1.2 The dust growth in protoplanetary disks

Dust grain growth is another one of the important topics for understanding planet formation processes. Inside the PPDs, dust grains tend to settle down to the disk midplane overcoming the turbulent mixing and drift inward to the central star by the interaction between the dust grains and gas particles as shown in Figure 1.3 (e.g., Armitage 2010; Birnstiel et al. 2012; Testi et al. 2014). Those movements lead to the growth and destruction of dust grains by collisions, making different grain sizes from μm-sized grains to mm/cm-sized pebbles, and eventually growing up to km-sized planetesimals (e.g., Takeuchi & Lin 2005). To understand the growth rates, the experimental studies have tried to measure the stickiness of the grains (e.g., Heim et al. 1999; Gundlach et al. 2011). Traditionally, the water ice surfaces have been thought to have higher stickiness than the dry silicate grains. However, recent research indicates that the efficiency of dust growth and destruction varies with their physical properties and chemical compositions (e.g., Okuzumi et al. 2012; Okuzumi & Tazaki 2019; Steinpilz et al. 2019). It needs more investigation to clarify the detailed mechanisms and efficiency.

Also, the computational simulations on the collisions between the grains have examined the evolution of internal density and the growth conditions of the grains by the aggregates (e.g., Suyama et al. 2008; Wada et al. 2007, 2008, 2009). Simulations show that the low collision velocity ($v_{\rm col} \lesssim 1{\rm cm\ s^{-1}}$) with comparable size grains make fluffy aggregates (e.g., Meakin 1991). As the $v_{\rm col}$ increases, the aggregates make compression on the colliding grains. And if $v_{\rm col}$ exceeds the fragmentation velocity, the threshold velocity of the collisional destructions, the grains are fragmented instead of sticking each other. Since the internal structure of the grains and the grain sizes are the important parameters for calculating the Stokes number St (e.g., Birnstiel et al. 2012), the indicator of the mobility of the grains in the gas disk, they are essential information to estimate the grain growth in the PPDs and the maximum grain sizes. Moreover, Since the grain structure affects the scattering of the background lights (e.g., Kataoka et al. 2015; Tazaki et al. 2019), it is also important for interpreting the observational data to derive the dust properties.

Even by the various experimental and computational studies, the dust growths are not completely revealed yet. There is one famous problem in the classical dust growth theory called "Drift barrier" problem: the dust grains are hardly growing to the km-sized particles from the mm/cm-sized grains due to too fast radial drifts of the meter-sized grains in the gas disk (e.g., Armitage 2010; Laibe 2013; Morbidelli & Raymond 2016). The dust grains are experiencing the headwind because of a sub-Keplerian rotation of gas components supported by a radial gas pressure gradient. The efficiency of gas drag is depending on the grain sizes and their internal density structures (e.g., Armitage 2010; Birnstiel et al. 2016; Morbidelli & Raymond 2016). For example, the gas surface density of the minimum mass solar nebula (Weidenschilling 1977) at 1 au is $\Sigma_{\rm gas} = 1700$ g cm^{-2}. In this gas disk, the meter-sized boulders have a maximum drag force with a very shorter drifting time scale than the grain growth time scale. To overcome this barrier, some mechanisms are required to stop or slow down the radial drifts of the dust grains in the disks: gravitational instability (e.g., Johansen & Youdin 2007), turbulence (e.g., Johansen et al. 2011), or eddies (e.g., Cuzzi et al. 2008). The small-scale ($\sim$ a few au-scale) disk substructures, such as axisymmetric ring-gap structures, spiral arms, and lopsided dust disks, would be the products of those mechanisms for overcoming the drift barrier.

The observational studies also have detected the various disk morphology in the IR and mm-wavelengths. Since the central stars are still very bright in the IR wavelengths, the polarized lights or the chronography are suitable to observe the surrounding disks in the IR regimes. Those observations have revealed the substructures in the disks such as the spiral arms, the gap structures, and the inner cavity (e.g., Tanii et al. 2012; Avenhaus et al. 2014; Rapson et al. 2015). However, the IR wavelengths cannot trace the disk midplane due to the very high optical depth at the disk surface.

The mm-wavelength observations are essential to see the disk midplane. However, the previous generation arrays in (sub)millimeter wavelengths (e.g, CARMA, SMA) are limited in the sensitivity and spatial resolution for detecting the small-scale disk substructures less than a few tens au because of the small antenna numbers and short baselines. Therefore, the small-scale disk substructures have rarely been detected in many survey projects using these arrays toward the disks in some star-forming regions (e.g., Eisner et al. 2008; Öberg et al. 2010, 2011). These observational data have improved the understanding of the averaged disk properties in the entire disk or in the large scales. It indicates that the high-resolution observations at (sub)mm-wavelengths are required to detect the small-scale disk substructures.

The emergence of Atacama Large Millimeter/Submillimeter Array (ALMA) opened a new era on the (sub)mm-wavelengths observations. The high performances of ALMA on the spatial resolution and the sensitivity make the small-scale disk substructures being detected. Recent ALMA surveys of the thermal dust continuum toward the protoplanetary disks in nearby star-forming regions (e.g., Andrews et al. 2018; Long et al. 2019) show that the disk substructures are very common. Figure 1.4 presents the 20 disk samples of the Disk Substructures at High Angular Resolution Project (DSHARP; Andrews et al. 2018). They present various small-scale substructures such as axisymmetric ring-gap structures, spiral arms, and lopsided dust accumulations.

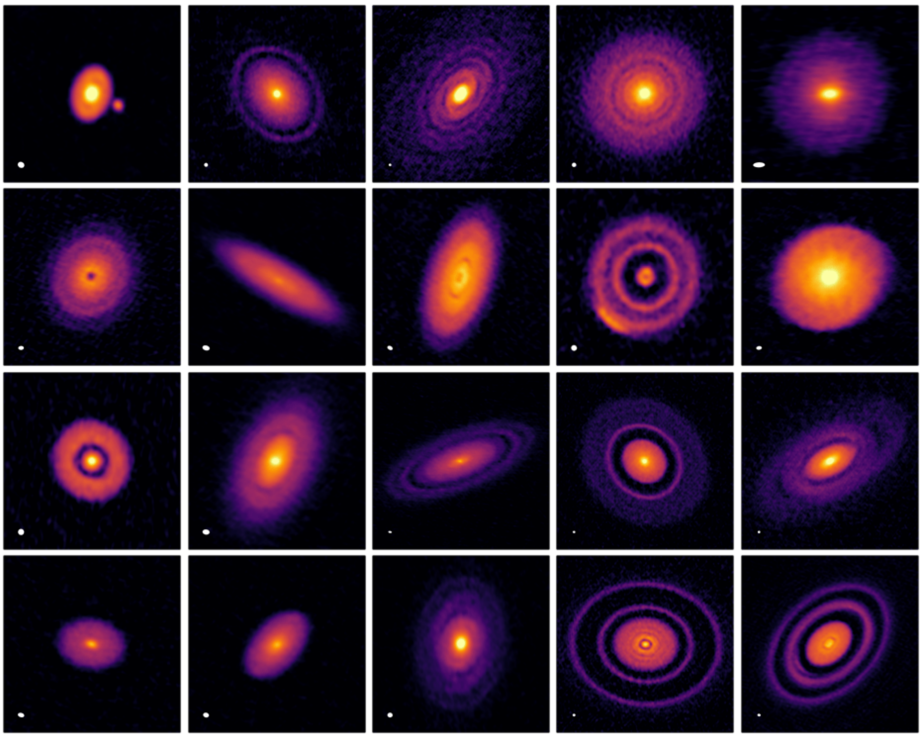

Figure 1.4. The dust continuum maps of DSHARP samples observed at ALMA Band 6. A total of 20 sample disks show their dust disks having various disk substructures: axisymmetric ring-gap structures, spiral arms, and lopsided dust accumulations. The most popular substructure in the samples is the axisymmetric ring-gap structures.

1.2 The origins of the axisymmetric ring-gap structures in protoplanetary disks

Among various disk substructures, axisymmetric (multiple) ring-gap structures are the most common feature observed in protoplanetary disks. Many theoretical/numerical studies have suggested some possible mechanisms producing the ring-gap structures in PPDs: (1) the planet-disk interaction (e.g. Kanagawa et al. 2016; Dong et al. 2017; Bae et al. 2017; Fedele et al. 2018), (2) the instabilities induced by various physical mechanisms (e.g., Secular Gravitational Instability or Magnetorotational Instability; Youdin 2011; Takahashi & Inutsuka 2014; Flock et al. 2015), and (3) the molecular snowlines (e.g. Zhang et al. 2015; Okuzumi et al. 2016). These scenarios are still under debate on which mechanism is the best explanation of the origin of the axisymmetric ring-gap structures due to the lack of observational supports. In this section, I will briefly introduce some possible gap origins.

1.2.1 The planet-disk interaction

When a massive planet is in the protoplanetary disks, the dust and gas materials in the disks are perturbed by the gravity of massive (proto)planets. By exchanging the angular momentum and energy between the (proto)planet and the disk materials by the gravitational interactions, The disk materials moving away from the orbits of the (proto)planets (e.g., Lin & Papaloizou 1979; Goldreich & Tremaine 1980). Then, the gas gap is opened by an evacuation of the materials around the orbit of the (proto)planet. Through this mechanism, only small dust grains coupled with the gas components are survived in the gap region while the large dust grains are trapped in the gas pressure bump at the outer edge of the gas gap (Dust filtration; Zhu et al. 2012). Then, the grain size distributions inside and outside of the gap structures are different. The observational studies often use the spectral index α or the dust opacity power-law index β as the proxy of the maximum grain size (e.g. Miyake & Nakagawa 1993; Mennella et al. 1998; Chihara et al. 2002; Draine 2006; Koike et al. 2006; Min et al. 2016; Woitke et al. 2016). Therefore, the β is enhanced inside the gap structures but decreases at the outer edge of the gap.

The most common way to examine the planet-disk interaction scenario is the comparison between the observed gap structures and the model expectations by the numerical simulations. Depending on the planet mass, the gas gap is also created with the dust gap. For example, Kanagawa et al. (2017) expresses the empirical relation of the gap width and depth to the planet mass. Through this relation, the planet mass is estimated to explain the observed gas gap structures (See Section 3.4.1). Although this relation is based on the assumption that one gap is corresponding to one planet, some recent numerical studies suggest the possibility that the multiple gaps can be opened by the gravitational perturbation of a single planet when the dimensionless turbulence parameter α (Shakura & Sunyaev 1973) is very low ($\alpha \leq 10^{-4}$) (e.g., Dong et al. 2017; Bae et al. 2017; Fedele et al. 2018). However, since the derivation of the turbulence α in the disk from the observational data is difficult, it is very difficult that distinguishing whether a single planet opens only one gap or multiple gaps observationally.

The circumplanetary disk could be one of the direct observational evidence for the planet-disk interaction scenario. The forming planet accretes the disk materials by creating the accretion disk surrounding it. Tsukagoshi et al. (2019) has detected a small blob of the excess emission at the edge of the dust disk surrounding the TW Hya T Tauri star. Although the observed blob is not inside the gap structures of the TW Hya disk, it is a candidate for the circumplanetary disk. If this kind of point source is discovered in a gap, it is direct observational support that the gap structures are opened by the planet-disk interaction. Additionally, the Hα emission and/or the IR point source are another observational evidence for the circumplanetary disks (e.g., Wagner et al. 2018; Keppler et al. 2018). Those lights are emitted from the hot accreting gases onto the planets from the disks.

1.2.2 The instabilities

Another possible mechanism for gap opening in protoplanetary disks are instabilities induced by various causes. One of the mechanisms is the secular gravitational instability (Secular GI; e.g. Youdin 2011; Takahashi & Inutsuka 2014). The secular GI is occurred by the gas-dust friction. It dissipates the Coriolis force of the dust grains during their radial drifts. Then, they are concentrated at a certain radius by making the axisymmetric ring-gap structures. The simulations insist that the secular GI prefers the marginally gravitationally unstable disks (Toomre's Q parameter $\sim$ 1-3), high dust-to-gas mass ration ($\epsilon \gtrsim 0.1$), and weak turbulence strength ($\alpha \lesssim 4\times10^{-4}$) (e.g., Takahashi & Inutsuka 2014). Also, since the gas-dust friction needs the background gas flow, it is not preferred the existence of the gas gap. Although the turbulence strength is difficult to be determined by the observations, the dust-to-gas mass ratio and the Toomre's Q parameter can be easily obtained from the observations.

Another kind of instability can be induced by the magnetohydrodynamic (MHD) effects called magnetorotational instability (MRI; e.g. Flock et al. 2015). The disk midplane is very cold and dense so that the ionization fraction is very low but not zero by the non-thermal ionization processes that occurred by the cosmic rays and the stellar X-rays ($x \lesssim 10^{-12}$; e.g., Armitage 2010). With this very low ionization fraction, the non-ideal magnetohydrodynamic effects suppress the turbulences at the disk midplane. This area is called a dead zone. At the outer edge of the dead zone, the smooth jump of the gas pressure and density structures are occurred by the discrepancy of turbulence strength (e.g., Armitage 2015). This jump makes a reversed gradient of gas pressure, then the gas pressure bump is created at the outer dead-zone boundary. The dust grains are concentrated at this pressure bump making an axisymmetric ring-gap structure in the disk and the creation of planetesimals. This mechanism requires the low ionization fraction in the disk midplane of the dead zone and the gas pressure bump structure at the dead-zone boundary. To obtain the ionization fractions, the line observations of the various molecular and ionic species in the disks are essential. However, since the line observations are expensive than the dust continuum observations, it would not be an efficient way to check this model. Although the gas pressure bump can be created by the other causes, it would be a better way because they are more easily obtained from the observations.

1.2.3 Molecular Snowlines

Dust grains in the disks are growing from sub-micron size to planetesimal size by the collisions (e.g., Okuzumi 2009; Okuzumi et al. 2012). However, the growth rates and stickiness of the grains are varying with the physical and chemical status of the grain surfaces. For example, Okuzumi & Tazaki (2019) constrains the maximum grain size of $\sim 100\mu$m in the HL Tau disk from their polarization observation at sub-mm wavelength. They interpret this small maximum grain size is due to the non-sticky CO_2 ice on the grain surface. Recent laboratory experiments have reported that the CO_2 ice particles are less sticky than H_2O ice particles at the same size (e.g., Musiolik et al. 2016a,b).

The temperature structure of the disks is one of the important parameters on the dust growths because the sublimation of the molecules from the grain surfaces changes the physical and chemical properties of dust grains. Around the molecular snowlines, where the disk temperature equals the sublimation temperature of the molecules, the dust grain sizes vary along the disk radius by the sublimation process (e.g. Zhang et al. 2015; Okuzumi et al. 2016). Zhang et al. (2015) suggests that the gap is opened by the rapid growths of dust grains inside the condensation front. By the rapid growth of the grains, the density of the mm-sized grains decreases so that the intensity at the gap region also decreases. In this case, the observed spectral index α or the dust opacity power-law index β becomes small because the dust grains grow larger than the millimeter sizes. In contrast, the sintering effect (Okuzumi et al. 2016) suggests that the partial sublimation of the molecules makes the icy grains more easily fragmented by the collisions instead of sticking outside the molecular snowlines. It makes the grain sizes in this region small and the Stokes numbers of the grains become smaller as well. Therefore, since the radial drifts of the fragmented small dust grains become slower, they are accumulated outside the snowlines with a β enhancement in the accumulated region.

This mechanism has an advantage in the formation of the multiple ring-gap structures because every snowline for each molecular species can be assigned as an origin of the gap structures. However, this is also a weakness of this mechanism that the ring-gap structures should be matched with the radii of snowlines. Another advantage of the molecular snowline scenario is that it is independent of the existence of the gas gap because this mechanism depends only on the grain sizes. Therefore, this mechanism is preferred for the disks only having dust gaps and not gas gaps.

1.3 Overviews of Target disks

In Section 1.2, I briefly introduce some possible origins of the axisymmetric ring-gap structures in PPDs. Among many PPDs having axisymmetric ring-gap structures resolved by the ALMA, I choose two disks, the CR Cha and the TW Hya disks, for studying the origins of their ring-gap structures using the ALMA observational data. In this section, I will introduce the overviews of the CR Cha and TW Hya disks.

1.3.1 The CR Cha protoplanetary disk

Chamaeleon dark clouds are one of the active star-forming regions in our Galaxy near the south pole ($Dec \sim -77°$). The Chamaeleon complex consists of three sub-structural clouds named as Cha I, Cha II, and Cha III (Luhman 2008). The distance of the Chamaeleon complex is recently updated as $d \sim$ 179-200 pc by Tycho-Gaia Astrometry (Gaia Collaboration et al. 2016; Voirin et al. 2018). Since the Chamaeleon clouds have many young stars, these clouds have been good targets to perform surveys at various wavelengths, such as Hα line emission, X-ray emission, and infrared excess emission, for investigating the properties of young stars and their PPDs (e.g., Whittet et al. 1987; Gauvin & Strom 1992; Carpenter et al. 2002; Luhman 2004; Furlan et al. 2009; Varga et al. 2018).

CR Cha (aka Sz 6, Cha T8) is a K-type pre-main-sequence star (Hussain et al. 2009; Villebrun et al. 2019) in the Cha I dark cloud. An optical V-band brightness of CR Cha is $m_V = 11.2$. It has a short rotation period of $P_{\rm rot} = 2.3$ day (Bouvier et al. 1986; Schegerer et al. 2006). Also, CR Cha is a strong X-ray emitter with the luminosity of $L_{\rm X} \sim 1.48 \times 10^{30}$ erg s^{-1} (Feigelson et al. 1993; Robrade & Schmitt 2006). The accretion rate of CR Cha is moderate ($log(\dot{M}_{\rm acc}) \sim -8.71$; Manara et al. 2016) derived from the Hα line observation ($EW_{\rm H_\alpha} \sim$ 29.5-34 Å; Reipurth et al. 1996; Guenther et al. 2007). The fitting on the stellar evolution tracks suggests that the stellar mass of CR Cha is $M_\star =$ 1.2-2 $M_\odot$ with an age of $t \sim$ 1-3 Myr (e.g., D'Antona & Mazzitelli 1994; Natta et al. 2000; Hussain et al. 2009; Varga et al. 2018). The latest updated distance of CR Cha is $d \sim 187.5 \pm 0.8$ pc (GAIA DR 2; Gaia Collaboration et al. 2018).

The existence of the PPD around CR Cha had already been revealed by the dust thermal emission at (sub)mm-wavelengths (e.g., Ubach et al. 2012; Pascucci et al. 2016;

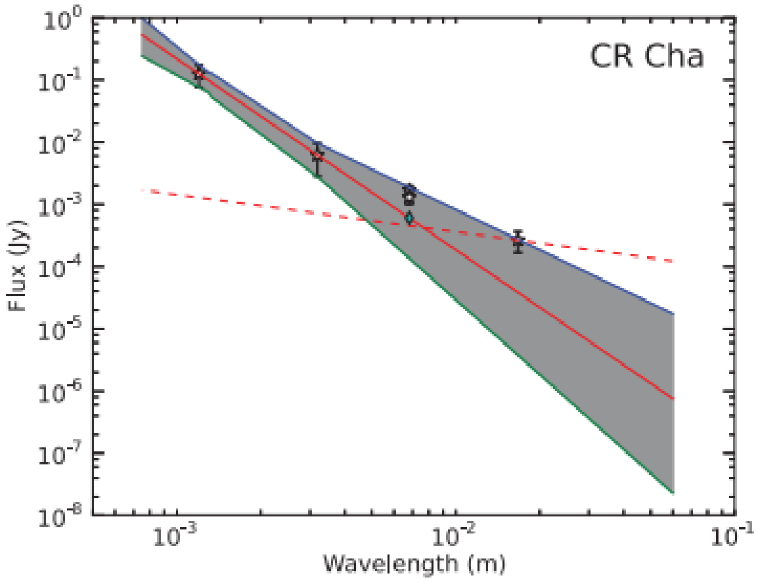

Figure 1.5. The spectral index α of the CR Cha disk in mm-wavelengths (Figure 1 of Ubach et al. 2012). The error bars indicate the uncertainty of the flux and the primary flux calibration. The red solid line represents the spectral index at 1 mm $\alpha_{1\ \mathrm{mm}} = 3.4$ and the grey shaded region indicates the uncertainty of $\alpha_{1\ \mathrm{mm}}$.

Ribas et al. 2017; Ubach et al. 2017). The spectral index α at (sub)mm-wavelengths is linked to the dust properties, such as dust opacity and dust grain size (e.g., Miyake & Nakagawa 1993). It can be used to study the dust growth in the disk by comparing it with the α of the interstellar medium (ISM) (e.g., Beckwith & Sargent 1991; D'Alessio et al. 2001). Toward the CR Cha disk, the measured spectral index at 1 mm is $\alpha_{1\ \mathrm{mm}} \sim 3.4$ (Figure 1.5; Ubach et al. 2012), which is close to $\alpha_{\mathrm{ISM}} \sim 3.7$ of the ISM. This large $\alpha_{1\ \mathrm{mm}}$ value in the CR Cha disk indicates that the maximum grain size is small in the outer disk (e.g., Draine 2006). Ribas et al. (2017) and Ubach et al. (2017) suggested that this may be the result of the dust growth in the outer disk: the mm-sized dust grains already drifted inward in the gas disk due to the gas drag. A recent CO line survey toward the protoplanetary disks in Cha I cloud using ALMA can support this possibility by detecting the gas disk around the CR Cha with an angular size of $\sim 0''.9$ in radius (Long et al. 2017).

However, the time scale of the radial drift of mm/cm-sized dust grains (10^{4-5} yr; e.g., Takeuchi & Lin 2005; Brauer et al. 2007) is much shorter than the age of CR Cha ($t \sim$ 1-3 Myr). Ribas et al. (2017) suggested that some braking mechanisms are required to stop or slow down the radial drifts of the dust grains such as dust trapping at the gas pressure bumps produced by zonal flow (e.g., Pinilla et al. 2012) or gap opening by a planet (e.g., Zhu et al. 2012). That is, the CR Cha disk is one of the strong candidates which would have disk substructures like a dust ring-gap structure. However, there are no high-resolution observations yet to resolve the disk substructures less than a few tens au scale.

Therefore, the high spatial resolution ALMA observation is needed to detect the small-scale disk substructures in the CR Cha disk. Chapter 2 will introduce new detection of the disk substructure in the CR Cha disk for the first time by the ALMA high-resolution observation. It contributes to the studies on the disk substructures in the PPDs by enlarging the numbers of the disk samples having disk substructures. Also, Chapter 3 will introduce the possibility of some mechanisms to explain the origins of the observed disk substructure. This approach can contribute to the studies for understanding the gap origins by providing observational supports.

1.3.2 The TW Hya protoplanetary disk

TW Hydrae (TW Hya) is identified as a T Tauri star with the mass of $M_* \sim 0.8\, M_\odot$, isolated from the parent cloud (Herbig 1978; Andrews et al. 2012). The follow-up observations around TW Hydrae identified more T Tauri stars and some brown dwarfs, then they are named as the TW Hydrae association (e.g., Sterzik et al. 1999; Zuckerman et al. 2001). These T Tauri stars and brown dwarfs are good samples to examine the star formation processes with its proximity ($d \sim 59.5 \pm 1$ pc; Gaia Collaboration et al. 2018).

The PPD around TW Hya with substantial gas and dust contents have been imaged many times at near-IR (e.g., Krist et al. 2000; Weinberger et al. 2002; Debes et al. 2017) and (sub)millimeter wavelengths (e.g., Qi et al. 2004; Andrews et al. 2011; Akiyama et al. 2015). The disk mass of $M_{\rm disk} > 0.05\ M_{\odot}$ is derived from the HD emission line observed by the Herschel Space Telescope. The estimated age of the TW Hya disk is $t \sim$ 3-10 Myr (Bergin et al. 2013). Compared with the typical lifetime of gaseous PPDs of $t \sim 3$ Myr (Hernández et al. 2007), the TW Hya disk is an old population.

Recent ALMA high spatial resolution observations (e.g., Andrews et al. 2016; Tsukagoshi et al. 2016; Nomura et al. 2016) have revealed that the TW Hya disk is one of the representative PPDs which have axisymmetric ring-gap structures. Figure 1.6 presents the very high-resolution ($\sim 0''.03$ corresponding to ~ 2 au in physical scale at the distance of $d \sim 59.5$ pc) dust continuum image of the TW Hya disk observed at ALMA Band 7. There are two narrow and shallow dust gaps at $r \sim 25$ au and $r \sim 41$ au. The estimated gap widths of two gaps are $\sim$ 1-6 au with the gap depth of $\sim$ 5-30% (Andrews et al. 2016).

The gaseous disk surrounding TW Hya has been also observed many times by various molecular lines. The CO isotopologue emission lines are usually used to trace the gas disk. Favre et al. (2013) derived the CO-to-H_2 ratio χ(CO) of the TW Hya disk from the HD (1$-$0) line observed by the Herschel Space Telescope and the $C^{18}O$ $J = 2{-}1$ emission line observed by SMA. The derived $\chi({\rm CO}) = (0.1\text{-}3) \times 10^{-5}$ is lower than the canonical value of 10^{-4} indicating the chemical destruction of CO molecules by the

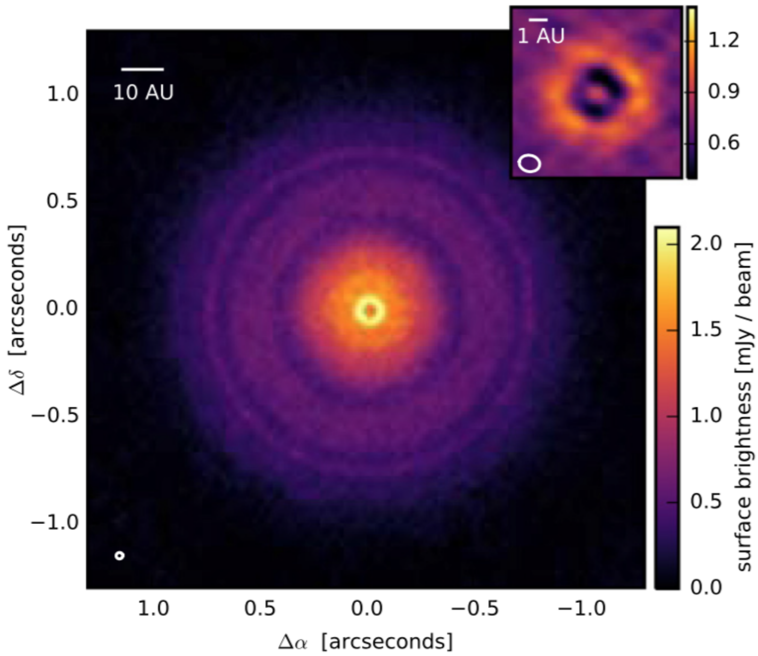

Figure 1.6. The dust continuum image of the TW Hya protoplanetary disk at ALMA Band 7 (Andrews et al. 2016). The beam size of image is $\sim 0''.03$, corresponding to $\sim$ 2 au in physical scale at the distance of $d \sim 59.5$ pc. There are two narrow dust gaps at $r \sim 25$ au and $r \sim 41$ au.

rapid formation of carbon chains or CO_2 molecules. Schwarz et al. (2016) observed the ^{13}CO and $C^{18}O$ emission lines in the TW Hya disk. They also confirm that the CO gas is depleted in the TW Hya disk. Since the CO depletion would be related to the CO snowline and chemical reactions in the disk, it also can be related to the dust gap structures (e.g., Nomura et al. 2016). However, the limit of observations on the resolution, it is still not clear.

Although some possible origins of these dust gap structures have been suggested, such as the planet-disk interaction, the molecular snowlines, the magnetohydrodynamic turbulence, and the photoevaporation (e.g., Nomura et al. 2016; Tsukagoshi et al. 2016; Andrews et al. 2016; Huang et al. 2018), there is no clear conclusion yet because of the lack of accurate constraints of the dust and gas properties around the gap structures derived from the observations. As I introduce in Section 1.2, each origin of the axisymmetric ring-gap structures requires different dust and gas properties to ignite their unique physical mechanisms and also as their products. Therefore, I need to derive the accurate dust and gas properties to distinguish the most plausible origin of the ring-gap structures. I will introduce the ALMA multiband analysis in Chapter 4 to estimate the dust and gas properties accurately from the ALMA observational data of the TW Hya disk. In a technical view, the ALMA multiband analysis has an advantage that there are no assumptions on the dust properties. Also, if the derived dust properties through the ALMA multiband analysis are accurate enough, those are used for the observational supports of the gap origins.

1.4 Scientific Goals

The main purpose of my Ph.D. thesis is addressing the following questions,

- What is the origin of axisymmetric ring-gap structures in protoplanetary disks?
- What kinds of observables are needed to distinguish the gap opening mechanisms?
- Is there any observational evidence supporting the dust growth and planet formation theories?

To address these questions, I focus on the derivation of the dust and gas properties around the gap structures from the ALMA observations. As Section 1.1.2 and 1.2 introduced, I need various information to reveal the origin of the ring-gap structures:

the temperature and density distribution of dust and gas materials, dust growths, and grain size distributions. By deriving the dust and gas properties from the ALMA observations, the theoretical and experimental studies can be examined by comparing the observed properties to the model expectations. Furthermore, if I derive those properties accurately, I try to examine the possible origins of the detected axisymmetric ring-gap structures in the PPDs.

I study two protoplanetary disks that have axisymmetric ring-gap structures using their high spatial resolution ALMA observations: the CR Cha disk (Kim et al. 2020) and the TW Hya disk (Kim et al. 2019). I apply different approaches to the CR Cha and TW Hya disks because two disks have different conditions (See Section 1.3) and different numbers of ALMA archival data. Since the CR Cha disk did not have a high spatial resolution image that can resolve disk substructures before, I adopt a new ALMA observation at Band 6 with a high spatial resolution to examine the existence of disk substructures (PI: Takayuki Muto, ALMA Project Code: 2017.1.00286.S). Using this data, I detect an axisymmetric dust ring-gap structure in the dust disk for the first time. Besides, the CO isotopologue (^{12}CO, ^{13}CO, and C^{18}) $J = 2$-1 emission lines in the same data show the smooth but more extended gas disk than the dust disk. There is a bump-like structure in the radial profile of the ^{13}CO peak brightness temperature at the radius of the observed dust ring. I investigate two possible mechanisms to examine the origin of the observed dust ring-gap structure in the CR Cha disk: (1) the gap opened by a planet and (2) the dust trapping at the gas pressure bump (Kim et al. 2020).

However, single wavelength data is limited to constrain the dust and gas properties because of the degeneracy of temperature T and optical depth τ_ν in the radiative transfer equation $I_\nu = B_\nu(T)[1 - \exp(-\tau_\nu]$. Therefore, I need to adopt the temperature assumption to derive the optical depth for the CR Cha disk. For constraining dust properties from the observational data without any assumptions, the multiwavelength analysis is essential. Unfortunately, the CR Cha disk does not have enough numbers of ALMA archival data to perform the multiwavelength analysis. Instead of the CR Cha disk, I choose the TW Hya disk for applying the multiwavelength analysis because it has enough numbers of ALMA archival data (Band 3, 4, 6, 7, 8, and 9). By adopting the method of Tsukagoshi et al. (2016), I establish the synthetic ALMA multiband analysis model for the TW Hya disk to find the best combination of three ALMA bands providing the most accurate dust properties without any assumptions on the dust temperature and the dust optical depth. And then, I apply the ALMA multiband analysis to the ALMA archival data to derive the dust properties and examine the consistency of the synthetic model (Kim et al. 2019). Through this analysis, I can directly derive the dust properties from the ALMA observations without any assumptions on the temperature and the optical depth. Also, I will try to examine the origin of the gap structure in the TW Hya disk by comparing the derived dust properties to the model expectation of possible origins.

In Chapter 2, I summarize the ALMA observations at Band 6 toward the CR Cha disk and present the images resolving disk substructures. Chapter 3 describes two possible mechanisms for explaining the observed disk substructures of the CR Cha disk by comparing it to the theoretical/numerical models. Next, I will explain the synthetic ALMA multiband analysis using the ALMA archival data of the TW Hya disk in Chapter 4 to overcome the limitations of the derivation of the dust properties with a single wavelength observation. In Chapter 5, I describe some future aspects of the ALMA multiband analysis. Finally, Chapter 6 summarizes all the results and interpretations in the previous chapters.

Chapter 2

ALMA observation toward the CR Cha protoplanetary disk

Recent ALMA surveys on PPDs in the nearby star-forming regions have revealed that the axisymmetric ring-gap structures are very common features in the disks (e.g., Andrews et al. 2018; Long et al. 2019). As I introduce in Section 1.3.1, the CR Cha disk is one of the strong candidates having disk substructures based on the discrepancy between the observed spectral index at mm-wavelengths and the extended dust continuum map of recent survey observation. If I detect any small-scale substructures in the disk, it enlarges the numbers of the disk samples that have substructures. Also, the previous ALMA survey observation indicates that the CR Cha disk has substantial dust and gas materials detected even in very short integration time ($\leq$ 240 s per each source; Long et al. 2017). It indicates that I can study more detailed dust and gas properties including diffuse extended structures even for the relatively short integration time.

Since all the ALMA archival data of the CR Cha disk are low spatial resolution data, I adopt a recent high-resolution ALMA observation to examine the existence of the small-scale substructures in the CR Cha disk. Using this data, I detect a dust ring-gap structure at the outer dust disk and a gas temperature bump at the dust ring region from the CO isotopologue emission lines (Kim et al. 2020). In this chapter, I will introduce the data reduction and imaging results of the recent high-resolution ALMA observation of the CR Cha disk.

2.1 Recent high-resolution ALMA Observation toward the CR Cha disk

Although there are some previous ALMA observations toward the CR Cha disk, those data are the survey data with the relatively short integration time and the low spatial resolution. Since the CR Cha disk is one of the candidates having a disk substructure, new high spatial resolution ALMA observation is needed to resolve the existence of the disk substructures. Therefore, I adopt a recent new observation at ALMA Band 6 with a very high spatial resolution (PI: Takayuki Muto, ALMA project code: 2017.1.00286.S).

Recent new ALMA observation toward the CR Cha protoplanetary disk was performed in November 2017 and March 2018 with 47 and 42 antennae respectively. The projected baselines of the ALMA configurations during the observations are covered from 12.54 m to 7.908 km, corresponding to the largest angular size of $\sim 5''$ and an angular resolution of $\gtrsim 0''.06$. The total execution time of observations is ~ 3.2 hours including the target on-source time of $\sim$ 2 hours. J1427-4206 and J0635-7516 are used as the bandpass and flux calibrators at the observations in November 2017 and March 2018, respectively. J1058-8003 is selected as a phase calibrator at both observations. The correlator setup has a total of four spectral windows (SPWs): Dust continuum emission is observed at 233 GHz (SPW1) and 217 GHz (SPW2) with 1.8 GHz bandwidth at each SPW. The SPW0 is centered at 230.538 GHz for the ^{12}CO $J = 2$-1 emission line. The SPW3 is divided into two parts to cover the ^{13}CO $J = 2$-1 emission at 220.398 GHz and the C^{18}O $J = 2$-1 emission at 219.560 GHz. The spectral resolution for three CO isotopologue emission lines is 61 kHz, corresponding to $\sim 0.08 \text{ km s}^{-1}$ in velocity.

The calibration processes of raw data are run through the ALMA calibration pipeline using the `CASA` package version 5.3. After the ALMA pipeline calibration, I make the images of the dust continuum and the CO isotopologue emission lines by the `CLEAN` command in the `CASA` package. The Briggs robust = 0 is adopted for the dust continuum image, obtaining the synthesized beam size of $\sim 0''.087 \times 0''.052$ and the beam position angle (PA) of $\sim 35^\circ.75$. The 1σ root-mean-square (RMS) level of the clean dust continuum map is ~ 0.0198 Jy beam^{-1} and the signal-to-noise ratio (SNR) of the peak intensity is ~ 220. Since the SNR of the dust continuum image is high enough ($\text{SNR} > 100$), I apply the phase-only self-calibration to the dust continuum image for improving the data quality. I adopt the solution interval of 'infinity' for phase self-calibration solution. Since the phase self-calibration solutions at the long baselines are flagged due to the low SNR < 3, I apply the solutions with an option `applymode=calonly` in the `applycal` command of the `CASA` package to keep the high spatial resolution of the dust continuum map. This mode applies the solution only for the short baseline data which has the SNR ≥ 3. By applying the phase-only self-calibration to the dust continuum data, the dust continuum image is improved $\sim 15\%$, showing the 1σ RMS level of $\sim 0.0178 \text{ mJy beam}^{-1}$ and the SNR ~ 261.

Meanwhile, the SNRs of the CO isotopologue emission lines are $\sim$ 5-7 with the synthesized beam size of $\sim 0''.080 \times 0''.047$ when the Briggs robust = 0 is applied. Therefore, I apply the Briggs robust = 2.0 (natural weighting) to the CO isotopologue

Table 2.1. The summary of new high-resolution ALMA observational data of the CR Cha disk

Species	$\nu_{\rm center}$ (GHz)	RMS in Cube (mJy beam^{-1})	RMS in Mom. 0 (mJy beam^{-1} km s^{-1})	Beam size (arcsec^2)	Beam PA (degree)
Dust	225	~ 0.0178		0.087×0.052	35.75
^{12}CO	230.538	~ 2.47	~4.594	0.188×0.128	0.635
^{13}CO	220.398	~ 2.40	~4.978	0.196×0.143	0.405
C^{18}O	219.560	~ 2.28	~3.441	0.194×0.142	0.976

emission lines for obtaining the high SNRs of $\sim$ 20-30. The synthesized beam sizes are $\sim 0''.188 \times 0''.128$ for the ^{12}CO line, $\sim 0''.196 \times 0''.143$ for the ^{13}CO line, and $\sim 0''.194 \times 0''.142$ for the C^{18}O line, respectively. The 1σ RMS level in the datacubes of the CO isotopologue lines is measured of $\sim 2.47~\mathrm{mJy~beam^{-1}}$ for the ^{12}CO line, $\sim 2.40~\mathrm{mJy~beam^{-1}}$ for the ^{13}CO line, and $\sim 2.28~\mathrm{mJy~beam^{-1}}$ for the C^{18}O line. Table 2.1 summarizes the 1σ RMS levels and the synthesized beam sizes of the dust continuum and the CO isotopologue emission lines of the CR Cha disk.

2.2 The high-resolution images of the CR Cha disk

As I described in Section 2.1, I make the high-resolution images of the CR Cha disk for the dust continuum and the CO isotopologue emission lines. Figure 2.1 shows the dust continuum image of the CR Cha disk at 225 GHz. The synthesized beam size of the dust continuum image is $0''.087 \times 0''.052$. It is presented in the bottom-left corner as filled white ellipse. There is a dust gap at $r \sim 90$ au and a faint dust ring just beyond the dust gap. The total flux density of the dust disk inside $r \leq 160$

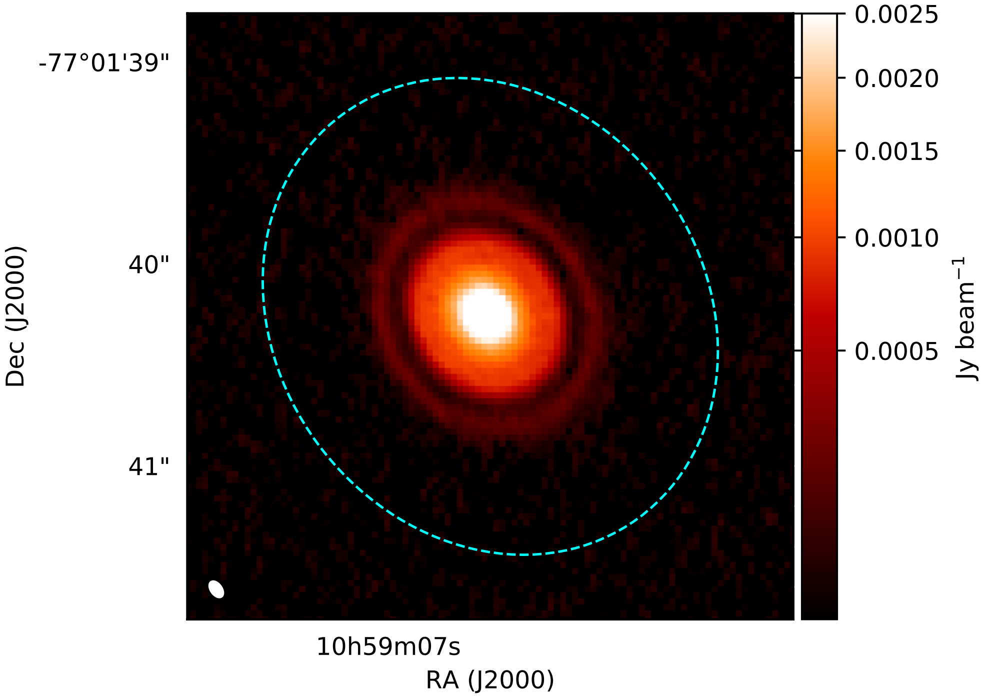

Figure 2.1. The dust continuum image of the CR Cha disk at 225 GHz. The synthesized beam size is presented as the filled white ellipse in the bottom-left corner, $\sim 0''.087 \times 0''.052$ (Briggs robust = 0). The right color bar indicates the intensity in Jy beam^{-1} units. There is a dust gap at $r = 90$ au and a faint dust ring beyond the dust gap. The cyan dashed contour indicates the outer edge of the CO gas disks at $r = 240$ au.

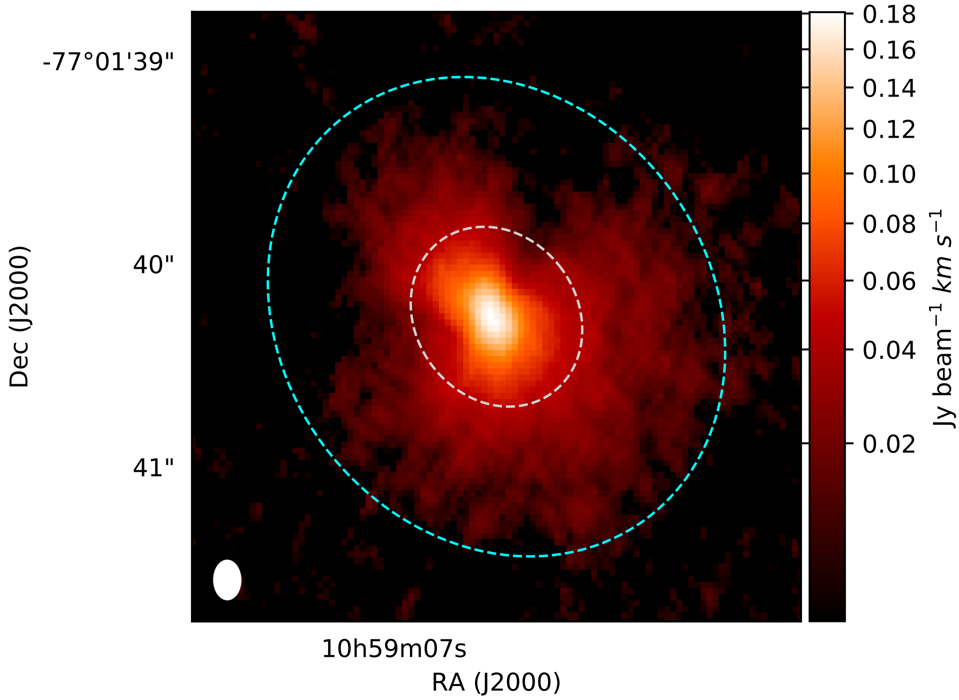

Figure 2.2. The moment 0 map of ^{12}CO $J = $ 2-1 line emission in the CR Cha disk. The synthesized beam size is presented as the filled white ellipse in the bottom-left corner, $\sim 0''.188 \times 0''.128$ (Briggs robust = 2). The right colorbar indicates the integrated intensities in Jy beam^{-1} km s^{-1} units. The white dashed contour indicates the location of the dust gap at $r = 90$ au. The cyan dashed contour indicates the outer edge of the CO gas disks at $r = 240$ au. There are two absorption features in the northern half-disk ($\phi \sim +10^\circ$ and $\phi \sim -90^\circ$ from the North in the counterclockwise).

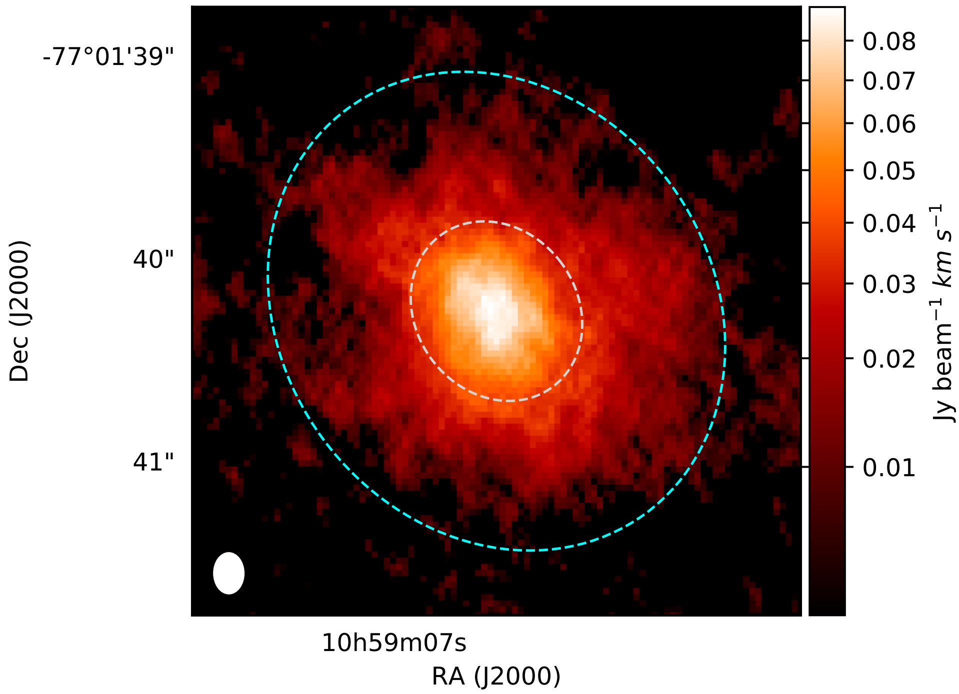

Figure 2.3. The moment 0 map of ^{13}CO J = 2-1 line emission in the CR Cha disk. The synthesized beam size is presented as the filled white ellipse in the bottom-left corner, $\sim 0''.196 \times 0''.143$ (Briggs robust = 2). The right colorbar indicates the integrated intensities in Jy beam^{-1} km s^{-1} units. The white dashed contour indicates the location of the dust gap at $r = 90$ au. The cyan dashed contour indicates the outer edge of the CO gas disks at $r = 240$ au.

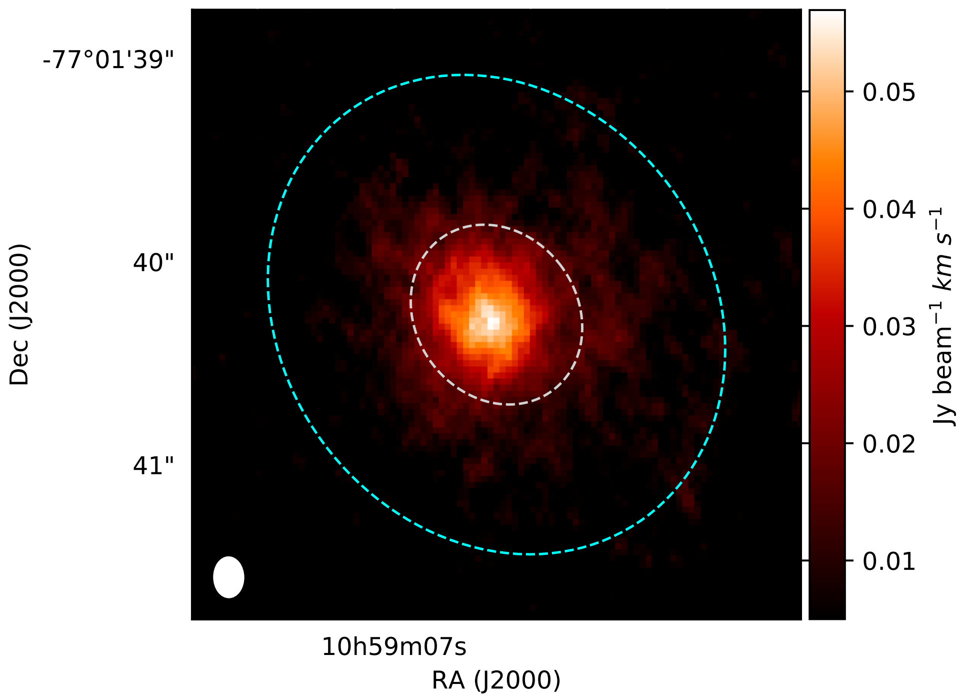

Figure 2.4. The moment 0 map of C^{18}O $J = 2$-1 line emission in the CR Cha disk. The synthesized beam size is presented as the filled white ellipse in the bottom-left corner, $\sim 0''.194 \times 0''.142$ (Briggs robust = 2). The right colorbar indicates the integrated intensities in Jy beam^{-1} km s^{-1} units. The white dashed contour indicates the location of the dust gap at $r = 90$ au. The cyan dashed contour indicates the outer edge of the CO gas disks at $r = 240$ au.

au is $F_{225\ \mathrm{GHz}} \sim 0.139$ Jy. It is consistent with the previous observation at 1.2 mm continuum of $F_{1.2\ \mathrm{mm}} \sim 0.125$ Jy (Ubach et al. 2012). The 1σ RMS level of the dust continuum image is ~ 0.0178 mJy beam^{-1}. The dust ring around $r \sim 120$ au is detected with $\sim 10\sigma$ detection on average. I also measure the disk geometry by the ellipse fitting using the `imfit` command in the `CASA` package at the image plane. The estimated inclination of the dust disk is $i \sim 31^\circ.0 \pm 1^\circ.4$ and PA is $\phi \sim 36^\circ.2 \pm 1^\circ.8$.

Figures 2.2-2.4 present the integrated intensity (moment 0) maps of the continuum subtracted ^{12}CO, ^{13}CO, and C^{18}O $J = 2$-1 transition line emissions, respectively. The white dashed contour presents the annulus at $r = 90$ au which is corresponding to the radius of the dust gap in Figure 2.1. The cyan dashed contour indicates the outer edge of the CO gas disk at $r = 240$ au. This radius corresponds to the detection limits of the CO isotopologue $J = 2$-1 emission lines, where the peak intensity at each pixel (the moment 8 maps; Figures 2.11 and 2.12) is ~ 7.5 mJy beam^{-1}, $\approx 3\sigma$ RMS level of the datacubes for the CO isotopologue lines. It indicates that the gas disk of the CR Cha disk is much extended than the dust disk.

Figure 2.2 shows two absorption features in the northern half-disk ($\phi \sim -10^\circ$ and $\phi \sim +90^\circ$ from the North in the counterclockwise). To verify the CO absorption feature, I draw the averaged spectra of the CO isotopologue lines in the entire gas disk. The solid lines in Figure 2.5 presents the averaged spectra of the ^{12}CO (top), the ^{13}CO (middle), and the C^{18}O (bottom) lines inside the disk radius of r ≤ 240 au, applying the disk inclination of 31° and the disk PA of $36^\circ.2$. The ^{12}CO and ^{13}CO line spectra show a strong absorption feature at the velocity of $v \sim 4.5$ km s^{-1}. The absorption feature in the C^{18}O line spectrum is less prominent than those of the ^{12}CO and ^{13}CO lines. These absorption features are also clearly seen in the channel maps of the ^{12}CO and ^{13}CO lines (Figures 2.6 and 2.7) in the velocity range of 3.3 km s^{-1} $\leq v \leq$ 5.6

(a) ^{12}CO spectrum

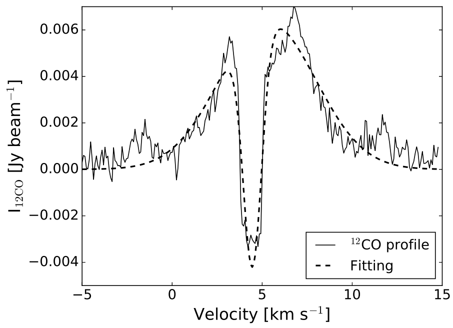

(b) ^{13}CO spectrum

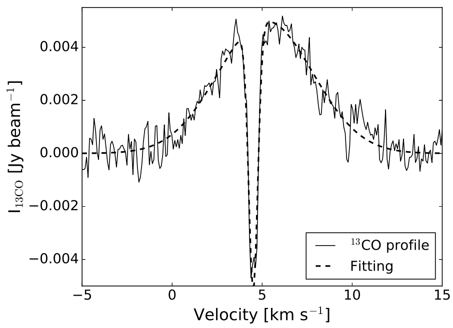

(c) C^{18}O spectrum

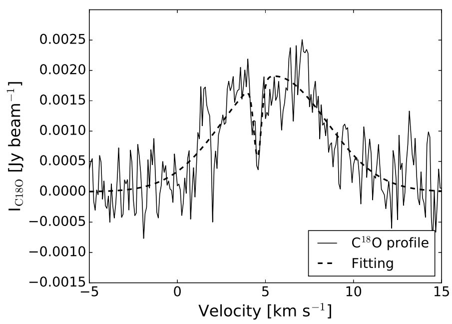

Figure 2.5. The averaged spectra (solid line) of the ^{12}CO (top), the ^{13}CO (middle), and the C^{18}O (bottom) J = 2-1 emission lines inside the disk radius of $r \leq 240$ au. The dashed lines in each panel are the fitting results by Equation 2.1, the emission and absorption lines of three CO isotopologue molecules. The emission lines are centered at $v_{\rm emit} \sim 5.3$ km s^{-1} with $\Delta v_{\rm emis}$ of ~ 2.7 km s^{-1} on average. The absorption lines are centered at $v_{\rm abs} \sim 4.5$ km s^{-1} with $\Delta v_{\rm abs}$ of ~ 0.2-0.5 km s^{-1}.

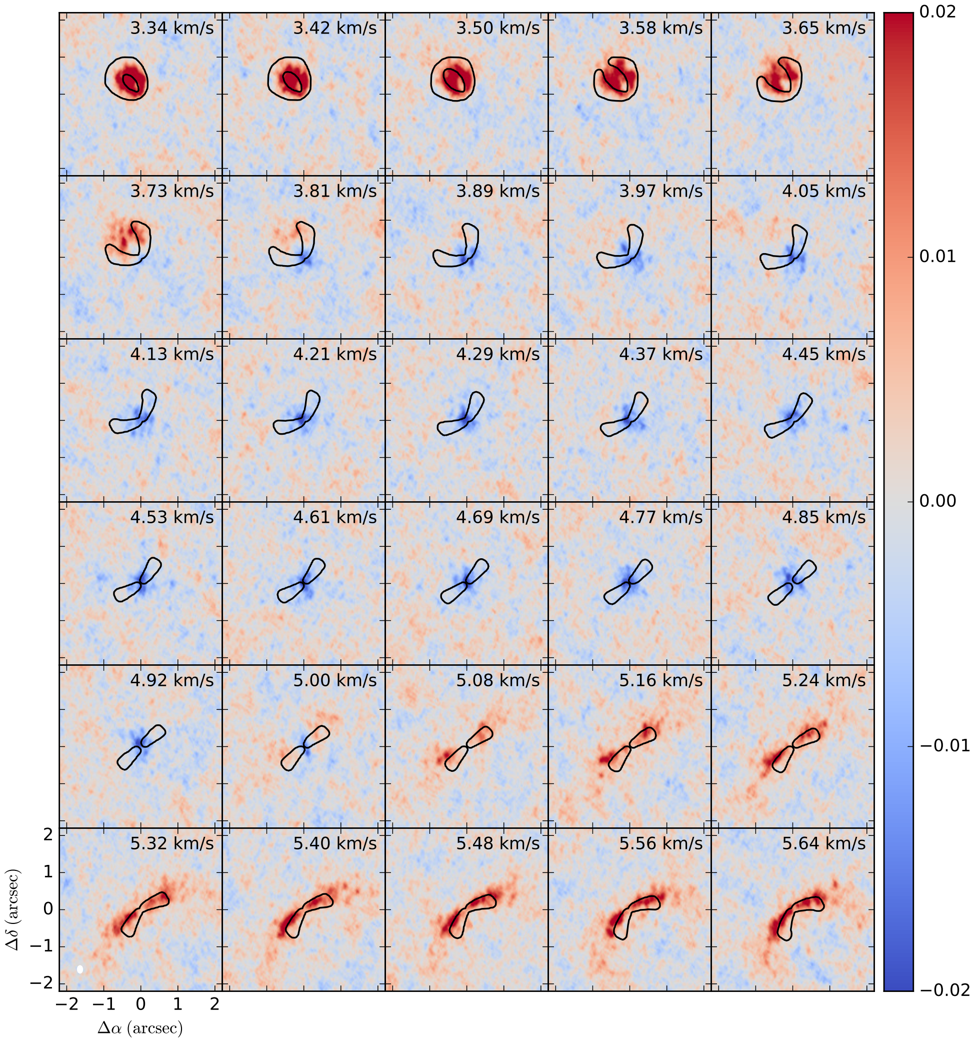

Figure 2.6. The channel maps of the ^{12}CO $J = 2$-1 emission line in the velocity ranges of 3.3 km s^{-1} to 5.6 km s^{-1}. The channels show that there are the absorption feature in the velocity ranges of 3.8 km s^{-1} $\leq v \leq$ 5.1 km s^{-1}. The black contour in each panel indicates the Keplerian rotation model adopting the disk inclination of 31° and the disk position angle of 36°.2.

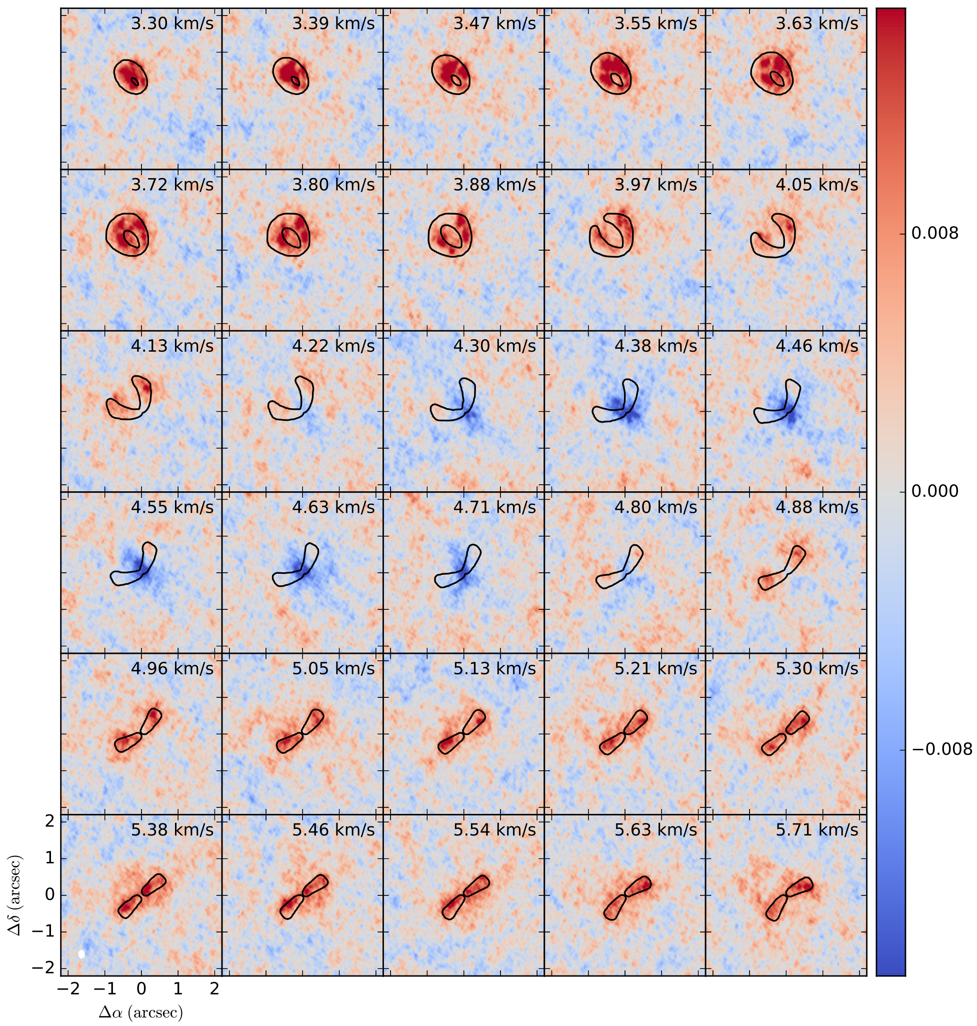

Figure 2.7. The channel maps of the ^{13}CO $J = 2$-1 emission line in the velocity ranges of 3.3 km s^{-1} to 5.7 km s^{-1}. The channels show that there are the absorption feature in the velocity ranges of 4.3 km s^{-1} $\leq v \leq$ 4.8 km s^{-1}. The black contour in each panel indicates the Keplerian rotation model adopting the disk inclination of 31° and the disk position angle of 36°.2.

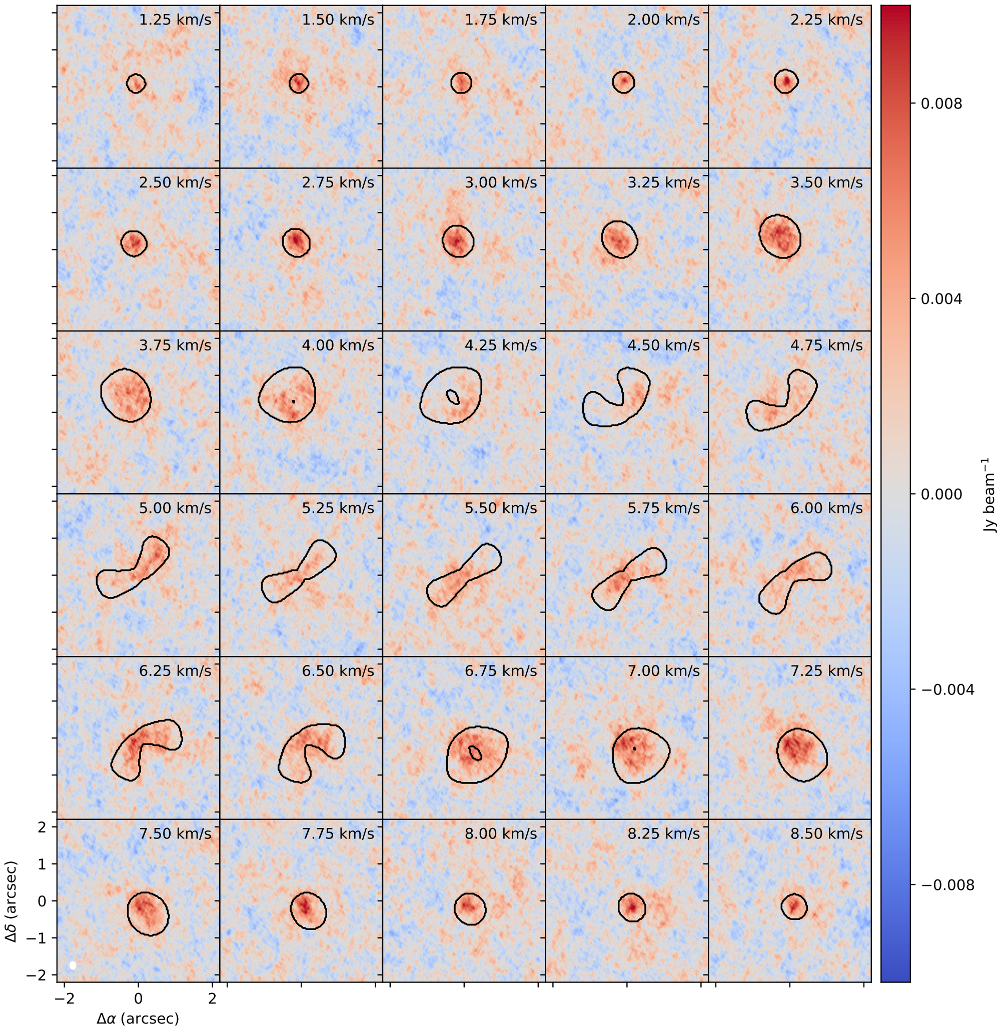

Figure 2.8. The channel maps of the $C^{18}O$ $J = 2$-1 emission line in the velocity ranges of 1.25 km s^{-1} to 8.5 km s^{-1} by smoothing three channels to one channel with the velocity resolution from $\Delta v \sim 0.08$ km s^{-1} to $\Delta v \sim 0.25$ km s^{-1} for increasing the SNR. There is no clear absorption feature in the velocity ranges of 4 km $s^{-1} \leq v \leq 5$ km s^{-1}. The black contour in each panel indicates the Keplerian rotation model adopting the disk inclination of 31° and the disk position angle of 36°.2.

km s^{-1} and the peak intensity (moment 8) maps of the ^{12}CO and ^{13}CO lines (Figures 2.11 and 2.12). In the channel maps of the CO isotopologue lines as shown in Figures 2.6-2.8, the black contours overlaid in each panel indicate the Keplerian rotation model adopting the stellar mass of 2 $M_{\odot}$, the disk inclination of 31°, and disk position angle of 36°.2. I note that I use the python code written by Kevin Flaherty for generating the Keplerian rotation model[1]. The Keplerian rotation model shows which regions are affected by these absorption features in the moment 0 and 8 maps of the CO isotopologue lines.

I perform the least mean square fitting for the CO isotopologue emission and absorption lines to measure their strengths, velocity centers, and widths. I use the summation of two Gaussian functions for the fitting:

$$I_\nu = A_{\rm emit} \exp\left(-\frac{(v - v_{\rm emis})^2}{2\Delta v_{\rm emis}^2}\right) + A_{\rm abs} \exp\left(-\frac{(v - v_{\rm abs})^2}{2\Delta v_{\rm abs}^2}\right). \tag{2.1}$$

The fitting parameters are summarized in Table 2.2. The dashed lines in Figure 2.5 show the fitting results of the emission and absorption lines of the CO isotopologue molecules. The fitting results indicate that the CO isotopologue emission lines are centered at $v_{\rm emit} \sim 5.3$ km s^{-1} with $\Delta v_{\rm emis}$ of ~ 2.7 km s^{-1} on average. The absorption features in the CO isotopologue lines are centered at $v_{\rm abs} \sim 4.5$ km s^{-1} with $\Delta v_{\rm abs}$ of $\sim$ 0.2-0.5 km s^{-1}. The foreground Cha I molecular clouds with a systematic velocity of $v_{\rm sys} \sim$ 4-5 km s^{-1} (e.g., Haikala et al. 2005; Long et al. 2017) would be the origin of the absorption features.

[1] https://github.com/kevin-flaherty/ALMA-Disk-Code/blob/master/makemask.py

Table 2.2. The fitting parameters for the spectra of the CO isotopologue lines in the CR Cha disk

Species	$A_{\rm emis}$ (mJy beam^{-1})	$v_{\rm emis}$ (km s^{-1})	$\Delta v_{\rm emis}$ (km s^{-1})	$A_{\rm abs}$ (mJy beam^{-1})	$v_{\rm abs}$ (km s^{-1})	$\Delta v_{\rm abs}$ (km s^{-1})
^{12}CO	6.37±0.22	5.30±0.07	2.67±0.07	-10.26±0.34	4.46±0.02	0.52±0.02
^{13}CO	5.00±0.11	5.19±0.06	2.64±0.06	-9.97±0.30	4.50±0.01	0.25±0.01
C^{18}O	1.90±0.08	5.51±0.13	2.96±0.13	-1.24±0.26	4.56±0.05	0.21±0.05

2.3 The azimuthally averaged intensity radial profiles

To investigate the radial structure of the CR Cha disk, I make the azimuthally averaged intensity radial profiles of Figures 2.1−2.4. The derived disk inclination of 31° and disk PA of 36°.2 are applied to calculate the projected disk radius of each pixel in the images. I azimuthally average every 8 au-width annulus inside of $r \leq 240$ au. As mentioned in Section 2.2, the CO isotopologue emission lines are affected by the foreground absorption of Cha I cloud in the northern half-disk against the disk minor axis. I azimuthally average only the southern half-disk ($126^\circ.2 \leq \phi \leq 306^\circ.2$) for the CO isotopologue lines to avoid the absorption features. Meanwhile, since the dust continuum is not affected by the line absorption, I average the full azimuthal angles for the dust continuum image.

Figure 2.9 presents the azimuthally averaged intensity radial profile of dust continuum (black) in Jy arcsec^{-2} units and the azimuthally averaged integrated intensity radial profiles of the ^{12}CO (red), ^{13}CO (green), and C^{18}O (blue) $J = $ 2-1 emission lines in Jy arcsec^{-2} km s^{-1} units. I note that I integrate the intensities of the CO isotopologue lines within the same velocity ranges of -1 km s^{-1} $\leq v \leq$ 12 km s^{-1}. The color-shaded regions indicate the uncertainties of the (integrated) intensity due to the azimuthal average at each annulus. As shown in Figure 2.1, there is a dust gap at $r \sim 90$ au and a dust ring at $r \sim 120$ au. Compared with the rapid drop of the dust continuum intensity around 90 au, the CO isotopologue emission lines are smoothly extended to $r \sim 240$ au.

I calculate the line ratios between the CO isotopologue molecules using the derived integrated intensity radial profiles in Figure 2.9. The line ratios can be used as a proxy of the optical depth of the lines. Figure 2.10 presents the ratios between the azimuthally averaged integrated intensities of the CO isotopologue emission lines: ^{13}CO/^{12}CO (green), C^{18}O/^{12}CO (red), and C^{18}O/^{13}CO (blue). The color-shaded regions indicate the uncertainties of the line ratios due to those of azimuthally averaged integrated intensities of the CO isotopologue molecules in Figure 2.9. I note that even if I derive these line ratios by dividing the moment 0 maps first and then averaging azimuthally, the results are identical inside of $r \leq 200$ au. The line ratios have very large uncertainties in the region outside of $r \geq 200$ au due to the weak emission lines compared to the noise levels.

The line ratios indicate that the ^{12}CO and ^{13}CO lines are optically thick. The measured line ratios between three CO isotopologue molecules are larger than 0.2 at all radii, which is larger than the typical molecular abundance ratios of ^{13}CO:^{12}CO = 1:67 and C^{18}O:^{13}CO = 1:7 in protoplanetary disks (e.g., Qi et al. 2011). When the molecular lines are optically thin, the line ratios should be almost the same as the abundance ratios because the line strength is directly proportional to the column density of the molecules, $I_\nu \propto B_\nu(T)\tau_\nu$ where B_ν is the Planck function at a given frequency ν. Meanwhile, when the lines are optically thick, the intensity at the line center becomes the same as the blackbody radiation, $I_\nu \propto B_\nu(T)$. Therefore, the intensities are proportional only to the temperature and independent of the optical depth, which is proportional to the column density of the molecules. In this case, the line ratios do not need to be similar to the abundance ratios of the molecules.

2.4 The peak brightness temperatures of the optically thick ^{12}CO and ^{13}CO lines

Since the brightness temperature of the optically thick ^{12}CO and ^{13}CO lines can be used as a proxy of gas temperature, I make the peak intensity (moment 8) maps of the ^{12}CO and ^{13}CO emission lines using the `immoments` command in the `CASA` package to derive the CO gas temperature at the line emitting regions. For making the moment 8 maps, I use the datacubes of the ^{12}CO and ^{13}CO emission lines without a dust continuum subtraction. In the case of optically thin lines, the observed intensity is considered as simply the summation of the dust continuum and the molecular line. Therefore, the continuum subtraction removes only the continuum component. In contrast, for the optically thick lines, the observed intensity is not simply described as the summation of the dust continuum and the line emissions. Therefore, the line plus continuum intensity should be used to derive the brightness temperature of line emitting molecules (e.g., Weaver et al. 2018).

Figures 2.11 and 2.12 present the moment 8 maps of the ^{12}CO and ^{13}CO line emissions including the dust continuum. The white and cyan dashed contours are the same as those in Figures 2.2$-$2.4. I azimuthally average only the southern half-disk of the moment 8 maps of the ^{12}CO and ^{13}CO lines to derive the peak intensity ($I_{\nu,\mathrm{peak}}$) radial profiles for avoiding the absorption features in the northern half-disk occurred by the foreground Cha I cloud. Figure 2.13 presents the $I_{\nu,\mathrm{peak}}$ radial profiles of the ^{12}CO

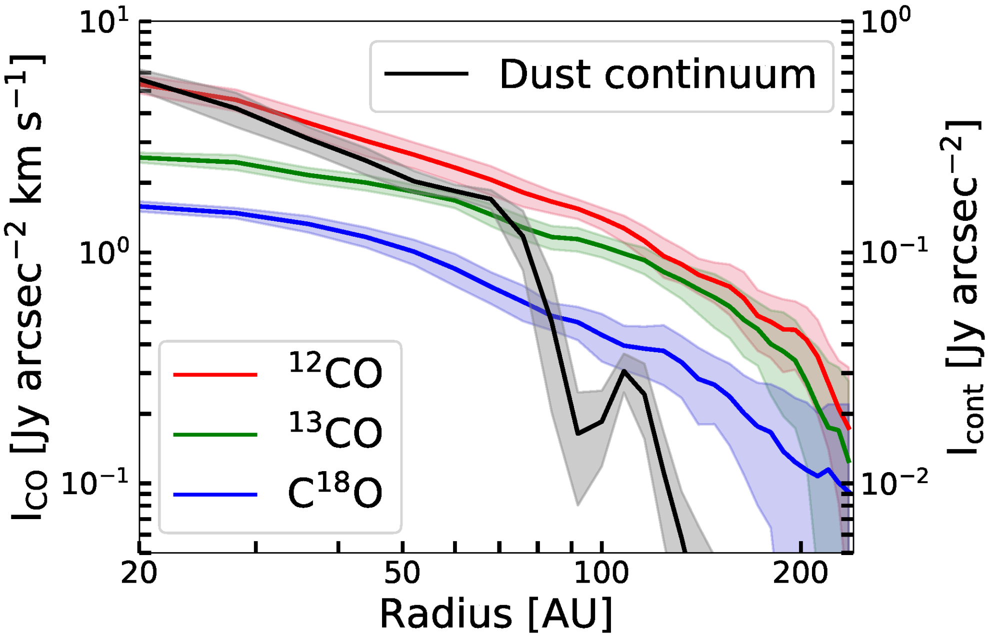

Figure 2.9. The azimuthally averaged radial profiles of the dust continuum emission (black) in Jy arcsec^{-2} units and the integrated intensities of the ^{12}CO (red), the ^{13}CO (green), and the C^{18}O (blue) emission lines in Jy arcsec^{-2} km s^{-1} units. The color-shaded regions indicate the uncertainties of the azimuthal average. The dust continuum emission shows a gap at $r \sim 90$ au and a ring at $r \sim 120$ au. Meanwhile, the CO isotopologue emission lines are smoothly extended to $r \sim 240$ au.

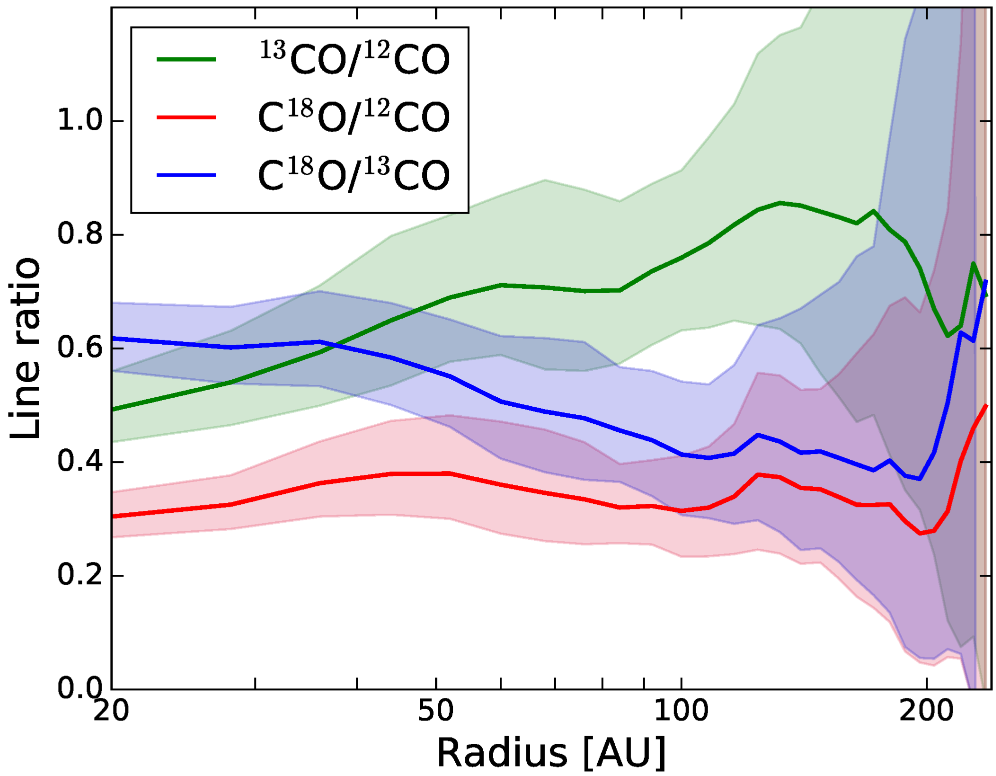

Figure 2.10. The line ratios between the CO isotopologue molecules: $^{13}CO/^{12}CO$ (green), $C^{18}O/^{12}CO$ (red), and $C^{18}O/^{13}CO$ (blue). The color-shaded regions indicate the uncertainties of the line ratios due to those of azimuthally averaged integrated intensities of the CO isotopologue molecules. All the line ratios are larger than 0.2 at all radii, which is the typical abundance ratios between the CO isotopologue molecules.

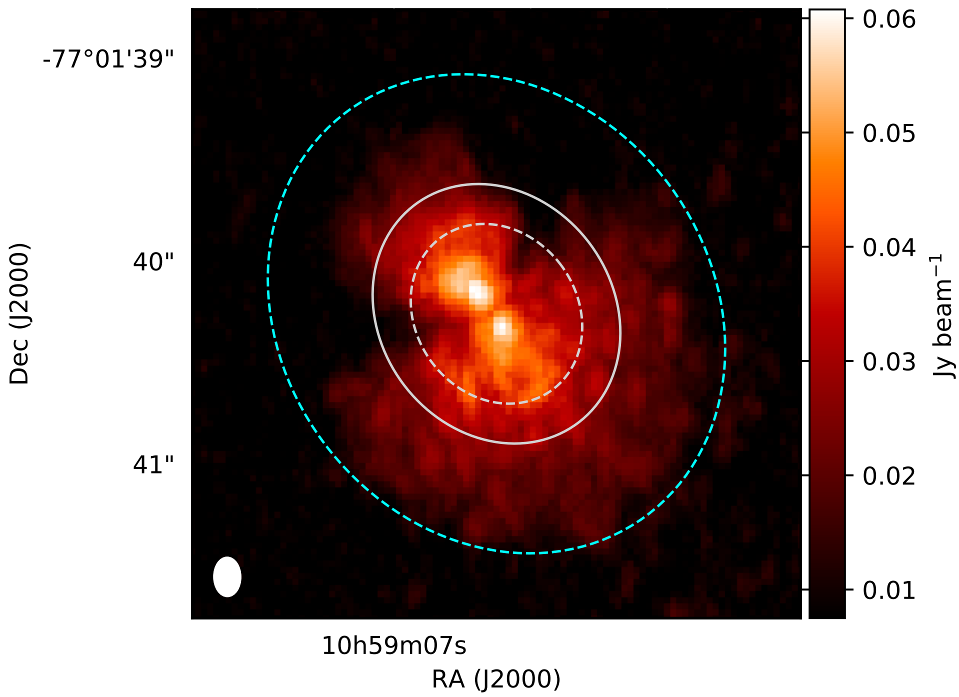

Figure 2.11. The moment 8 map of the ^{12}CO line emission with dust continuum. The absorption feature is seen in the northern half-disk ($\phi = -10°$ and $\phi = +90°$). The overlaid white and cyan dashed contours are the same as those in Figure 2.2. The white solid contour indicates the location of the bump in the azimuthally averaged ^{13}CO intensity radial profile at $r = 130$ au.

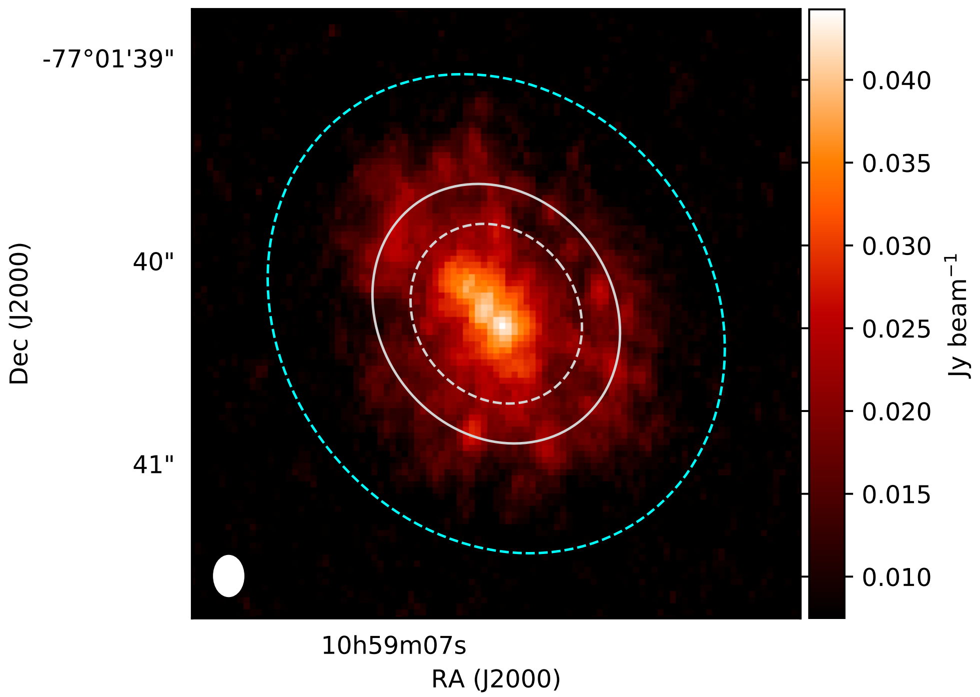

Figure 2.12. The moment 8 map of ^{13}CO line emission with dust continuum. The overlaid white and cyan dashed contours are the same as those in Figure 2.3. The white solid contour indicates the location of the bump in the azimuthally averaged ^{13}CO intensity radial profile at $r = 130$ au.

line (red) and the ^{13}CO line (blue) from the moment 8 maps. The color-shaded regions indicate the uncertainties of the $I_{\nu,\mathrm{peak}}$ due to the azimuthal average. The $I_{^{13}\mathrm{CO,peak}}$ radial profile shows a small bump around $r \sim 130$ au, corresponding to the radius of the dust ring beyond the dust gap.

I derive the peak brightness temperature ($T_{\mathrm{B,peak}}$) using the azimuthally averaged $I_{\nu,\mathrm{peak}}$ radial profiles of the ^{12}CO and ^{13}CO lines with the dust continuum by assuming $I_{\nu,\mathrm{peak}} = B_\nu(T_{\mathrm{B,peak}})$. Figure 2.14 presents the derived $T_{\mathrm{B,peak}}$ radial profiles of the line emitting ^{12}CO and ^{13}CO gases. The color-shaded regions are the uncertainties of the derived $T_{\mathrm{B,peak}}$ propagated from those of $I_{\nu,\mathrm{peak}}$ in Figure 2.13. As the same as $I_{^{13}\mathrm{CO,peak}}$ profile, there is a small bump at $r \sim 130$ au in the $T_{\mathrm{B,peak}}$ radial profile of the ^{13}CO gas. The white solid contour in Figures 2.11 and 2.12 indicates the location of the $T_{\mathrm{B,peak}}$ bump of ^{13}CO emission line at $r = 130$ au.

To quantify the $T_{\mathrm{B,peak},^{13}\mathrm{CO}}$ bump at $r \sim 130$ au, I perform the least squares fitting to the derived $T_{\mathrm{B,peak}}$ profiles of the ^{12}CO and ^{13}CO gases using the power-law profile with a single Gaussian function,

$$T_{\mathrm{B,peak}}(r) = A\left(\frac{r}{50\ \mathrm{au}}\right)^B + C\exp\left(-\frac{(r-D)^2}{2E^2}\right) \tag{2.2}$$

where A, B, C, D, and E are the fitting parameters. Using the $T_{\mathrm{B,peak}}$ profiles within 20 au $\leq r \leq$ 200 au, I obtain the fitting parameters, as listed in Table 2.3. The fitting parameters indicate that the small bump of $T_{\mathrm{B,peak},^{13}\mathrm{CO}}$ is centered at $r \sim 127$ au with $C \sim 4.3$ K amplitude, corresponding to $\sim 1.4\ \sigma$ detection at this radius ($1\sigma \approx 3$ K). The dashed lines in Figure 2.14 present the fitting results of the $T_{\mathrm{B,peak}}$ profiles of the ^{12}CO and ^{13}CO gases by inserting the numbers in Table 2.3 to Equation 2.2.

The $T_{\mathrm{B,peak}}$ profile derived from $I_{^{12}\mathrm{CO,peak}}$ also has a small bump at $r \sim 83$ au, the inner edge of the dust gap. It may be caused by a rapid decrease of the dust continuum

Table 2.3. The fitting parameters for the $T_{\mathrm{B,peak}}$ profiles of the ^{12}CO and ^{13}CO gases in the CR Cha disk.

Species	A (K)	B	C (K)	D (au)	E (au)
^{12}CO	37.57±1.38	−0.38±0.02	8.37±0.91	82.81±4.65	36.05±5.69
^{13}CO	28.29±0.38	−0.54±0.03	4.31±0.69	127.62±3.33	21.96±4.86

intensity around $r \sim 80$ au. The location of the photosphere of the ^{12}CO emission line could be changed inside and outside of the dust rich disk owing to the very steep gradients of the optical depth. The disk scale height could also be changed at the edge of the dense dust disk (see Section 3.4). The difference between the $T_{\mathrm{B,peak}}$ profiles of the ^{12}CO and ^{13}CO gases can be a hint for revealing the temperature and density distributions of the gas disk.

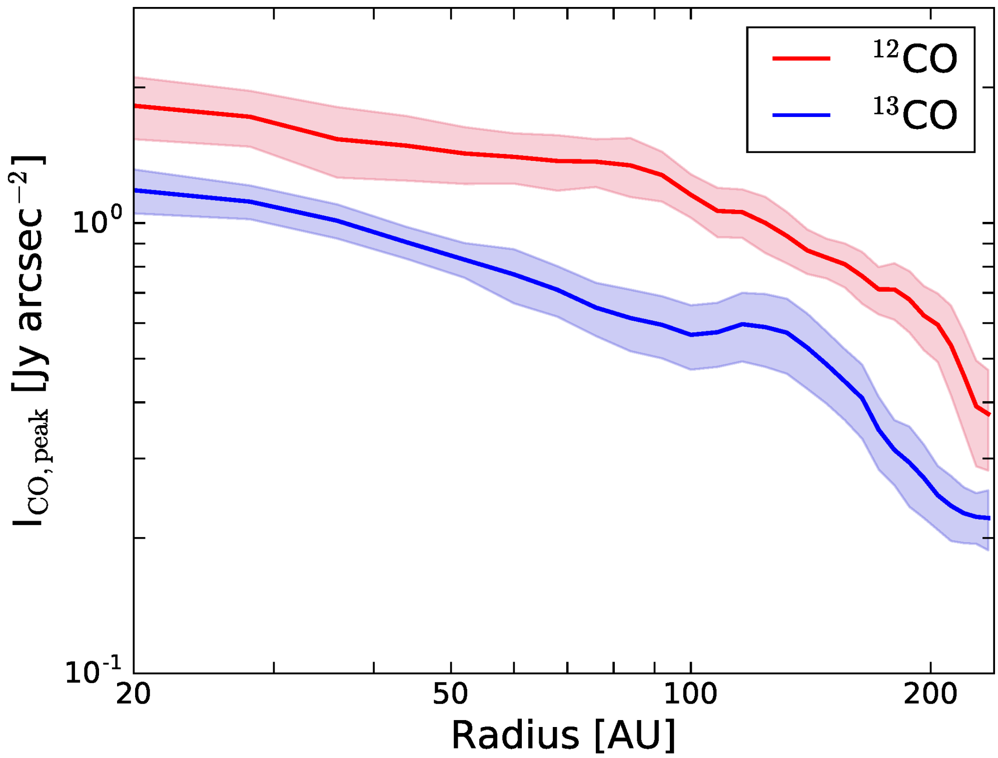

Figure 2.13. The azimuthally averaged radial profiles of the $I_{\nu,\mathrm{peak}}$ of the ^{12}CO (red) and ^{13}CO (blue) emission lines in the southern half-disk. The color-shaded regions indicate the uncertainties of $I_{\nu,\mathrm{peak}}$ owing to the azimuthal average. There is a small bump in $I_{^{13}\mathrm{CO,peak}}$ around $r \sim 130$ au.

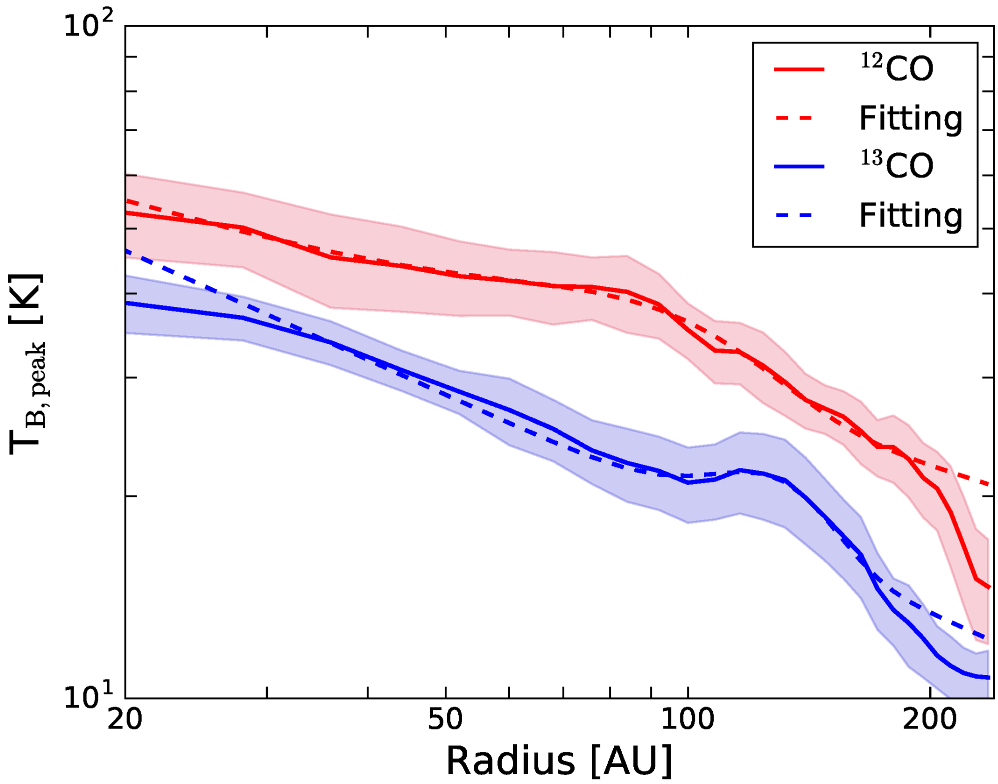

Figure 2.14. The radial profiles of the $T_{\rm B,peak}$ derived from the $I_{\nu,\rm peak}$ profiles of the ^{12}CO (red) and ^{13}CO (blue) emission lines in Figure 2.13. The color-shaded regions indicate the uncertainties of $T_{\rm B,peak}$ propagated from those of $I_{\nu,\rm peak}$. The dashed lines present the lease squares fitting results by inserting the numbers in Table 2.3 to Equation 2.2. The derived $T_{\rm B,peak}$ from the $I_{^{13}\rm CO,peak}$ profile also shows a small bump at $r \sim 130$ au.

Chapter 3

Two possible origins of the ring-gap structure in the CR Cha disk

In Chapter 2, I introduce the new high-resolution ALMA observational results of the CR Cha disk. There are a dust ring-gap structure and a gas temperature bump at the dust ring location. As I introduce in Section 1.2, there are some possible scenarios to explain the origin of the observed disk substructures in the CR Cha disk. The previous studies suggested two possible mechanisms in their papers (e.g., Ribas et al. 2017; Ubach et al. 2017): a dust gap opened by a planet (e.g., Zhu et al. 2012) and the dust trapping at the gas pressure bump (e.g., Pinilla et al. 2012). In this chapter, I derive the detailed dust ring-gap structure and the gas density distribution from new high-resolution ALMA observational data. Then, I examine the suggested two possible origins from the previous studies by comparing the observed dust and gas properties to the model expectations (Kim et al. 2020).

3.1 The dust gap structure in the CR Cha disk

To analyze the observed dust gap structure in the CR Cha disk, I derive the radial profile of dust surface density ($\Sigma_{\rm dust}$) from the observed dust continuum intensity ($I_{\rm cont}$). First, I derive the optical depth at 225 GHz ($\tau_{225\ {\rm GHz}}$) using the radiative transfer equation, $I_{\rm cont} = B_{225\ {\rm GHz}}(T_{\rm dust})\,[1 - \exp\,(-\tau_{225\ {\rm GHz}})]$. I simply assume that the dust temperature is equal to the $T_{\rm B,peak}$ of the ^{12}CO or ^{13}CO line in Figure 2.14, that is, $T_{\rm dust} = T_{\rm gas} = T_{\rm B,peak}$. Since both CO lines are optically thick, I can use the derived $T_{\rm B,peak}$ profiles as the gas temperature $T_{\rm gas}$ of the ^{12}CO and ^{13}CO line emitting regions. And then, I derive the dust surface density $\Sigma_{\rm dust}$ using the equation $\tau_{225\ {\rm GHz}} = \kappa_{225\ {\rm GHz}}\Sigma_{\rm dust}$ where $\kappa_{225\ {\rm GHz}} = 2.3$ cm^2 g^{-1} is the dust opacity at 225 GHz (e.g., Beckwith et al. 1990).

The solid lines in Figure 3.1 indicate the derived $\tau_{225\ {\rm GHz}}$ and $\Sigma_{\rm dust}$ radial profiles when I adopt $T_{\rm dust} = T_{\rm B,peak,^{12}CO}$ (red) and $T_{\rm dust} = T_{\rm B,peak,^{13}CO}$ (blue). The color-shaded regions indicate the uncertainties of $\tau_{225\ {\rm GHz}}$ and $\Sigma_{\rm dust}$ propagated from the uncertainties of the $T_{\rm B,peak}$ in Figure 2.14. Although I simply assume $T_{\rm dust} = T_{\rm gas}$ in this calculation, the $T_{\rm dust}$ near the disk midplane could be lower than the $T_{\rm gas}$ of the ^{12}CO or ^{13}CO line emitting regions (see Section 3.4.2). Then, the $\Sigma_{\rm dust}$ values derived from this assumption would be lower than the real dust surface density.

To make an accurate fitting of the gap structure, I need to make the least squares fitting of the baseline to the derived $\Sigma_{\rm dust}$ profile first. I adopt the power-law function with an exponential tail for the baseline,

$$\Sigma_{\rm d,baseline} = A\left(\frac{r}{50\ {\rm au}}\right)^{-0.5}\ \exp\left[-\left(\frac{r}{100\ {\rm au}}\right)^4\right] \tag{3.1}$$

where $A = 0.09$ g cm^{-2} for $T_{\rm dust} = T_{\rm B,peak,^{12}CO}$ and $A = 0.13$ g cm^{-2} for $T_{\rm dust} =$

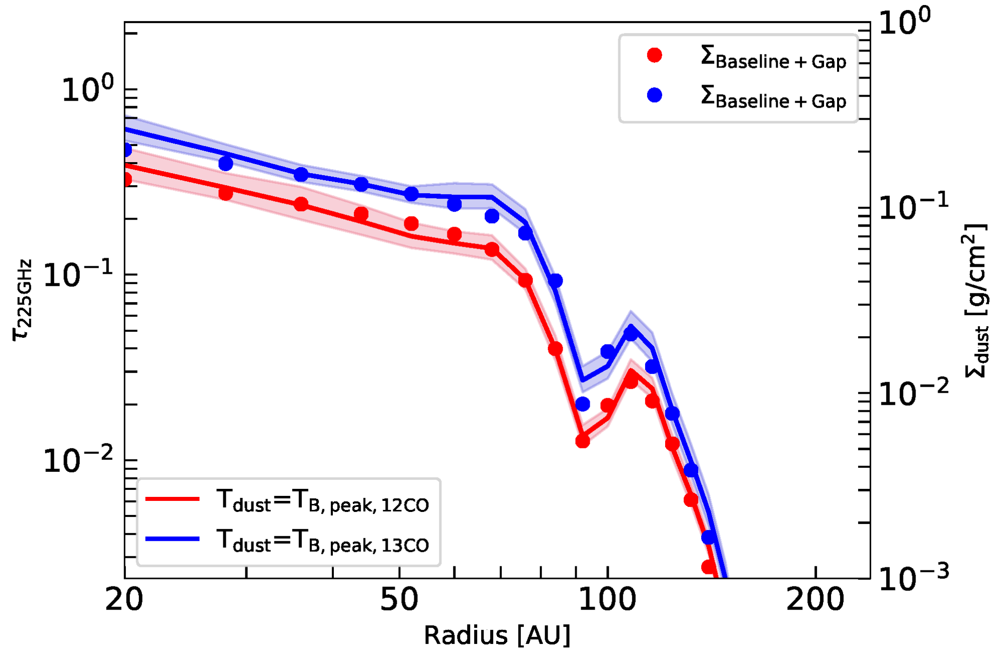

Figure 3.1. The radial profiles of the optical depth at 225 GHz ($\tau_{225\ \mathrm{GHz}}$) and the dust surface density (Σ_{dust}), where $\tau_{225\ \mathrm{GHz}} = \kappa_{225\ \mathrm{GHz}}\Sigma_{\mathrm{dust}}$ with the constant $\kappa_{225\ \mathrm{GHz}} = 2.3\ \mathrm{cm}^2\ \mathrm{g}^{-1}$. The solid lines present the derived $\tau_{225\ \mathrm{GHz}}$ and Σ_{dust} profiles when I adopt the $T_{\mathrm{B,peak}}$ of the ^{12}CO (red) and ^{13}CO (blue) gases as T_{d}. The color-shaded regions indicate the uncertainties propagated from the uncertainties of the $T_{\mathrm{B,peak}}$ in Figure 2.14. The dotted lines indicate the fitting results of the baseline and dust gap structure expressed by Equations 3.1 and 3.2 with the same color indications. Table 3.1 summarizes the fitting parameters for Equation 3.2.

Table 3.1. The fitting parameters for the dust gap in the CR Cha disk

$T_{\rm dust}$	$r_{\rm cent}$ (au)	Δr (au)	$\Sigma_{\rm peak}$ (g cm^{-2})	Depth (%)
$T_{\rm B,peak.^{12}CO}$	88.94	9.74	0.028	$\sim$ 21.71
$T_{\rm B,peak.^{13}CO}$	91.47	6.72	0.038	$\sim$ 19.94

$T_{\rm B,peak,^{13}CO}$. The mass of dust disk inside of 100 au based on Equation 3.1 is $M_{\rm dust} \sim 79\ M_\oplus$ where $M_\oplus$ is Earth mass. I note that the shape of Equation (3.1) is derived by the least squares fitting to the derived $\Sigma_{\rm dust}$ profiles except the radius ranges of 70 au $\leq r \leq$ 110 au. And then, I choose concrete numbers within the uncertainties of the fitting parameters. After subtracting the baseline from the derived $\Sigma_{\rm dust}$ profiles, the gap structure is fitted with a single Gaussian function of

$$\Sigma_{\rm d,gap} = \Sigma_{\rm peak} \exp\left[\frac{(r - r_{\rm cent})^2}{2(\Delta r)^2}\right]. \tag{3.2}$$

Table 3.1 summarizes the fitting parameters for the gap structure. The uncertainties of the fitting parameters are not listed in the table because they are more than 500% for all the parameters because only 2-3 data points are included in the gap structure of $\sim$ 20 au width.

The dotted lines in Figure 3.1 indicate the fitting results of the baseline and the dust gap structure. The fitting results indicate that the dust gap is centered at $r_{\rm cent} \sim 90$ au and has a width of $\Delta r \sim 8$ au on average. The gap depth is measured as

$$\frac{\Sigma_{\rm d,baseline}(r_{\rm cent}) - \Sigma_{\rm peak}}{\Sigma_{\rm d,baseline}(r_{\rm cent})}, \tag{3.3}$$

the ratio between the bottom of the gap and the baseline value at the gap center $r_{\rm cent}$. The derived gap depth is $\sim 20\%$ on average. I note that the derived gap depth should be regarded as the upper limit because the synthesized beam size ($\sim$ 16 au) is comparable to the estimated total gap width of $2\Delta r \sim 16$ au. As an example, Isella et al. (2016) finds the degeneracy between the gap depth and width at a low angular resolution ($\sim 0''.2$) data of the HD 163296 disk: The observed intensity profile can be reproduced by both a shallow wide gap or a deep narrow gap. The later observation of HD 163296 disk with high angular resolution ($\sim 0''.05$, Isella et al. 2018) shows that the gap is deeper than that observed with low angular resolution.

3.2 The $C^{18}O$ gas column density

For understanding the origin of the observed disk substructures and the gas temperature bump around $r \sim 130$ au, the gas distribution is essential information. In this section, I analyze the CO gas density distribution in the CR Cha disk from the observed optically thin $C^{18}O$ line emission. I adopt the following equation in Yamamoto (2017) to derive the $C^{18}O$ column density ($N_{C^{18}O}$):

$$\begin{aligned}\int \tau_\nu \, dv &\approx \sqrt{2\pi}\, \tau_{\nu,\rm peak} \Delta v \\ &= \frac{8\pi^3 S \mu_0^2}{3hU(T_{\rm gas})} \left[\exp\left(\frac{h\nu}{k_{\rm B}T_{\rm gas}}\right) - 1\right] \exp\left(-\frac{E_{\rm u}}{k_{\rm B}T_{\rm gas}}\right) N_{\rm molecule}\end{aligned} \tag{3.4}$$

where $\tau_{\nu,\rm peak}$ is the peak optical depth of the molecular line at the line center, Δv is the width of the molecular line, S is the molecular line strength, μ_0 is the permanent dipole moment of the molecule, h is the Planck constant, $U(T_{\rm gas})$ is the rotational partition function of the molecular species at a given gas temperature $T_{\rm gas}$, ν is the rest frequency of the molecular transition line, $k_{\rm B}$ is the Boltzmann constant, $E_{\rm u}$ is the upper state energy level, and $N_{\rm molecule}$ is the column density of the molecule, respectively. I simply assume that the $\rm C^{18}O$ line has a Gaussian profile. Then, by adopting the approximation of the integrated area of the Gaussian function as $\int \tau_\nu \, dv \approx \sqrt{2\pi}\tau_{\rm C^{18}O,peak}\Delta v$, I can derive $N_{\rm C^{18}O}$ by inserting the peak optical depth $\tau_{\nu,{\rm peak}}$, which is derived from the peak intensity $I_{\rm C^{18}O,peak}$, and the width of Δv of the $\rm C^{18}O$ line spectrum into Equation 3.4. Those two parameters are obtained by the Gaussian fitting on the $\rm C^{18}O$ line spectrum. For the $\rm C^{18}O$ J = 2-1 transition line, I use ν = 219.5603 GHz, $S\mu_0^2 = 0.02440\, D^2 \approx 2.440{\times}10^{-51}$ J $\cdot$ m^3, and $E_{\rm u}/k_{\rm B} = 15.80580$ K from the Leiden Atomic and Molecular Database (Schöier et al. 2005) and Cologne Database for Molecular Spectroscopy (Müller et al. 2001). The rotational partition function $U(T_{\rm gas})$ of $\rm C^{18}O$ molecule is approximated as $U(T_{\rm gas}) \approx 0.38\,(T_{\rm gas} + 0.88)$ (Mangum & Shirley 2017).

As a first step, I obtain the $I_{\rm C^{18}O,peak}$ and the $\Delta v_{\rm C^{18}O}$ by performing the least-squares fitting to the azimuthally averaged and velocity corrected $\rm C^{18}O$ line spectra using a Gaussian function. When I azimuthally average the $\rm C^{18}O$ line spectra, I correct the velocity offset of the line center at each pixel (mainly due to Doppler shift by the Keplerian rotation) by using the intensity-weighted velocity (moment 1) map of the $\rm C^{18}O$ line. Then, I derive the $\tau_{\rm C^{18}O,peak}$ using the radiative transfer equation, $I_{\rm C^{18}O,peak} = B_{\rm C^{18}O}(T_{\rm gas})\left[1 - \exp(-\tau_{\rm C^{18}O,peak})\right]$, with $T_{\rm gas} = T_{\rm B,peak,^{13}CO}$, the blue line in Figure 2.14.

The solid line in Figure 3.2 presents the derived $\tau_{\rm C^{18}O,peak}$ radial profile. The gray-shaded region shows the uncertainty of the $\tau_{\rm C^{18}O,peak}$. The dotted line with error bars in Figure 3.2 shows the fitted $\Delta v_{\rm C^{18}O}$. The decrease of $\tau_{\rm C^{18}O}$ in the inner disk is caused by the line broadening. Since the Keplerian rotation velocity is faster and the gradient of velocity along the line of sight is steeper in the inner disk than the outer disk, the beam

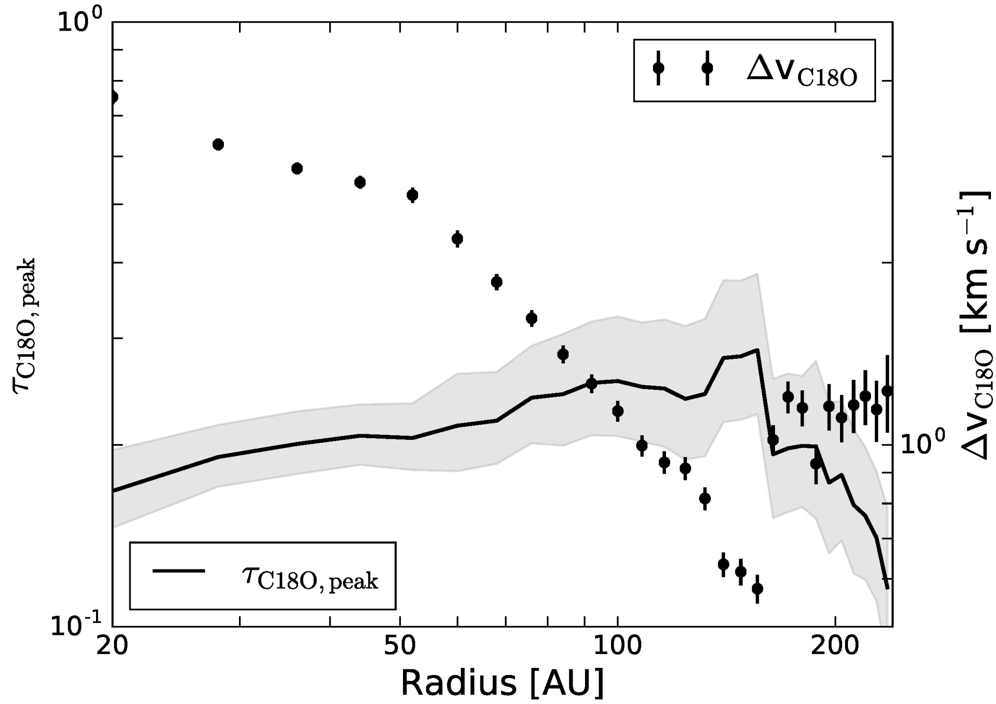

Figure 3.2. The radial profiles of the $\tau_{\rm C^{18}O,peak}$ and $\Delta v_{\rm C^{18}O}$. The solid line indicates the derived $\tau_{\rm C^{18}O,peak}$. The gray-shaded regions indicate the uncertainties of the $\tau_{\rm C^{18}O,peak}$. The dotted line with error bars indicates the $\Delta v_{\rm C^{18}O}$ of the azimuthally averaged $C^{18}O$ line spectra. The $\tau_{\rm C^{18}O,peak}$ in the inner disk decreases because of the line broadening caused by the Doppler shifts corresponding to the high rotation velocity in the inner disk. This line broadening leads to the flat distribution of the $\tau_{\rm C^{18}O,peak}$ in the inner disk.

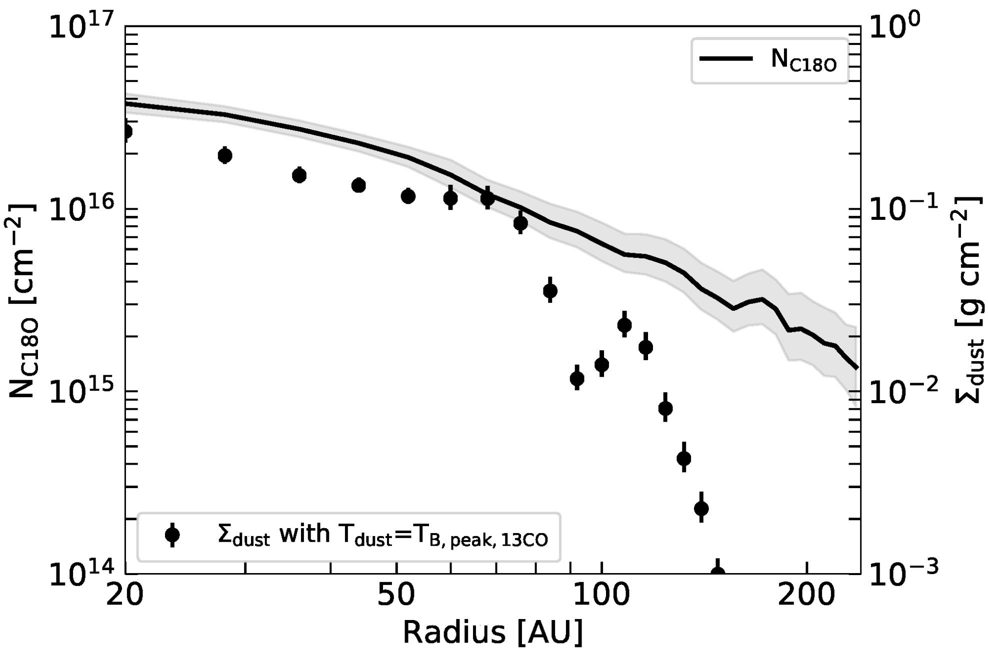

Figure 3.3. The radial profiles of the derived $C^{18}O$ column density $N_{C^{18}O}$ and dust surface density Σ_{dust}. The solid line indicates the $N_{C^{18}O}$ radial profile. Their uncertainty is represented as the gray-shaded region. The dotted line with error bars indicates the Σ_{dust} profile derived with $T_{dust} = T_{B,peak,^{13}CO}$. It presents that the dust disk is compact than the gas disk.

averaged line width becomes broader in the inner disk. Because of this line broadening, the derived $\tau_{\mathrm{C^{18}O,peak}}$ radial profile is nearly flat up to $r \sim 160$ au but the derived $\Delta v_{\mathrm{C^{18}O}}$ profile rapidly decreases in the same region. In the outer disk of $r \geq 160$ au, the Gaussian fitting on the $\mathrm{C^{18}O}$ line spectra is affected by the noise next to the $\mathrm{C^{18}O}$ line signal making the broader line width and the smaller peak intensity. It makes the drop of $\tau_{\mathrm{C^{18}O,peak}}$ at $r > 160$ au.

Finally, I derive the $\mathrm{C^{18}O}$ column density ($N_{\mathrm{C^{18}O}}$) by inserting the derived $\tau_{\mathrm{C^{18}O,peak}}$, $\Delta v_{\mathrm{C^{18}O}}$, and $T_{\mathrm{gas}} = T_{\mathrm{B,peak,^{13}CO}}$ into Equation 3.4. Figure 3.3 presents the derived $N_{\mathrm{C^{18}O}}$ profile as a solid line and their uncertainties as gray-shaded regions. The dotted line with error bars in Figure 3.3 indicates the derived Σ_{dust} profile. Compared with the Σ_{dust} profile, the $\mathrm{C^{18}O}$ gas disk is much extended than the dust disk. There is no gas gap around the dust gap at $r \sim 90$ au owing to the large synthesized beam size of the line observation ($\sim 0''.2$ corresponding to ~ 36 au in the physical scale at the distance of $d \sim 187.5$ pc).

Additionally, I can estimate the grain size from the size difference between the dust and gas disks. If the grains are drifted $\Delta r \sim 150$ au during their age $t \sim 1$ Myr, the average radial drift velocity $v_{\mathrm{r,ave}} = \Delta r/t \sim 71.11$ cm s^{-1}. Theoretically, the v_{r} is expressed as $v_{\mathrm{r}} = 2\eta v_{\mathrm{K}} St/(1 + St^2)$, where $\eta \sim (c_{\mathrm{s}}/v_{\mathrm{K}})^2$ and the Stokes number $St = \pi \rho_{\mathrm{d}} a / 2\Sigma_{\mathrm{gas}}$ (e.g., Birnstiel et al. 2012; Ormel & Liu 2018). For the CR Cha disk, the Keplerian rotation velocity is $v_{\mathrm{K}} \sim 4.07$ km s^{-1} and $T_{\mathrm{gas}} \sim 22.36$ K at $r = 90$ au. Then, the sound speed at $r = 90$ au is $c_{\mathrm{s}} \sim 273$ m s^{-1} so that the $\eta \sim 0.0045$. Therefore, the Stokes number is derived as $St \sim 0.02$. From the derived $N_{\mathrm{C^{18}O}}$ profile, I derive the $\Sigma_{\mathrm{gas}} = 28\, m_{\mathrm{H}} \times 444 \times 10^4 \times N_{\mathrm{C^{18}O}} \sim 1.7$ g cm^{-2} at $r = 90$ au by assuming the CO molecular mass is 28 m_{H}, the abundance ration of ^{12}CO/C^{18}O $= 444$ (Qi et al. 2011), and $\Sigma_{\mathrm{H_2}}/\Sigma_{\mathrm{CO}} = 10^4$. If I assume the compact dust grain with the $\rho_{\mathrm{d}} = 1$ g cm^{-3}, the grain size $a \sim 200$ μm for the $St \sim 0.02$. This grain size is consistent with the recent ALMA polarization observations at mm-wavelengths, the maximum grain size in the outer disk regions is $a_{\rm max} \sim 100$ μm for some PPDs (e.g., Kataoka et al. 2015, 2017).

3.3 The dust-to-CO-gas mass ratio

The dust-to-gas mass ratio is one of the important parameters to understand the physical and chemical status of the materials in PPDs. Based on the derived radial profiles of the $\Sigma_{\rm dust}$ and the $N_{\rm C^{18}O}$ in Figure 3.3, I derive the dust-to-CO-gas mass ratios of the CR Cha disk in this section.

By adopting the factor $X \equiv N_{\rm CO}/N_{\rm H_2}$, the ratio of the number density between CO and H_2 gas molecules, and $\epsilon \equiv \Sigma_{\rm dust}/\Sigma_{\rm H_2}$, the dust to gas mass ratio, I derive the dust-to-CO-gas mass ratio as following equation,

$$\frac{\epsilon}{X} = \frac{\Sigma_{\rm dust}}{\Sigma_{\rm H_2}}\frac{N_{\rm H_2}}{N_{\rm CO}} = \frac{\Sigma_{\rm dust}}{2m_{\rm H}N_{\rm CO}} = 14\,\frac{\Sigma_{\rm dust}}{\Sigma_{\rm CO}} \tag{3.5}$$

where $\Sigma_{\rm H_2} = 2m_{\rm H}N_{\rm H_2}$, $\Sigma_{\rm CO} = 28m_{\rm H}N_{\rm CO}$, and $m_{\rm H} = 1.67 \times 10^{-24}$ g is the mass of hydrogen atom. If I adopt the typical abundance ratio of $^{12}{\rm CO}/{\rm C}^{18}{\rm O} = 444$ (e.g., Qi et al. 2011), the ^{12}CO number density ($N_{\rm CO}$) is derived by the conversion of $N_{\rm CO} = 444\ N_{\rm C^{18}O}$. I also adopt the typical values in the ISM of $X_0 = 10^{-4}$ and $\epsilon_0 = 10^{-2}$ for the comparison to the typical dust-to-CO-gas mass ratio in the interstellar medium (ISM).

Figure 3.4 presents the radial profile of the normalized dust-to-CO-gas mass ratio $(\epsilon/X)\,/\,(\epsilon_0/X_0)$, indicating how much the dust-to-CO-gas mass ratio of the CR Cha disk deviates from the typical ISM value. The gray-shaded region indicates the uncer-

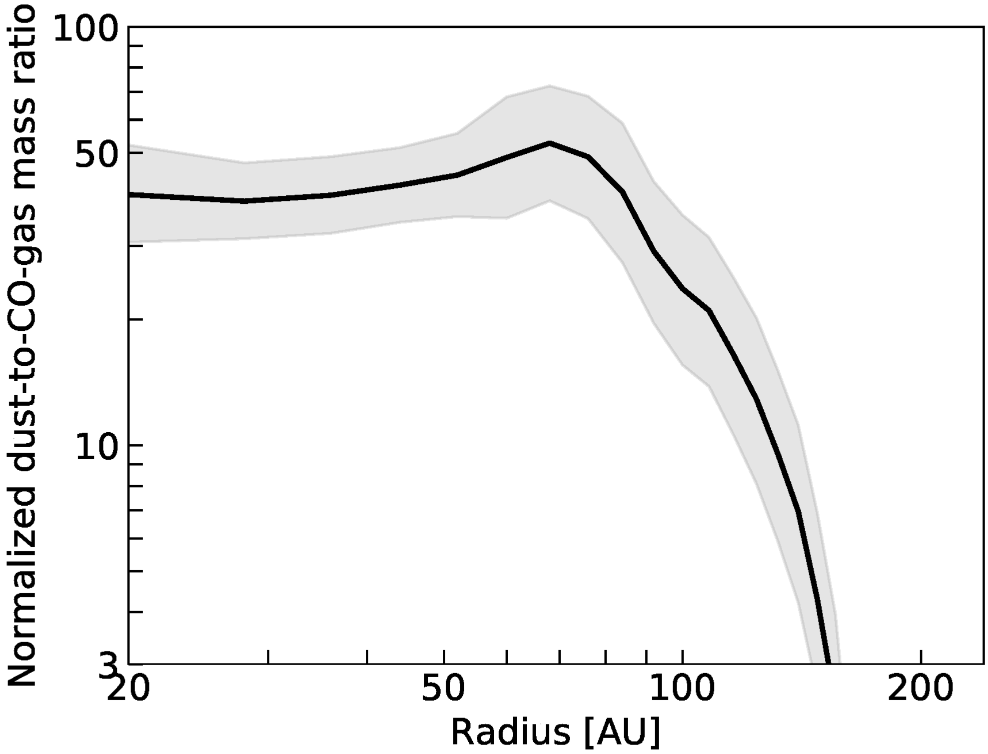

Figure 3.4. The radial profile of the dust-to-CO-gas mass ratio (ϵ/X) normalized by the typical ratio of the interstellar medium (ϵ_0/X_0). The gray-shaded region indicates the uncertainty of the ratio. The disk region in $r \lesssim 80$ au has ~ 50 times higher dust-to-CO-gas mass ratio than the typical interstellar medium. The $\Sigma_{\rm dust}$ profile is convolved with the same beam size of the $C^{18}O$ line image for deriving the dust-to-CO-gas mass ratio.

tainty of the normalized dust-to-CO-gas mass ratio based on the uncertainties of the derived $\Sigma_{\rm dust}$ and $N_{\rm C^{18}O}$ radial profiles. I note that the $\Sigma_{\rm dust}$ profile is convolved with the same beam size of the C^{18}O line image for deriving the dust-to-CO-gas mass ratio. The dust-to-CO-gas mass ratio in the disk radius of $r \lesssim 80$ au is ~ 50 times higher than the typical ISM value.

The dust concentration by the radial drift of dust grains is one of the possible mechanisms to explain this high dust-to-CO-gas mass ratio of the inner disk. If I simply assume that the initial dust disk is extended to $r = 240$ au with a uniform dust surface density and the dust mass in the disk is conserved during the radial contraction, the initial dust surface density of the disk is $\Sigma_{\rm dust,ini} \sim 0.0189$ g cm^{-2}. This is corresponding to the value at $r \sim 90$ au. If only dust grains drift inward down to $r \sim 90$ au from $r = 240$ au, ~ 9 times dust concentration is acceptable. However, it is still not enough to reach ~ 50 times higher dust-to-CO-gas mass ratio. Therefore, it may need other processes to increase the dust-to-CO-gas mass ratio in the inner disk. The CO gas depletion ($X = N_{\rm CO}/N_{\rm H_2} < 10^{-4}$) and/or gas dispersal ($\epsilon = \Sigma_{\rm dust}/\Sigma_{\rm gas} > 0.01$) may have to be considered as another possibility to explain this high dust-to-CO-gas mass ratio. I note that there are some uncertainties in the derived dust-to-CO-gas mass ratio. As mentioned in Section 3.1, the $\Sigma_{\rm dust}$ profile could be underestimated because the temperature at the disk midplane is possibly lower than the temperature of the ^{13}CO line emitting region where may be above the disk midplane. In that case, the dust-to-CO-gas mass ratio could be underestimated. Meanwhile, if the C^{18}O line is optically thick, the derived $N_{\rm C^{18}O}$ will be underestimated. Thus, the derived dust-to-CO-gas mass ratio could be overestimated.

Even if I can reproduce the observed high dust-to-CO-gas mass ratio considering dust concentration, gas dispersal, or CO depletion, this high dust-to-CO-gas mass ratio can trigger the gravitational or streaming instabilities. The disk stability by the self-gravity is represented by the Toomre's Q parameter (Toomre 1964),

$$Q \equiv \frac{c_{\rm s}\Omega_{\rm K}}{\pi G \Sigma_{\rm disk}}, \tag{3.6}$$

where $c_{\rm s}$ is sound speed, $\Omega_{\rm K}$ is orbital frequency, G is the gravitational constant, and $\Sigma_{\rm disk}$ is disk surface density. I adopt the assumption of $T = T_{\rm B,peak,^{13}CO}$ and the CR Cha stellar mass of $M_* = 1.657\ M_\odot$ (Villebrun et al. 2019) for deriving $c_{\rm s} = \sqrt{kT/\mu m_{\rm H}}$ and $\Omega_{\rm K} = \sqrt{GM_*/r^3}$ where $\mu = 2.34$ is the mean molecular weight of the disk materials. If the derived high dust-to-CO-gas mass ratio in the inner disk is explained only by the CO gas depletion and there is no gas dispersal and no dust concentration, that is, $\Sigma_{\rm disk} \approx \Sigma_{\rm gas} = 100\Sigma_{\rm dust}$, the Toomre's Q parameter is derived as $Q \sim$ 1-3 inside of $r \lesssim 100$ au, as shown in Figure 3.5, indicating that the disk is marginally unstable by the self-gravity. Meanwhile, if there is gas dispersal and/or dust concentration, Figure 9 in Yang et al. (2017) shows that $\Sigma_{\rm dust}/\Sigma_{\rm gas} \gtrsim 0.2$ triggers the streaming instability regardless of the grain sizes. It may infer that $(\epsilon/X)/(\epsilon_0/X_0) \gtrsim 20$ can trigger the streaming instability if I assume no CO gas depletion, that is, $X = N_{\rm CO}/N_{\rm H_2} = 10^{-4}$. If these instabilities are triggered, the dust disk is rapidly dissipated by creating planetesimals or disk substructures like spiral arms. Then, the extended dust disk cannot stand for a long time (e.g., Dong et al. 2015a; Li et al. 2019). Since it is not consistent with the observation, some assumptions used in the derivations of dust and gas surface density from the CR Cha observations may not be realistic. I need more investigation for solving this problem in the future.

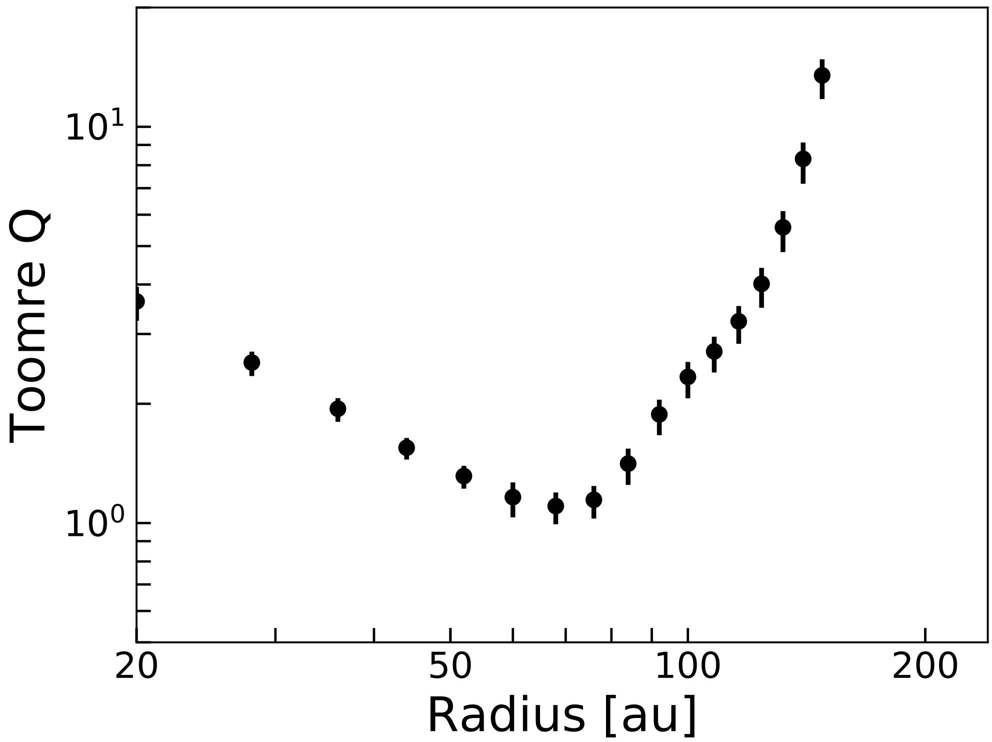

Figure 3.5. The Toomre's Q parameter of the CR Cha disk derived from the convolved $\Sigma_{\rm dust}$ radial profile with the assumption of $\Sigma_{\rm disk} \approx \Sigma_{\rm gas} = 100\Sigma_{\rm dust}$. The region inside of $r \lesssim 100$ au has $Q \approx$ 1-3, which is the marginally gravitationally unstable disk.

3.4 The formation of dust ring-gap structure

In this section, I investigate some possible origins of the observed disk substructure in the CR Cha disk: the dust ring-gap structure and the bump in the peak brightness temperature of the ^{13}CO emission line. I examine two origins suggested by the previous studies (e.g., Ribas et al. 2017; Ubach et al. 2017) by comparing the observed dust and gas properties to the model expectations: (1) The gap opening by a planet and (2) the dust trapping at the gas pressure bump at the outer edge of the dust disk (Kim et al. 2020). I note that Dr. Sanemichi Takahashi at the National Astronomical Observatory of Japan performed the fitting of the gap structure using the planet-driven gap structure models and running the radiative transfer calculation using the HO-CHUNK code as the collaborative works for Kim et al. (2020). I also briefly describe the other possible origins of the disk substructures in the CR Cha disk in the last part of this section.

3.4.1 Gap opening by a planet

Many previous numerical simulations have studied the relation between the surface density distribution of the dust and gas disk around the gap structure and the planet mass. In this subsection, I compare the $\Sigma_{\rm dust}$ profile around the gap structure of the CR Cha disk obtained from new high-resolution observation to the numerical models to constrain the planet mass which can reproduce the observed gap structure (Kim et al. 2020).

First, I check the minimum planet mass $M_{\rm p,min}$ for creating the observed dust gap structure of the CR Cha disk. Rosotti et al. (2016) suggested that the $M_{\rm p,min}$ that can perturb the dust surface density as

$$M_{\rm p,min} \sim 15\ M_{\oplus} \left(\frac{H/R}{0.05}\right)^3 \left(\frac{M_*}{1\ M_{\odot}}\right) \tag{3.7}$$

where $M_\oplus$ is the Earth mass, H is the disk scale height, R is the orbital radius of the planet, and M_* is the central stellar mass. To evaluate H/R, I use $T = 22$ K at the gap center of $r_{\rm cent} = R = 91.47$ au, which is obtained from the derived $T_{\rm B,peak,^{13}CO}$ profile and the derived $\Sigma_{\rm dust}$ distribution in Section 2.4 and 3.1. By inserting $M_* = 1.657\ M_\odot$ (Villebrun et al. 2019) and $H/R = 0.0683$ into Equation 3.7, I obtain the $M_{\rm p,min}$ for opening the observed dust gap in the CR Cha disk as $M_{\rm p,min} \sim 0.2\ M_{\rm J}$ where $M_{\rm J}$ is the Jupiter mass.

To estimate the planet mass which opens the observed gap in the CR Cha, I adopt the empirical relation expressed by Equation 6-10 in Kanagawa et al. (2017). Kanagawa et al. (2017) introduced two parameters, K and K', which control the surface density profile:

$$K = \left(\frac{M_{\rm p}}{M_*}\right)^2 \left(\frac{h_{\rm p}}{R_{\rm p}}\right)^{-5} \alpha^{-1} \tag{3.8}$$

and

$$K' = K \left(\frac{h_{\rm p}}{R_{\rm p}}\right)^2 \tag{3.9}$$

where $M_{\rm p}$ is the planet mass, $h_{\rm p}$ is the disk scale height at the planet orbital radius $R_{\rm p}$, and α is the dimensionless parameter for the strength of the turbulence (Shakura & Sunyaev 1973). I use the values of $T = 22$ K, $r_{\rm cent} = R_{\rm p} = 91.47$ au, and $M_* = 1.657\ M_\odot$ for evaluating the parameters in Equation 3.8 and 3.9. Then, the parameters K and K' can be reduced as a function of a single variable parameter $\alpha^{-1}(M_{\rm p}/M_*)^2$.

Figure 3.6 shows the comparison between the observed $\Sigma_{\rm dust}$ profile of the CR Cha disk with their observational uncertainties (filled squares with error bars) and the fitting of the model $\Sigma_{\rm dust}$ profile of the dust gap opened by a planet (solid line). I note that

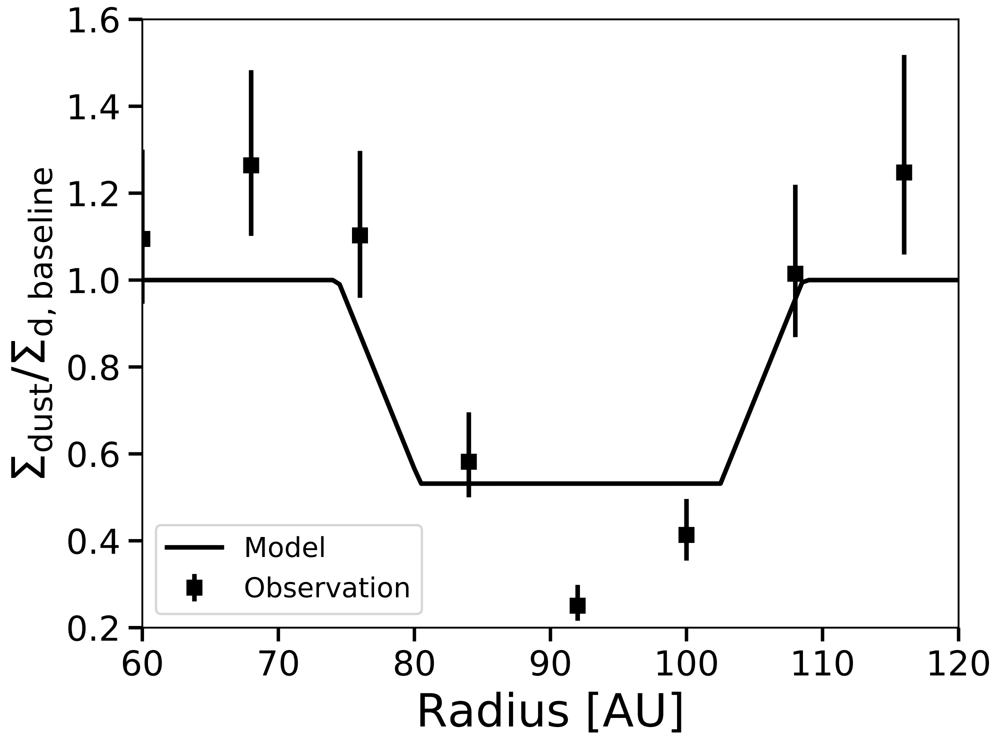

Figure 3.6. The comparison between the $\Sigma_{\rm dust}$ profiles derived from ALMA high-resolution observation (filled squares with error bars) and the model $\Sigma_{\rm dust}$ profile of the gap opened by a planet (solid line). The vertical axis is the $\Sigma_{\rm dust}$ profile normalized by the baseline function expressed in Equation 3.1.

I use the normalize $\Sigma_{\rm dust}$ profile by the baseline function expressed in Equation 3.1 for the fitting of the model $\Sigma_{\rm dust}$. I obtain the best model fit value of $\alpha^{-1}(M_{\rm p}/M_*)^2 = (3.3{\pm}1.1){\times}10^{-5}$. Therefore, the planet mass which can open the observed gap structure in the CR Cha disk is

$$M_{\rm p} = (0.99 \pm 0.15) M_{\rm J} \left(\frac{\alpha}{0.01} \right)^{0.5}. \tag{3.10}$$

However, the planet mass estimated here still has a large uncertainty. First, the observed gap structure is not resolved enough because of the comparable synthesized beam size to the total gap width as mentioned in Section 3.1. The real dust gap depth in the CR Cha disk could be deeper than the derived dust gap depth from this observation. Second, the depth of the dust gap may be much deeper than that of the gas gap. I assume that the dust gap structure detected by the observation can trace the gas gap structure in the disk. This assumption will be justified when the dust grains are small enough to be tightly coupled with the disk gas. In contrast, dust particles will be evacuated from the gas gap if the dust particles grow to mm-sized grains that are significantly affected by the gas drag (e.g., de Juan Ovelar et al. 2013; Dong et al. 2015b). In this case, I obtain the depth of the gas gap deeper than the real, which concludes a more massive planet mass is required to reproduce the gap depth derived from the observation. The scattered light imaging in the IR regime will be a good next step to investigate the estimation of planet mass and gap structures with their higher spatial resolutions and direct tracing of small dust grains that are generally well-coupled with the gas (e.g., Dong & Fung 2017).

Finally, I estimate the upper limit of the planet mass by assuming the non-detection of the gas gap when the gas gap is too shallow or too wide to be detected within the observational uncertainties. The ratio of the derived lower and upper limit of $N_{\rm C^{18}O}$ at

100 au is ~ 0.6. If I assume that the upper limit of $N_{\mathrm{C^{18}O}}$ is the baseline value and the lower limit of $N_{\mathrm{C^{18}O}}$ is the bottom of the gas gap, I can write the equation for the parameter K as

$$\frac{\Sigma_{\mathrm{lower}}}{\Sigma_{\mathrm{upper}}} = \frac{1}{1+0.04K} > 0.6. \tag{3.11}$$

When I insert the values of $R_{\mathrm{p}} = 91.47$ au, $T = 22$ K, and $M_{*} = 1.657\ M_{\odot}$ into Equation 3.11, the upper limit of the planet mass is derived as

$$M_{\mathrm{p}} < 0.87 M_{\mathrm{J}} \left(\frac{\alpha}{0.01}\right)^{0.5}. \tag{3.12}$$

Similarly, if the gas gap has a comparable width to the synthesized beam size of the ALMA observation, I also cannot detect the gas gap in the $N_{\mathrm{C^{18}O}}$ profile. The relation between the gap width and the planet mass is expressed as

$$\Delta R = 0.33 K'^{0.25} R_{\mathrm{p}}. \tag{3.13}$$

Considering the beam size of $\sim 0''.2$ corresponding to ~ 37.6 au in the physical scale at the distance of $d \sim 187.5$ pc, the upper limit of the planet mass is derived as

$$M_{\mathrm{p}} < 1.2 M_{\mathrm{J}} \left(\frac{\alpha}{0.01}\right)^{0.5}. \tag{3.14}$$

Combining all those values, I conclude that a Jupiter-mass planet is required to reproduce the observed dust gap structure in the CR Cha disk regardless of the existence of the gas gap at the dust gap location.

The temperature bump around 130 au could be related to the radiative heating on the outer wall of the gap. According to the previous studies, the gap opening by a planet makes a variation of the temperature distribution around the gap structure (e.g., Jang-Condell & Turner 2012; Turner et al. 2012). Due to the low optical depth inside the gap structure, stellar radiations can easily reach to the outer wall of the dust gap of the disk. Then, the radiations act like a heating source on the outer wall of the gap structure. This process can make a temperature bump at the outer edge of the dust gap structure like the observed temperature bump in the ^{13}CO emission line.

3.4.2 Dust trapping at the gas pressure bump

In this subsection, I discuss another possible origin of the dust ring-gap structure in the CR Cha disk. The dust trapping mechanism at the gas pressure bump is the formation mechanism of the dust ring structure (Kim et al. 2020). I assume the situation that the dust disk becomes more compact than the gas disk through the radial drift of the dust grains. Initially, the observed dust ring structure next to the dust gap does not exist. At the outer edge of the compact dust disk, the optical depth rapidly decreases by the steep negative gradient of the dust surface density profile. Then, the temperature at the disk midplane increases by the direct irradiations from the central star and the hot surface layer of the disk. This temperature increment leads to the formation of the gas pressure bump just beyond the edge of the compact dust disk. If there is enough amount of dust grains in the outside of the compact dust disk, they drift inward and concentrate at the gas pressure bump forming the dust ring structure. This mechanism is consistent with the observed features of the CR Cha disk: the dust ring beyond the dust gap, a more compact dust disk than the gas disk, and the temperature bump in the ^{13}CO line emission beyond the dust gap.

The dust trapping mechanism is based on the increment of gas temperature at the outer edge of the compact dense dust disk. Therefore, I calculate the gas temperature distribution in the disk r-z plane of the CR Cha disk through the radiative transfer calculation by adopting the observed $\Sigma_{\rm dust}$ and $N_{\rm C^{18}O}$ profiles in Figure 3.7. I note that Dr. Sanemichi Takahashi at the National Astronomical Observatory of Japan runs a published radiative transfer calculation code HO-CHUNK (Whitney et al. 2003a,b, 2004, 2013) to calculate the gas temperature distribution as the collaborative work for Kim et al. (2020) and I adopt the results for my Ph.D. thesis.

For taking into account the effect of the stellar radiation to the disk, I adopt the stellar mass of $M_* = 1.657\ M_\odot$, the effective temperature of $T_{\rm eff} = 4800$ K, and the stellar radius of $R_* = 3.113\ R_\odot$ (Villebrun et al. 2019). I also adopt the $\Sigma_{\rm dust}$ profile derived from the observation with $T_{\rm dust} = T_{\rm B,peak,^{13}CO}$ to take into account the compact dense dust disk for the radiative transfer calculation. Following the assumption of the initial dust disk without the dust ring structure, I make the least squares fitting to the observed $\Sigma_{\rm dust}$ profile within the radius ranges of 20 $\rm au \leq r \leq 100$ au. I obtain the fitting results of the $\Sigma_{\rm dust}$ profile as

$$\Sigma_{\rm d,RT} = A\left(\frac{r}{10\ \rm au}\right)^B \exp\left[-\left(\frac{r}{C\ \rm au}\right)^{10}\right] \tag{3.15}$$

where $A = 0.27 \pm 0.02\ \rm g\,cm^{-2}$, $B = -0.45 \pm 0.06$, and $C = 86.0 \pm 1.66$ au. The black dashed line in Figure 3.7 presents the $\Sigma_{\rm d,RT}$ profile of the compact dust disk without the outer ring structure. Although the dust temperature will change step by step during the radial drift of the grains in reality, here I assume a fixed dust surface density profile for the simplicity.

The radiative transfer calculation code introduces two dust populations, small dust grains and large dust grains. The size range of small grains is from 0.0025 μm to 0.2 μm and the size range of large grains is from 0.01 μm to 1 mm. The size distribution

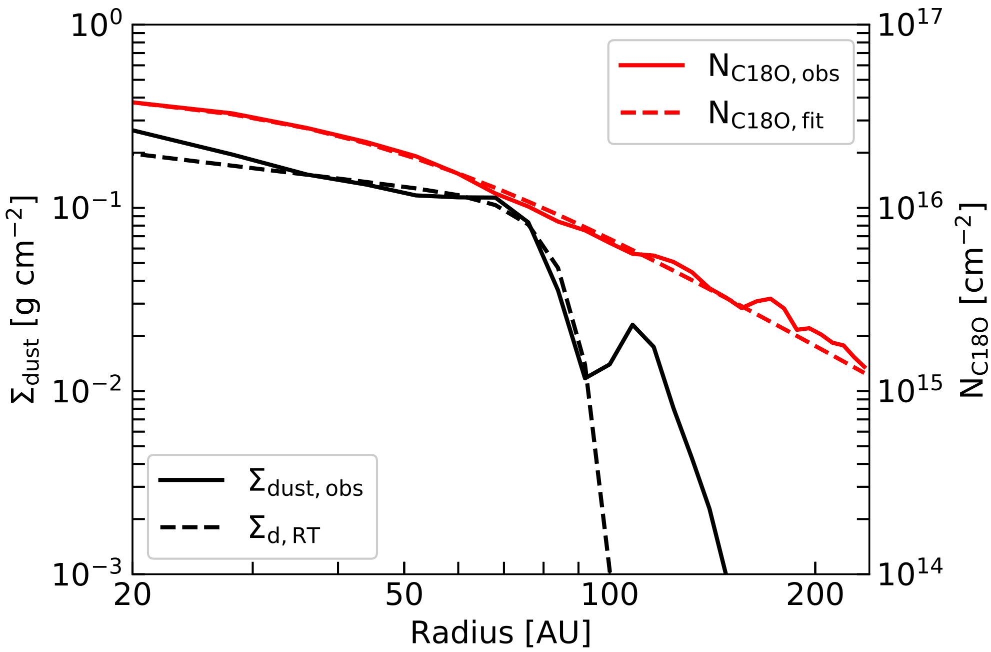

Figure 3.7. The $\Sigma_{\rm dust}$ profile (black) and the $N_{C^{18}O}$ profile (red) derived from the ALMA high-resolution observation (solid) and the fitting results (dashed) of Equation 3.15 and 3.18 for the radiative transfer calculation. The fitted $\Sigma_{\rm d,RT}$ profile excludes the outer dust ring structure following the assumption of the initial dust disk.

of both dust populations is $n(a) \propto a^{-3.5}$, where $n(a)$ is the number density per unit radius and a is the radius of dust grains. The opacity models for the small and large dust grains are described in Hashimoto et al. (2015) (Figure 3.10; see also Kim et al. 1994; Wood et al. 2002; Dong et al. 2012). I adopt the $\Sigma_{\rm d,RT}$ profile expressed by Equation 3.15 as the surface density distribution of the large dust grains ($\Sigma_{\rm large}$). And I assume that the surface density of the small dust grains ($\Sigma_{\rm small}$) is 10 times smaller than that of the large dust grains ($\Sigma_{\rm small} = 0.1\ \Sigma_{\rm large}$; e.g., D'Alessio et al. 2006). I note that the small-to-large dust mass ratio for the size distribution of $n(a) \propto a^{-3.5}$ is 1%, not 10%. However, many practical calculations (e.g., Andrews et al. 2011; Dong et al. 2015b) adjust the small-to-large dust mass ratio from 1% independently using the same size distribution of dust grains because the results of the 1% ratio and 10% ratio are largely the same.

To obtain the volume density distributions of the small and large dust grains, I set the scale height of them as

$$H_{\rm large} = 2\ {\rm au} \left(\frac{r}{100\ {\rm au}}\right)^{1.25} \tag{3.16}$$

and

$$H_{\rm small} = 6.5\ {\rm au} \left(\frac{\rm r}{100\ {\rm au}}\right)^{1.25} \tag{3.17}$$

where $H_{\rm large}$ and $H_{\rm small}$ are the scale heights of the large and small dust grains, respectively. I assume that the $H_{\rm small}$ is similar to the gas scale height ($H_{\rm gas}$) based on the assumption that the small dust grains are coupled with the gas. The $H_{\rm large}$ is assumed to be about three times smaller than $H_{\rm small}$. At $r = 70$ au, the gas surface density is $\Sigma_{\rm gas} = 10$ g cm^{-2} if I assume the turbulence strength is $\alpha = 10^{-2}$ and

$\Sigma_{\rm gas} = 100\Sigma_{\rm dust}$. Then, the scale height of 1 mm dust grains, which is the maximum size of the large dust grains, is about three times smaller than the gas scale height. In reality, although the ratio between the scale heights of dust grains and gas will depend on the radius, I assume the constant ratio for the simplicity of the calculation. Using these scale heights, I derive the volume density of the small and large dust grains that are proportional to $\exp(-z^2/2H^2)$ in the disk z-direction.

Figure 3.8 presents the temperature distribution of the small dust grains in the disk r-z plane calculated by the radiative transfer calculation by adopting the $\Sigma_{\rm d,RT}$ profile and the dust grain models described in the previous two paragraphs. The color bar in the right presents the color indications from 10 K to 300 K. There is a temperature bump in the region of $r \gtrsim 100$ au that would make a gas pressure bump and then the dust ring structure by the trapping of dust grains.

Since the large dust grains tend to settle down to the disk midplane, I also need to investigate the temperature bump at the midplane. Figure 3.9 presents the temperature distribution of the small and large dust grains at the disk midplane calculated by the radiative transfer calculations. The solid line indicates the temperature radial profile of the small dust grains ($T_{\rm small}$) and the dashed line indicates the temperature radial profile of the large dust grains ($T_{\rm large}$). The $T_{\rm small}$ profile starts to increases at the outer edge of the dust gap at $r \sim 90$ au. In contrast, the $\rm T_{large}$ profile does not increase much in the same region of the disk. The temperature at the disk midplane is determined by the balance between the heating by the radiations from the hot surface layer where is irradiated by the stellar radiation and the radiative cooling of the dust grains by their dust thermal emission. In the region of $r \lesssim 90$ au, the disk is very dense so that the $T_{\rm small} \approx T_{\rm large}$ by the collisional thermalization. Also, the disk is optically thick against the irradiation from the hot surface layer so that they keep low temperatures

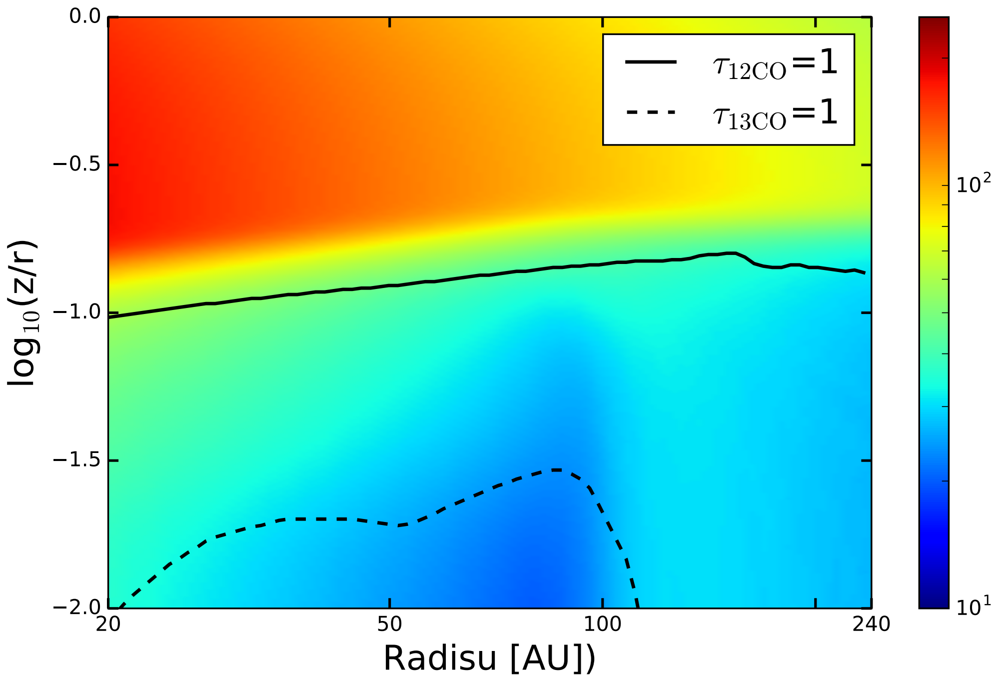

Figure 3.8. The gas temperature distribution in the disk r-z plane calculated by the radiative transfer calculation. The solid and dashed lines indicate the photospheres ($\tau_\nu = 1$) of the ^{12}CO and ^{13}CO emission lines derived from the observed $N_{\mathrm{C^{18}O,model}}$ profile, respectively. The disk region outside of $r \sim 100$ au has a relatively higher temperature than the inner disk. This temperature bump could make the gas pressure bump for making the observed dust ring structure.

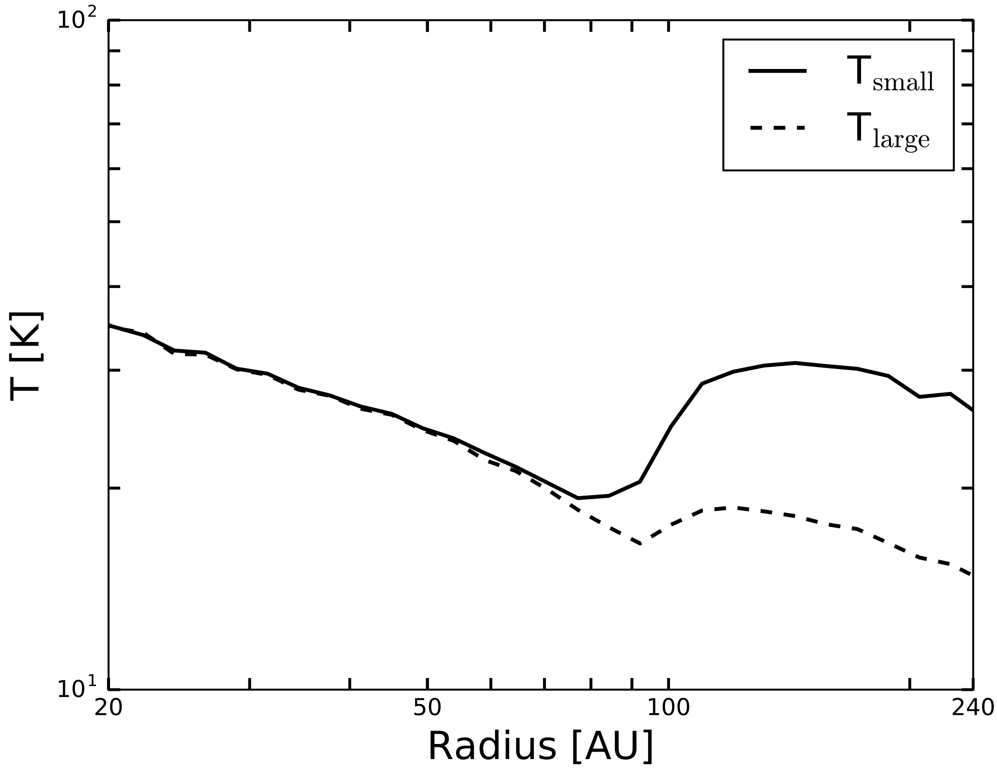

Figure 3.9. The temperature distribution of the small (T_{small}, solid) and large (T_{large}, dashed) dust grains at the disk midplane. The T_{small} distribution shows a bump beyond the dust gap at $r \sim 90$ au. Meanwhile, the T_{large} distribution does not have a bump structure at the same region.

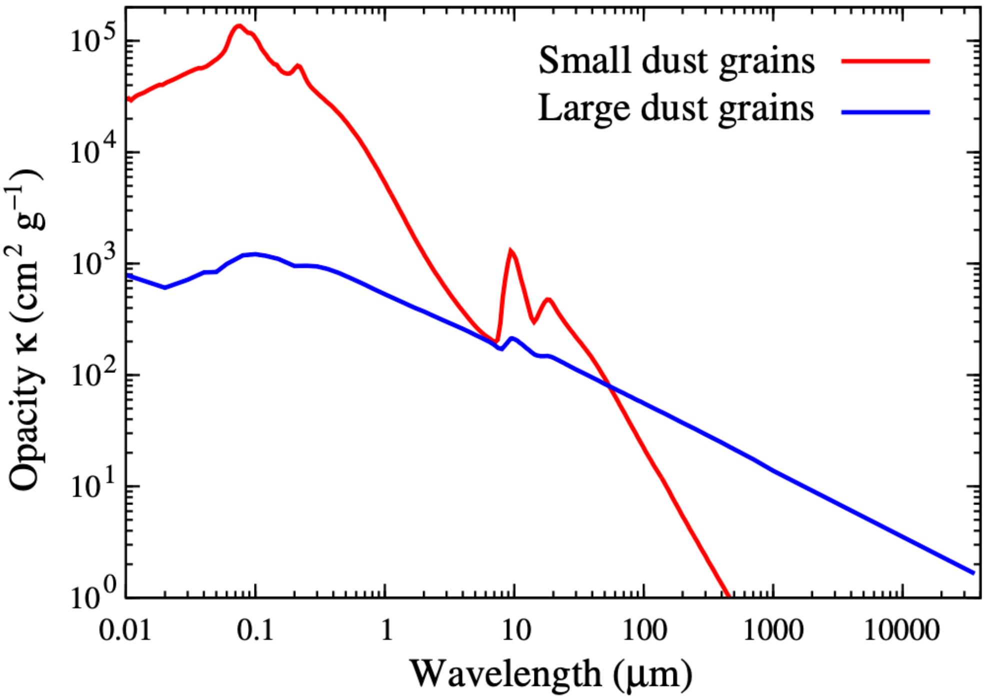

Figure 3.10. The dust opacity models of the small (red) and large (blue) dust grains for the radiative transfer calculation (Figure 5 of Hashimoto et al. 2015). The opacity profiles cross each other around $\lambda \sim 70$ μm. The opacity of small dust grains is higher than that of large dust grains for the radiation from the hot surface disk layer peaked around $\lambda \sim 30$ μm. Similarly, the opacity of small dust grains is smaller than that of large dust grains for the thermal emission of dust grains peaked around $\lambda \sim 100$ μm.

by the shielding effect. On the other hand, the dust grains at the disk midplane in the region of $r \gtrsim 90$ au are directly irradiated by the radiations from the central star and the hot disk surface since the disk becomes optically thin with the very low $\Sigma_{\rm dust}$ values. Therefore, the dust grains in this region are heated and have a higher temperature than the inner disk.

However, the difference between the $T_{\rm small}$ and $T_{\rm large}$ in this region is caused by the opacity effects of the dust grains. Figure 3.10 presents the dust opacity models of the small (red) and large (blue) dust grains used for the radiative transfer calculation (Figure 5 in Hashimoto et al. 2015). There is a cross between the dust opacities of the small dust grains ($\kappa_{\rm small}$) and large dust grains ($\kappa_{\rm large}$) around $\lambda \sim 70$ μm. Therefore, the $\kappa_{\rm small} > \kappa_{\rm large}$ for the radiations around $\lambda \sim 30$ μm, which is the peak of the irradiations from the hot disk surface, while $\kappa_{\rm small} < \kappa_{\rm large}$ for the radiations around $\lambda \sim 100$ μm, which is the peak of the thermal emissions of the dust grains at the disk midplane. It indicates that the small dust grains efficiently absorb the radiation from the hot surface layer and let the thermal radiation of grains from the midplane freely pass through. By those effects, the $T_{\rm small}$ is higher than $T_{\rm large}$ at the disk midplane making the temperature bump outside of the dense dust disk in the $r \gtrsim 90$ au region.

Since I assume that the small dust grains are tightly coupled with the gas component in the disk, I can use the $T_{\rm small}$ distribution calculated by the radiative transfer calculation as a proxy of the $T_{\rm gas}$ distribution because the $T_{\rm gas}$ will be determined by the collisional thermalization with the small dust grains. Then, I conclude that the gas temperature bump is created around $r \sim 130$ au. It indicates that this gas temperature bump would lead to the creation of a gas pressure bump at the same location. If there are enough amount of the large dust grains for making the observed dust ring structure outside of the gas pressure bump, they can be trapped at the gas pressure bump during their radial drifts and form the observed dust ring structure.

To investigate the observed bump structure around $r \sim 130$ au only seen in the ^{13}CO emission line, I calculate the optical depth of the ^{12}CO and ^{13}CO emission lines from the observed $N_{\mathrm{C^{18}O}}$ profile presented as the red solid line in Figure 3.7. I do the lease squares fitting to the $N_{\mathrm{C^{18}O}}$ profile to obtain the model $N_{\mathrm{C^{18}O,model}}$ profile with the following equation,

$$N_{\mathrm{C^{18}O,model}} = A\left[1 + \left(\frac{r}{B}\right)^{C}\right]^{-1}, \tag{3.18}$$

where $A = (4.46 \pm 0.04) \times 10^{16}$ cm^{-2}, $B = 44.40 \pm 0.5$ au, and $C = 2.12 \pm 0.03$. The red dashed line in Figure 3.7 indicates the $N_{\mathrm{C^{18}O,model}}$ profile. By adopting the abundance ratio of $^{12}\mathrm{CO}/\mathrm{C}^{18}\mathrm{O} = 444$ and $^{12}\mathrm{CO}/^{13}\mathrm{CO} = 67$ (Qi et al. 2011), I derive the $\tau_\nu = 1$ layer (i.e., photosphere) of the ^{12}CO and ^{13}CO line emissions. The solid and dashed lines in Figure 3.8 indicates the photospheres of the ^{12}CO and ^{13}CO lines. The derived density distributions indicate that the ^{12}CO emission line is optically thick at all radii. The photosphere of the ^{12}CO line is located at the hot upper surface of the disk. In contrast, the ^{13}CO emission line is optically thick in the inner region of $r \leq 100$ au while it is optically thin outside of dense dust disk. Therefore, the photosphere of the ^{13}CO emission line is located around or below the disk midplane. I note that the gas mass of the disk can be estimated by adopting the CO-to-H$_2$ ratio of 10^{-4} from the derived $N_{\mathrm{C^{18}O}}$. By integrating the $N_{\mathrm{C^{18}O}}$ profile in the radius range of 0 au $\leq r \leq 240$ au, the gas mass in the CR Cha disk is estimated of $M_{\mathrm{H_2}} \sim 0.168\ M_\odot$.

Figure 3.11 shows the temperature distributions at the ^{12}CO (solid) and ^{13}CO (dashed) photosphere layers. I note that I plot the midplane temperature if the photosphere of the ^{13}CO line is located below the midplane. The optical depth of the ^{13}CO emission line seems lower than the unity in the region of $r \gtrsim 120$ au because Figure 3.8 shows only

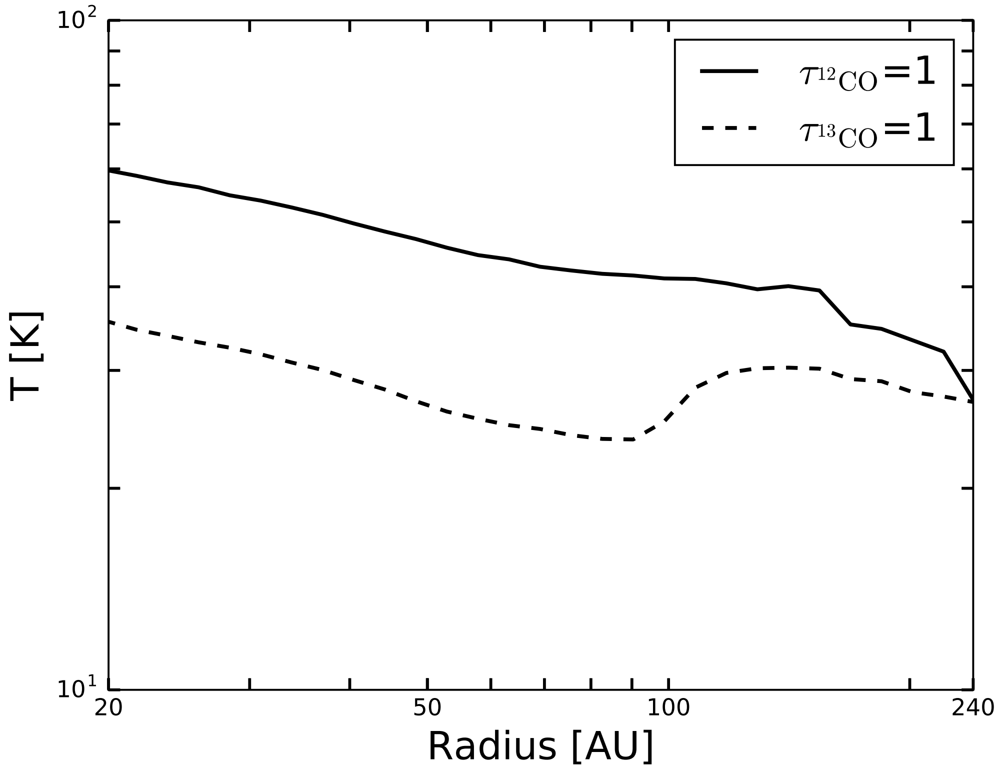

Figure 3.11. The gas temperature distribution at the photospheres of the ^{12}CO (solid) and ^{13}CO (dashed) emission lines shown in Figure 3.8. The gas temperature bump around 130 au is clearly seen at the photosphere of the ^{13}CO line since it traces the layer close to the midplane where is heated by the radiation from the hot upper disk layer. There is no bump at the photosphere of the ^{12}CO line because it traces the hot upper layer of the disk.

the upper half-disk in the z-direction. When integrating the full vertical disk, the optical depth of the ^{13}CO emission line becomes larger than unity up to $r \sim 160$ au, but ~ 0.7 in the region of $r > 160$ au. Considering the large uncertainties of the line ratios in Figure 2.10, it does not significantly conflict with the observations.

There is no bump in the temperature profile at the ^{12}CO photosphere beyond the dust gap at $r \sim 90$ au since it traces the hot upper disk surface. Meanwhile, there is a bump in the temperature profile at the ^{13}CO photosphere in the region of $r \gtrsim 90$ au. Since the optical depth of the ^{13}CO line emission is smaller than that of the ^{12}CO line, it traces the temperature at the layer closer to the midplane. This is consistent with the observed bump in the peak brightness temperature of the ^{13}CO line around $r \sim 130$ au but nothing for the ^{12}CO line. I note that the decrease of the $T_{\mathrm{B,peak,^{13}CO}}$ profile in the outer disk of $r \gtrsim 130$ au is occurred by a small $\tau_{^{13}\mathrm{CO}}$ in this region.

The dust trapping scenario looks good to explain the origin of the observed dust ring-gap structure and the gas temperature bump in the CR Cha disk. However, I need further investigation of this scenario to justify the assumptions I used for the radiative transfer calculation. For instance,

1. How can the compact disk be formed in the short time scale of $t \sim$ 1-3 Myr?
2. How the temperature distribution changes when I adopt the dust growth or time evolution of the disk?'
3. How long this temperature structure can stand being stable?
4. Does there really exist enough mass of dust grains outside of the gas pressure bump?

3.4.3 The other possible origins

I investigated two possible mechanisms to explain the observed disk substructure in the CR Cha disk in Section 3.4.1 and 3.4.2. However, there are some other possible mechanisms can reproduce the observed disk substructures in the CR Cha disk. To examine those mechanisms, I need further studies in the future.

As shown in Figure 3.9, the dust temperature at the disk midplane around the dust gap at $r \sim 91$ au is $T_{\rm d} \sim$ 20-25 K. This temperature range is comparable to the sublimation temperature of CO molecules ($T_{\rm sub} \sim$ 15-25 K). It indicates that the dust sintering effect around the CO snowline may be a possible origin of the dust gap and ring structure (Okuzumi et al. 2016). To support the sintering effect, I need to derive the size distribution of the dust grains around the ring-gap structure from the observations. For the specific, I need to derive the opacity power-law index β from the multiwavelength observations in the future. If the derived β is enhanced in the dust ring region, it will support the dust sintering effect as an origin of the dust ring-gap structure in the CR Cha.

Secular gravitational instability (secular GI; Ward 2000; Youdin 2011; Michikoshi et al. 2012; Takahashi & Inutsuka 2014) described in Section 1.2.2 is another possible formation mechanism of the dust ring-gap structure. In Section 3.3, the Toomre's $Q \sim$ 1-3 is derived from the derived $\Sigma_{\rm dust}$ and $N_{\rm C^{18}O}$ profiles. And the dust-to-CO-gas mass ratio indicates a high dust-to-gas mass ratio of $\epsilon/X \gtrsim 0.2$ if there is no CO gas depletion. These features are suitable for the growth of the secular GI in the disk (Takahashi & Inutsuka 2014, 2016; Latter & Rosca 2017; Tominaga et al. 2019). However, to examine the plausibility of this mechanism for the observed gap structure, I need the information of turbulence α in the disk to calculate the model gap depth and width. Especially, Takahashi & Inutsuka (2014) requires very weak turbulence in the disk of

$\alpha \lesssim 4 \times 10^{-4}$. If the turbulence α could be constrained from the other observational works, the secular GI is examined as the possible origin of the dust ring-gap structure in the CR Cha disk in the future.

Chapter 4

The synthetic ALMA multiband analysis on the TW Hya protoplanetary disk

In Chapter 2 and 3, I derive the dust and gas properties in the CR Cha disk from the single wavelength ALMA observation, and then investigate some possible origins of the observed small-scale substructures in the CR Cha disk. However, I used many assumptions to derive the physical properties of the disk materials, $T_{\mathrm{B,peak,^{13}CO}} = T_{\mathrm{gas}} = T_{\mathrm{dust}}$, for instance, because the single wavelength data cannot break the degeneracy in the radiative transfer equation, $I_\nu = B_\nu(T)\,[1 - \exp{(-\tau_\nu)}]$. Since those assumptions still have a large uncertainty on the derived results, I need to minimize the assumptions to derive the dust and gas properties from the observational data. To solve all the unknowns without any assumptions, the multiwavelength analysis is essential. In this chapter, I will describe the synthetic ALMA multiband analysis to find the best three ALMA band combination to derive the accurate dust properties (Kim et al. 2019).

4.1 Background and Motivation

Dust properties such as dust temperature $T_{\rm d}$, dust opacity κ_ν, and dust opacity power-law index β are the key parameters to distinguish the origins of the axisymmetric ring-gap structure. They are expected to behave in a different way around the ring-gap structures depending on the formation mechanisms (see Section 1.2). For example, the planet-disk interaction scenario makes dust filtration when the planet opens a gas gap (e.g., Zhu et al. 2012). Then, β is enhanced inside the gap because the large grains are depleted and only small-sized dust grains survive. In contrast, the dust sintering scenario (Okuzumi et al. 2016) expects the β enhancement at the dust ring region because the dust grains are piled up at the outside of the molecular snowline.

Beckwith et al. (1990) and Beckwith & Sargent (1991) were the pioneering works to constrain τ_ν and β from the single-dish observations at millimeter wavelengths of the disks surrounding the pre-main-sequence stars in Taurus-Auriga clouds. Kitamura et al. (2002) extended this approach to the interferometer observations to measure the outer radii of the disks and then estimate the dust properties. After that, some studies (e.g. Andrews & Williams 2007; Andrews et al. 2009) made further constraints on the dust properties by comparing the theoretical models with the observed visibility data. Moreover, lots of studies (e.g. Guilloteau et al. 2011; Pérez et al. 2012, 2015; Tazzari et al. 2016) have tried to derive the radial profiles of the dust properties, such as τ_ν or β, from the interferometric observations of various PPDs. Those works adopted the radial profiles of dust temperature which are mainly derived by the SED modeling or the radiative transfer calculations. If those modelings are not available, they just adopted a simple assumption of the dust temperature profile.

As a previous research, Tsukagoshi et al. (2016) derived the radial profiles of τ_ν and β from the dust continuum observations of the TW Hya disk at ALMA Band 4 and 6 by adopting the dust temperature radial profile derived from the radiative transfer calculation (Andrews et al. 2012). They made meaningful constraints on the τ_ν and β in the TW Hya disk. However, the temperature structure of the disks is significantly affected by many parameters, such as the density structure of the disk, the dust grain size distributions, then also the optical depths, and the disk substructures like a dust gap opened by a planet (e.g., Jang-Condell & Turner 2012). Therefore, more direct observations are necessary for a better understanding of the dust properties without any assumption of the dust temperature. To drop the assumption on the dust temperature structure, and then derive the improved radial profiles of dust properties in the disks, I need additional observations at a different ALMA band. Since I need at least three ALMA bands to obtain the exact solutions of ($T_{\rm d}$, τ_ν, β) through the multiwavelength analysis mathematically, I perform the synthetic ALMA multiband analysis to find which three ALMA bands are the best combination to derive the dust properties accurately by the ALMA multiband analysis. (Kim et al. 2019)

4.2 The synthetic ALMA multiband analysis

For finding the best combination of three ALMA bands providing the most accurate constraints on the dust properties, I perform the synthetic ALMA multiband analysis (Kim et al. 2019). The synthetic ALMA multiband analysis consists of two parts, setting up the model intensity at each ALMA band and performing the sensitivity analysis for extracting the constraint ranges of the synthetic dust properties corresponding to the observational uncertainty ranges. I perform the synthetic ALMA multiband analysis for all the possible 56 combinations of three ALMA bands among ALMA Band 3 to Band 10. Table 4.1 lists the representative frequency and the frequency coverage of the ALMA bands used in the synthetic ALMA multiband analysis in GHz units.

Table 4.1. The representative frequencies and frequency coverages of the ALMA bands used in the synthetic multiband analysis

Band	3	4	5	6	7	8	9	10
$\nu_{\rm min}$ (GHz)	84	125	166	211	275	385	602	787
$\nu_{\rm rep}$ (GHz)	112	145	190	233	346	450	670	870
$\nu_{\rm max}$ (GHz)	119	163	211	275	370	500	720	950

4.2.1 The model intensity at the ALMA bands

The first part of the synthetic ALMA multiband analysis is calculating the model intensity at each ALMA band by the formal solution of the radiative transfer equation,

$$I_\nu = B_\nu(T_{\rm d})[1 - \exp(-\tau_\nu)]. \tag{4.1}$$

The dust optical depth τ_ν follows the power-law function of

$$\tau_\nu = \tau_0(\nu/\nu_0)^\beta \tag{4.2}$$

by assuming that the dust opacity obeys the power-law, $\kappa_\nu \propto \nu^\beta$. I note that I simply assume that the source function is $S_\nu = B_\nu(T_{\rm d})$, and the dust temperature $T_{\rm d}$ and the absorption coefficient, $\kappa_\nu \rho_{\rm d}$ ($\rho_{\rm d}$ is the dust density), are constant along the line-of-sight in Equation 4.1 for the simplicity. In this case, the spectral index α of dust continuum emission can be written as

$$\alpha \equiv \frac{dlog(I_\nu)}{dlog(\nu)} = 3 - \frac{h\nu}{k_{\rm B}T_{\rm d}} \frac{e^{h\nu/k_{\rm B}T_{\rm d}}}{e^{h\nu/k_{\rm B}T_{\rm d}} - 1} + \beta \frac{\tau_\nu}{e^{\tau_\nu} - 1} \tag{4.3}$$

where k_B is the Boltzmann constant and h is the Planck constant.

To calculation the model intensity at each ALMA band, I derive the frequency independent radial profiles of $\tau_{0,\mathrm{model}}$ and β_model first using Equations 4.1-4.3 and the observed intensity, $I_{\mathrm{obs,190GHz}}$, and spectral index, $\alpha_{\mathrm{obs,190GHz}}$, at 190 GHz. The observational data is derived from the high-resolution (~ 88.1 mas$\times 62.1$ mas) dust continuum images at ALMA Band 4 and 6 (Tsukagoshi et al. 2016). I also adopt the assumption of $T_{\mathrm{d,model}}(r) = 26$ K $(r/10\ \mathrm{au})^{-0.4}$ for solving the equations. The $T_{\mathrm{d,model}}$(r) profile is obtained by fitting of the temperature profile at the disk midplane in the previous studies (e.g., Andrews et al. 2012, 2016), which is derived using radiative transfer calculations. Using the derived frequency independent parameters of $\tau_{0,\mathrm{model}}$ and β_model, I calculate the frequency dependent optical depth $\tau_{\nu,\mathrm{model}}$ by Equation 4.2. Then, I obtain the model intensities, $I_{\nu,\mathrm{model}}$, at a given frequency of the ALMA bands using Equation 4.1 with the $T_{\mathrm{d,model}}(r)$ and the derived $\tau_{\nu,\mathrm{model}}$ at a given radius r.

4.2.2 The sensitivity analysis

After calculating the frequency-independent $\tau_{0,\mathrm{model}}$ and β_model and the model intensities at the ALMA bands, I perform the sensitivity analysis to extract the constraint ranges of the synthetic dust parameters at a given radius; the synthetic dust temperature $T_{\mathrm{d,syn}}$, the synthetic optical depth $\tau_{\nu,\mathrm{syn}}$, and the synthetic dust opacity power-law index β_syn. To perform this sensitivity analysis, I establish the parameter space of the synthetic intensities $I_{\nu,\mathrm{syn}}$ at three ALMA bands which are arbitrarily picked among ALMA Band 3 to 10 corresponding to the combinations of [$T_{\mathrm{d,syn}}$, $\tau_{\nu,\mathrm{syn}}$, β_syn]. Then, I extract the constraint ranges of the synthetic dust properties satisfying the ranges of $(100\% - x)I_{\nu,\mathrm{model}} \leq I_{\nu,\mathrm{syn}} \leq (100\% + x)I_{\nu,\mathrm{model}}$ where $I_{\nu,\mathrm{model}}$ is the model intensities at three ALMA bands I picked using the values calculated in Section 4.2.1 and the

x indicates observational uncertainties which vary depending on the ALMA bands.

I practically obtain the constraint ranges of the synthetic dust properties in the following way. I pick three different ALMA bands $[\nu_1, \nu_2, \nu_3]$ among ALMA Band [3,4,5,6,7,8,9,10] as one band set. Then, at a given radius, I set $I_{\nu,\mathrm{syn}}$ which corresponds to the ranges of $(100\% - x)I_{\nu,\mathrm{model}} \leq I_{\nu,\mathrm{syn}} \leq (100\% + x)I_{\nu,\mathrm{model}}$ for $\nu = \nu_1$ and ν_2. The x in the equation indicates the uncertainties of the flux calibration for ALMA data: $x = 10\%$ for Band 3, 4, 5 and 6, $x = 15\%$ for Band 7 and 8, $x = 20\%$ for Band 9 and 10 (Warmels et al. 2018, p.155). Next, I derive $\tau_{\nu_1,\mathrm{syn}}$, $\tau_{\nu_2,\mathrm{syn}}$ and β_{syn} from the calculated $I_{\nu_1,\mathrm{syn}}$ and $I_{\nu_2,\mathrm{syn}}$ through Equations 4.1 and 4.2. In this step, I adopt the synthetic dust temperature in the range of $T_{\mathrm{d,syn}}$ = 5-60 K with every 0.2 K spacing. And then, I calculate $I_{\nu_3,\mathrm{syn}}$ using $T_{\mathrm{d,syn}}$, $\tau_{\nu_1,\mathrm{syn}}$, $\tau_{\nu_2,\mathrm{syn}}$, β_{syn} through Equations 4.1 and 4.2. Finally, I search the sets of $[T_{\mathrm{d,syn}}, \tau_{\nu,\mathrm{syn}}, \beta_{\mathrm{syn}}]$ satisfying the ranges of $(100\% - x)I_{\nu_3,\mathrm{model}} \leq I_{\nu_3,\mathrm{syn}} \leq (100\% + x)I_{\nu_3,\mathrm{model}}$. From the collections of the derived synthetic dust property sets, I obtain the minimum and maximum values of the synthetic dust properties. Through these calculation steps for every radius, I obtain the minimum and maximum values of $T_{\mathrm{d,syn}}$, $\tau_{\nu,\mathrm{syn}}$ and β_{syn}, which corresponds to $(100\% - x)I_{\nu,\mathrm{model}} \leq I_{\nu,\mathrm{syn}} \leq (100\% + x)I_{\nu,\mathrm{model}}$ at three frequencies $\nu = [\nu_1, \nu_2, \nu_3]$ as shown in Figure 4.2.

4.3 The result of the synthetic multiband analysis

I perform the synthetic ALMA multiband analysis described in Section 4.2 for all the possible 56 combinations of three bands among ALMA Band 3 to 10. Some ALMA band sets provide us the narrow constraint ranges of the $T_{\mathrm{d,syn}}$, $\tau_{\nu,\mathrm{syn}}$, and β_{syn}, while the others have very broad constraint ranges of the synthetic dust properties. Among the constrained synthetic dust properties, the maximum synthetic dust temperature ($T_{\mathrm{d,syn,max}}$) is the most sensitively varying parameter to the observational uncertainties within the radius ranges of 20 au $\leq r \leq$ 45 au, as shown in Figure 4.2. I calculate the normalized average deviation of $T_{\mathrm{d,syn,max}}$ from $T_{\mathrm{d,model}}$ as a representative accuracy of the synthetic ALMA multiband analysis for the quantitative comparisons between the ALMA band combinations. Figure 4.1 presents some of the normalized average deviation of $T_{\mathrm{d,syn,max}}$ from $T_{\mathrm{d,model}}$ within 20 au $\leq r \leq$ 45 au, that is,

$$\frac{1}{n_{20-45\ \mathrm{au}}} \sum_{r=20\ \mathrm{au}}^{45\ \mathrm{au}} \frac{T_{\mathrm{d,syn,max}}(r) - T_{\mathrm{d,model}}(r)}{T_{\mathrm{d,model}}(r)} \tag{4.4}$$

where $n_{20-45\ \mathrm{au}}$ is the number of grids in 20 au $\leq r \leq$ 45 au. I use a 1 au grid spacing for the radial profile of the dust properties so that $n_{20-45\ \mathrm{au}} = 26$. The left-bottom triangle in Figure 4.1 presents the normalized average deviation of $T_{\mathrm{d,syn,max}}$ of the Band [10,x1,y1] sets where x1=[9,8,7,6,5,4] and y1=[8,7,6,5,4,3]. The right-top triangle in Figure 4.1 presents those of the Band [x2, y2, 3] sets, where x2=[10,9,8,7,6,5] and y2=[9,8,7,6,5,4]. In Figure 4.1, the Band [10,6,3] set gives us the smallest $\sim 21\%$ deviation of $T_{\mathrm{d,syn,max}}$ from $T_{\mathrm{d,model}}$ on average within 20 au $\leq r \leq$ 45 au. It is also the best band set among all the possible 56 band sets.

Figure 4.2 presents the constraint ranges of the synthetic dust properties of four good ALMA band sets (the Band [10,7,3] set, [10,6,3] set, [9,7,3] set, and [9,6,3] set) and one bad ALMA band set (the Band [7,6,3] set) as the examples selected from Figure 4.1. The constraint ranges of the synthetic dust temperature $T_{\mathrm{d,syn}}$ (top), the synthetic dust optical depth at Band 3 $\tau_{\mathrm{B3,syn}}$ (middle), and the synthetic dust opacity power-law index β_{syn} (bottom) derived by the synthetic ALMA multiband analysis are presented by the different color-shaded regions; yellow for the Band [7,6,3] set, purple for the Band [9,7,3] set, blue for the Band [9,6,3] set, red for the Band [10,7,3] set, and green

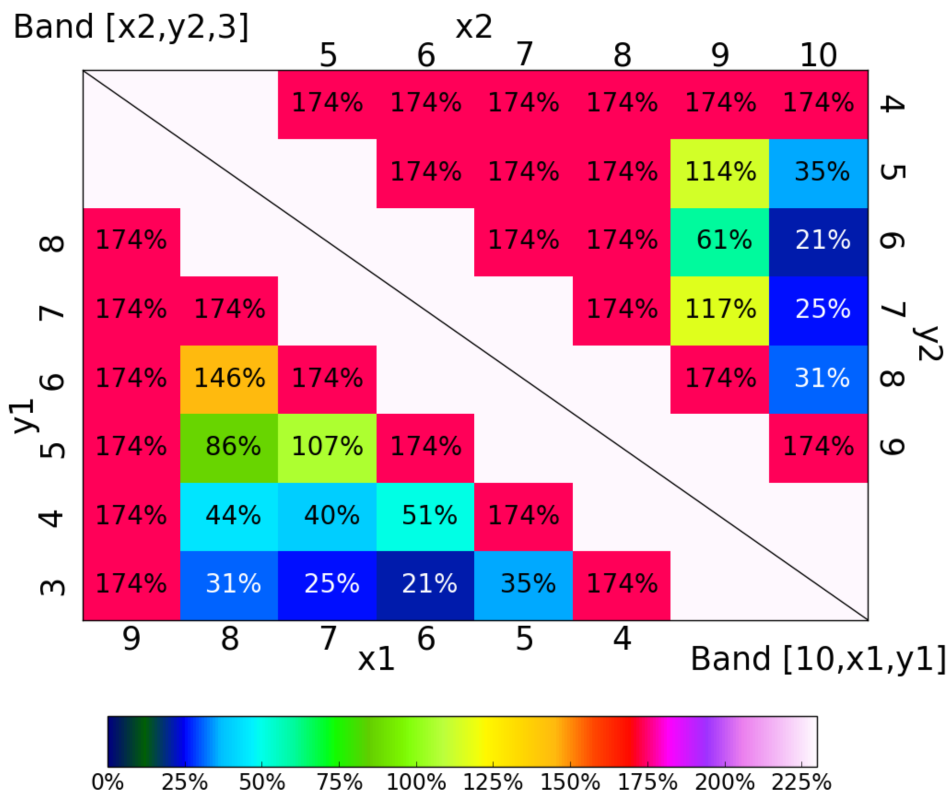

Figure 4.1. The normalized average deviation of $T_{\rm d,syn,max}$ from $T_{\rm d,model}$ within 20 au$\leq r \leq$ 45 au. The left-bottom triangle presents the normalized average deviations of $T_{\rm d,syn,max}$ for the Band [10, x1, y1] sets and the right-top triangle presents the deviations of $T_{\rm d,syn,max}$ for the Band [x2, y2, 3] sets where x1=[9,8,7,6,5,4], y1=[8,7,6,5,4,3], x2=[10,9,8,7,6,5], and y2=[9,8,7,6,5,4]. The numbers in each block indicates the normalized average deviation of $T_{\rm d,syn,max}$ from the $T_{\rm d,model}$ in percentages. The background colors of each block indicate the numbers corresponding to the bottom color bar. The smallest $\sim 21\%$ deviation of $T_{\rm d,syn,max}$ from $T_{\rm d,model}$ for the Band [10,6,3] set is the best among all the band sets.

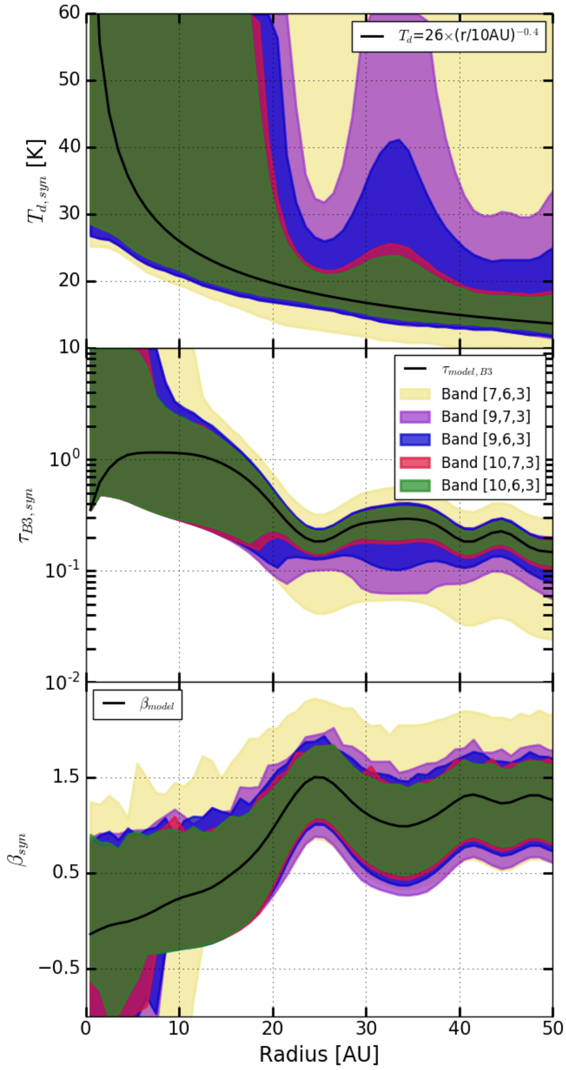

Figure 4.2. The constraint ranges of the synthetic dust temperature $T_{\rm d,syn}$ (top), the synthetic dust optical depth at ALMA Band 3 $\tau_{\rm B3,syn}$ (middle), and the synthetic dust opacity power-law index $\beta_{\rm syn}$ (bottom). They are derived by the synthetic ALMA multi-band analysis for five ALMA band sets selected from Figure 4.1. The different colors indicate the different ALMA band set; the Band [7,6,3] set by yellow, [9,7,3] set by purple, [9,6,3] set by blue, [10,7,3] set by red, and [10,6,3] set by green. The Black solid line in each panel shows the model radial profile of $T_{\rm d,model}$, $\tau_{\rm B3,model}$, and $\beta_{\rm model}$ derived by the method described in Section 4.2.1.

for the Band [10,6,3] set. The color shaded-regions are overlaid so that the green is narrower than the red area, for instance. The black solid line in each panel indicates the model radial profile of $T_{\rm d,model}(r)$, $\tau_{\rm B3,model}(r)$ and $\beta_{\rm model}(r)$ described in Section 4.2.1, respectively.

In Figures 4.1 and 4.2, the Band [10,6,3] set is the best set for constraining the accurate synthetic dust properties. Then, the better constraint ranges of the synthetic dust properties are derived from the following band sets in the order of the Band [10,7,3] set, [9,6,3] set, and [9,7,3] set. Including the other good band sets in Figure 4.1, they show two common conditions that

1. Band 9 or 10 is included in the band set

2. The bands in the set have enough large frequency intervals between them.

For the minor accuracy of the constraint ranges, if the other two bands in the sets are the same, the Band 10 gives us slightly better constraints on the dust properties than the Band 9. In Figures 4.1 and 4.2, the comparison between the band sets of [9,7,3] vs [10,7,3] and [9,6,3] vs [10,6,3] clearly show this trend for the minor accuracy in the constraint ranges. Also, the frequency intervals between the bands in the set make a small difference in the results. For instance, the Band [10,6,3] set shows slightly better constraint ranges on the synthetic dust properties than the Band [10,7,3] set and [9,6,3] set.

On the opposite side, the constraint ranges of the synthetic dust properties become very broad for the Band sets which do not satisfy two conditions. For instance, even though the observational uncertainty at Band 8 ($x = 15\%$) is smaller than that of Band 9 and 10 ($x = 20\%$), the Band sets including Band 8 instead of Band 9 or 10 (i.e. the Band [9,6,3] set vs [8,6,3] set) have broader constraint ranges of the synthetic dust properties and the $T_{\rm d,syn,max} \gtrsim 60$ K at every radius. I note that I set the range of

$T_{\mathrm{d,syn}} =$ 5-60 K for the analysis so that the maximum normalized average deviation of $T_{\mathrm{d,syn,max}}$ is fixed at 174% in Figure 4.1. Meanwhile, the cases that the two bands in the set are sequential have very bad constraint ranges of the synthetic dust properties even if Band 9 or 10 is included. For example, the Band [10,9,y1] sets where y1=[8,7,6,5,4,3] have the normalized average deviation of 174% in Figure 4.1, which means $T_{\mathrm{d,max}} \geq 60$ K at all radii.

4.4 Physical interpretations of the synthetic ALMA multiband results

In Section 4.3, I find that the Band [10,6,3] set is the best combination to obtain the most accurate dust properties by the synthetic ALMA multiband analysis and there are two common conditions for the band sets giving better constraints than the others: (1) Band 9 or 10 is included in the band set and (2) the bands in the set have enough large frequency intervals between them. Also, Band 10 gives us slightly better constraint ranges than Band 9 if the other two bands in the set are the same. In this section, I examine the effect of each dust property on the synthetic ALMA multiband analysis results by artificially changing the model parameters to understand why those conditions are necessary for the good ALMA band sets.

4.4.1 τ_ν effect

First, I analyze the τ_ν effect on the synthetic ALMA multiband analysis. I examine the behaviors of the synthetic multiband analysis results by artificially multiplying some factors to the $\tau_{0,\mathrm{model}}(\mathrm{r})$ profile derived in Section 4.2.1. Figure 4.3 illustrates the constraint ranges of $T_{\mathrm{d,syn}}$ derived from the Band [10,7,3] set with the artificially

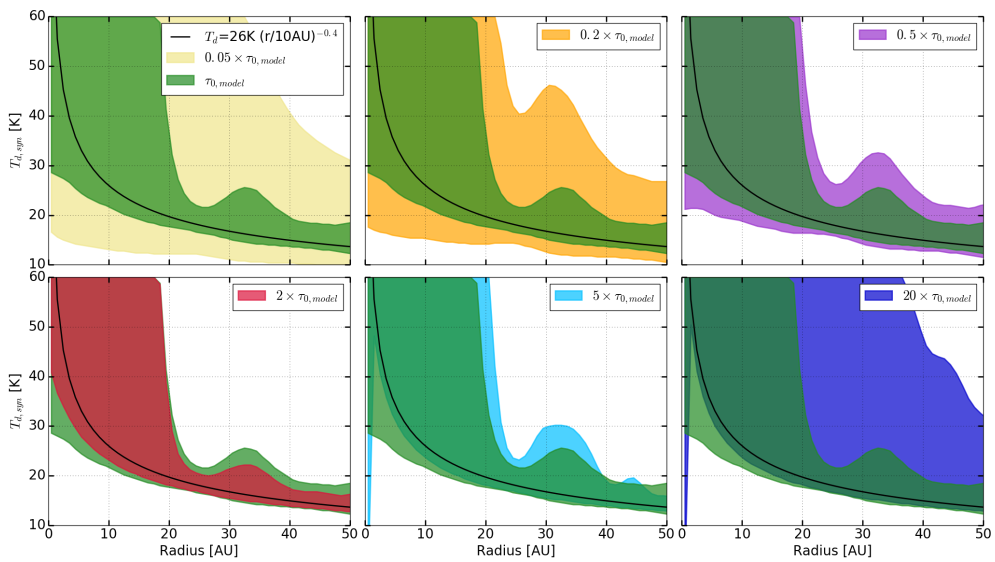

Figure 4.3. The constraint ranges of $T_{\rm d,syn}$ radial profiles derived from the Band [10,7,3] set with the different model optical depth $\tau'_{0,\rm model}$ profiles. From the Top-left panel, the results derived with $\tau'_{0,\rm model} = 0.05 \times \tau_{0,\rm model}$ (yellow), $0.2 \times \tau_{0,\rm model}$ (orange), $0.5 \times \tau_{0,\rm model}$ (purple), $2 \times \tau_{0,\rm model}$ (red), $5 \times \tau_{0,\rm model}$ (lightblue), and $20 \times \tau_{0,\rm model}$ (blue) are presented. The green shaded region in every panel indicates the derived $T_{\rm d,syn}$ constraint ranges with the original $\tau_{0,\rm model}$ for the comparison. The black solid line shows the model dust temperature profile of $T_{\rm d,model}(r) = 26\ {\rm K}(r/10\ {\rm au})^{-0.4}$.

adjusted model optical depth profiles ($\tau'_{0,\mathrm{model}}(r)$). From the top-left to the bottom-right panel, the constraint ranges of $T_{\mathrm{d,syn}}$ are presented with $\tau'_{0,\mathrm{model}}(r) = 0.05\times$, $0.2\times$, $0.5\times$, $2\times$, $5\times$, and $20\times\tau_{0,\mathrm{model}}(\mathrm{r})$. The green shaded region in every panel indicates the $T_{\mathrm{d,syn}}$ constraint range derived from the original $\tau_{0,\mathrm{model}}(r)$ as the comparison. The black solid line in every panel indicates the model dust temperature profile of $T_{\mathrm{d,model}}(r) = 26\ \mathrm{K}(r/10\ \mathrm{au})^{-0.4}$.

Figure 4.3 indicates that only the ranges of $\tau_{0,\mathrm{model}} \leq \tau'_{0,\mathrm{model}} \leq 2 \times \tau_{0,\mathrm{model}}$ provides good constraints on $T_{\mathrm{d,syn}}$ for the Band [10,7,3] set. In the optically thick ($\tau_\nu \gg 1$) and thin ($\tau_\nu \ll 1$) limits, Equation 4.1 is reduced by the approximation as

$$I_\nu \approx B_\nu(T_{\mathrm{d}}) \tag{4.5}$$

and

$$I_\nu \approx B_\nu(T_{\mathrm{d}})\tau_\nu \tag{4.6}$$

respectively. If the band set contains only optically thick bands, as in the case of $\tau'_{0,\mathrm{model}}(r) = 20 \times \tau_{0,\mathrm{model}}(r)$, I am not able to constrain the τ_ν accurately from the observed I_ν because Equation 4.5 is independent on τ_ν. On the other hand, if the band set contains only optically thin bands, as in the case of $\tau'_{0,\mathrm{model}}(r) = 0.05 \times \tau_{0,\mathrm{model}}(r)$, it is also difficult to constrain the dust properties because the dependence of the observed I_ν on T_{d} and τ_ν are completely degenerated as shown in Equation 4.6. Therefore, I can obtain better constraints on the dust properties only when the band set contains both optically thick and thin bands. The optically thick bands constrain the dust temperature accurately as indicated in Equation 4.5 and optically thin bands constrain the dust optical depth accurately by Equation 4.6 with the temperature information derived by

Equation 4.5.

4.4.2 β effect

Similarly, I analyze the β effect on the constraint ranges of the synthetic dust properties. I examine the behavior of constraint ranges with the artificially adjusted $\beta'_{\rm model}$ profiles. I derive the constraint range of $T_{\rm d,syn}$ with $\beta'_{\rm model}(r) = 1.5$ which is $\beta'_{\rm model}(r) \geq \beta_{\rm model}(r)$ at all radii where $\beta_{\rm model}(r)$ is the original model profile. Figure 4.4 illustrates the constraint range of $T_{\rm d,syn}$ derived from the Band [10,7,3] set with the $\beta'_{\rm model}(r) = 1.5$ as the red shaded region. And the constraint range derived with the original $\beta_{\rm model}(r)$ is presented as the green shaded region in the background for the comparison. The constraint range of $T_{\rm d,syn}$ becomes much better as β increases even in the inner disk, $r < 25$ au, and at the $T_{\rm d,syn}$ bump around $r \sim 33$ au.

This behavior is interpreted by the similar way described in Section 4.4.1. If β increases, the slope of the τ_ν on the frequency becomes steeper by the Equation 4.2. Then, the high-frequency bands become optically thick and the low-frequency bands become optically thin. Therefore, I can more easily obtain the combination of optically thick and thin bands satisfying the conditions for the good band sets discussed in Section 4.4.1. Meanwhile, if β is small, the optical depths at all the bands in the set are similar. That is, all the bands become optically thick or thin, and then I am not able to constrain the dust properties accurately.

4.4.3 T$_{\rm d}$ effect

In Figure 4.4, the blue shaded region presents the constraint ranges of $T_{\rm d,syn}$ with $\tau'_{0,\rm model}(r) = 1.0$ and $\beta'_{\rm model}(r) = 1.5$ at all radii, which reflects only the effect of the $T_{\rm d}$. In contrast, the red shaded region contains the dependence of the τ_ν as well.

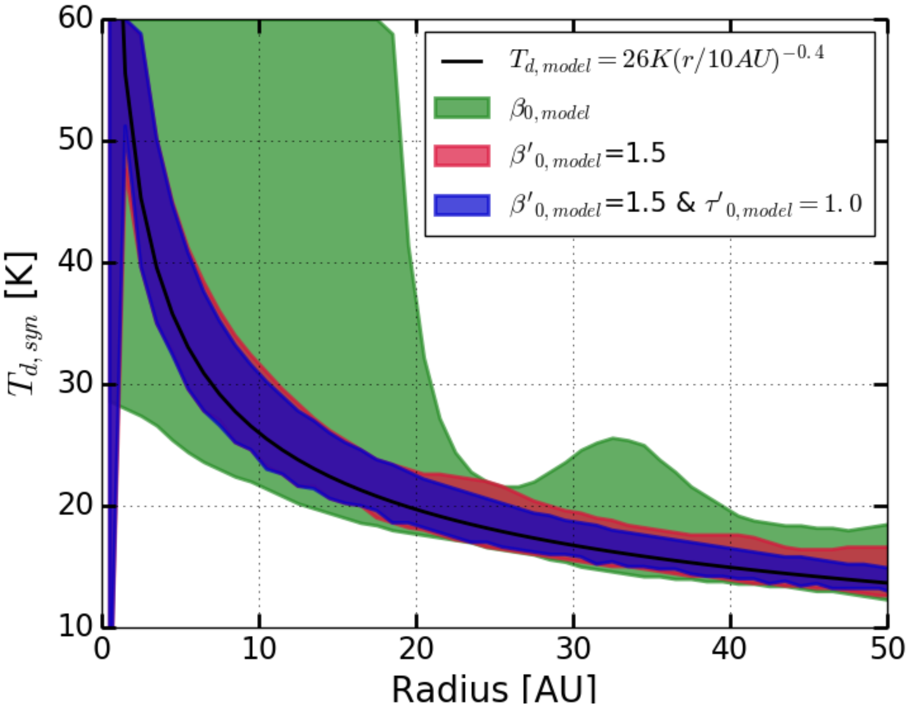

Figure 4.4. The constraint range of $T_{\mathrm{d,syn}}$ profiles derived from the Band [10,7,3] set with $\beta'_{\mathrm{model}}(r) = 1.5$ at all radii (red) and with $\beta'_{\mathrm{model}}(r) = 1.5$ and $\tau'_{0,\mathrm{model}}(r) = 1.0$ (blue). The result derived from the original β_{model} and $\tau_{0,\mathrm{model}}$ profiles is presented by the green shaded region for the comparison. These settings have $\beta'_{\mathrm{model}}(r) \geq \beta_{\mathrm{model}}(r)$ at all radii. The large β provides better $T_{\mathrm{d,syn}}$ constraint ranges than the small β. The blue shaded region shows purely T_{d} effect since I controlled two parameters, β'_{model} and $\tau'_{0,\mathrm{model}}$. The small $T_{\mathrm{d,model}}$ makes slightly better constraints than large $T_{\mathrm{d,model}}$.

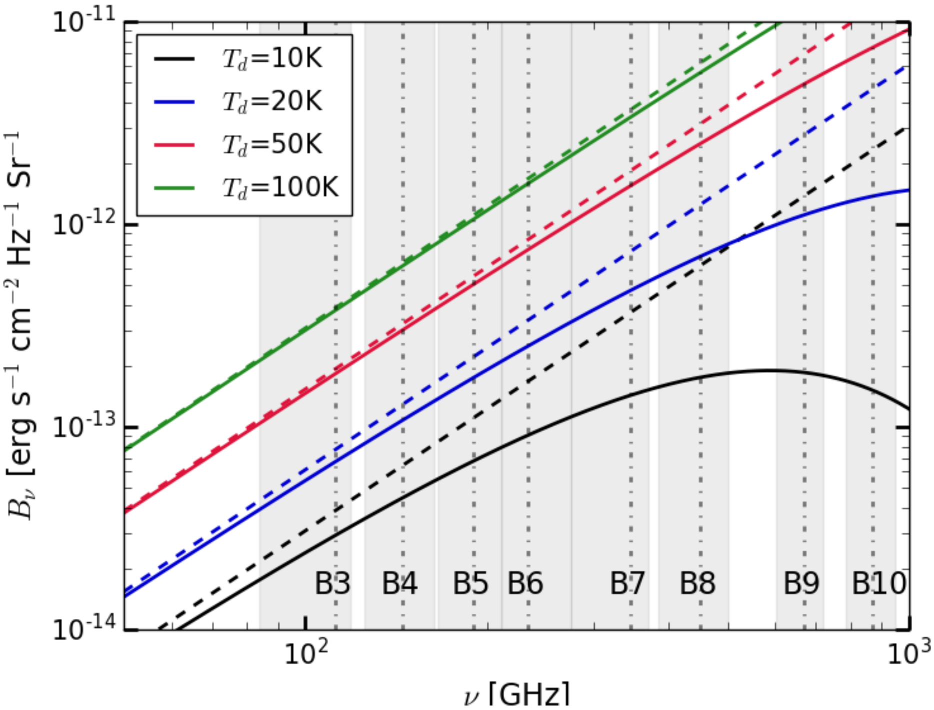

Figure 4.5. The blackbody curves at the $T_{\rm d}$ of 10 K (black), 20 K (blue), 50 K (red), and 100 K (green) in the $log(I_\nu)$-$log(\nu)$ plane. The dashed lines indicate the formula of the Rayleigh-Jeans limit which satisfies the relation $I_\nu \propto \nu^2$ at a given $T_{\rm d}$. The grey shaded regions present the frequency coverages and the dash-dotted vertical lines indicate the representative frequencies of each ALMA band listed in Table 4.1. The blackbody curves largely deviate from the Rayleigh-Jeans limit especially at high frequencies (Band 9 and 10) and the low temperatures ($T_{\rm d}$ = 10-20 K).

For example, the constraint ranges of the red region become slightly broader than the blue region around the gap at $r \sim 25$ au, where the optical depths become smaller than the unity. Focusing on the blue shaded region, the constraint ranges at $r \sim 40$ au is narrower than the ranges at $r \sim 10$ au. This result indicates that the uncertainty of the constraint ranges on the dust properties becomes larger if the dust temperature is higher.

It is explained by the deviation of blackbody curves from the Rayleigh-Jeans (RJ) limit at low dust temperatures. The solid lines in Figure 4.5 presents the blackbody curves at the $T_{\rm d} = 10$ K (black), 20 K (blue), 50 K (red), and 100 K (green), respectively. The dashed linear lines in Figure 4.5 indicate the formula of the RJ limit where $I_\nu \propto \nu^2$ at a given $T_{\rm d}$. The gray shaded regions indicate the frequency coverages and the vertical dash-dotted lines indicate the representative frequencies of each ALMA band listed in Table 4.1. For the very cold dust temperature ($T_{\rm d} \leq 20$ K), the peak of the blackbody curves locates at the frequency regimes of ALMA Band 9 or 10. Therefore, the blackbody curves largely deviate from the RJ limit at this frequency regime. If the deviation of the blackbody curves from the RJ limit becomes larger, the dust temperature can be constrained accurately because this deviation makes flexibility on the constraint of the spectral index α from the observed intensities with the observational uncertainties even at the optically thick limit. This is the reason for the first condition that the Band 9 or 10 is included in the set. Also, since the deviation from the RJ limit at the Band 10 is larger than one at the Band 9, the Band 10 data gives slightly more precise constraints of the dust properties than the Band 9 data.

4.4.4 Frequency intervals between the bands in the set

The frequency intervals between the bands in the set also affect the constraint ranges of the synthetic dust properties. Since spectral index α is defined as $\alpha \equiv \Delta log(I_\nu)/\Delta log(\nu)$, the uncertainty of α becomes smaller when the frequency intervals ($\Delta log(\nu)$) increases for a given observational uncertainties ($\Delta log(I_\nu)$). Furthermore, α is strongly related to all the dust properties as shown in Equation 4.3. Therefore, the uncertainty of α directly affects the constraint ranges of the dust properties. Owing to this effect, I need large frequency intervals between the bands in the set for the good ALMA band sets to reduce the uncertainty of α.

In principle, this interpretation indicates that I can apply the ALMA multiband analysis to the longer or shorter wavelengths data beyond the ALMA coverages to obtain the larger frequency intervals between the observational data. However, it should be cautious about the differences in the spatial resolution and the sensitivity between the data observed by different telescopes. For example, Jansky Very Large Array (JVLA) is another good instrument to obtain longer wavelength data than ALMA but the spatial resolution and the sensitivity may not be comparable to ALMA data.

4.5 Applications of the ALMA multiband analysis to the archival data of the TW Hya disk

In the previous sections, I present the synthetic ALMA multiband analysis results and two conditions for the good ALMA band sets. In this section, I examine whether the synthetic ALMA multiband analysis results are consistent with the real observational data by applying the ALMA multiband analysis to the archival dust continuum data of the TW Hya protoplanetary disk at Band 4, 6, 7, and 9. I adopt the Band 4 and 6 data of Tsukagoshi et al. (2016) and download the Band 7 dust continuum image at Sean Andrews's science homepage[1]. I also retrieve the Band 9 observation of the TW

[1]https://www.cfa.harvard.edu/ sandrews/data/twhya/

Table 4.2. The information of ALMA archival data used for the ALMA multiband analysis

Band	$\nu_{\rm rest}$ (GHz)	Beam size (mas^2)	PA (degree)	1σ level (mJy beam^{-1})
4	145	$\sim$88.1$\times$62.1	$\sim$57.8	$\sim$ 0.0124
6	233	$\sim$75.4$\times$55.2	$\sim$38.0	$\sim$ 0.0287
7	346	$\sim$24$\times$18	$\sim$78	$\sim$ 0.0350
9	661	$\sim$434$\times$247	$\sim$-85.8	$\sim$ 10

Hya disk (Schwarz et al. 2016) which is low spatial resolution data from JVO portal[2] operated by the National Astronomical Observatory of Japan. Table 4.2 summarizes the synthesized beam sizes and the 1σ noise levels of those ALMA archival data. I make two ALMA band sets for applying the ALMA multiband analysis, the Band [7,6,4] set as high-resolution data and the Band [9,6,4] set as low-resolution data.

For the consistent analysis, the images of the Band [7,6,4] set are smoothed to the beam size of $\sim 88.1 \times 62.1$ mas^2 and the images of the Band [9,6,4] set are smoothed to the beam size of $\sim 434 \times 247$ mas^2 to match the resolution of the images. I smooth the dust continuum images using the `imsmooth` command in the `CASA` package. I apply the Gaussian kernel to convolve the images, but the baseline tapering is another way to matching the spatial resolution of the images. I test the difference in the result images between the beam convolution method and the baseline tapering method using the ALMA science verification data of the HL Tau disk. The original spatial resolution of the HL Tau image is $\sim 0''.03$. I apply the beam convolution and the baseline tapering

[2]http://jvo.nao.ac.jp/portal/alma/archive.do

for making the images with the resolution of $\sim 0''.09$ and $\sim 0''.4$ where ~ 3 and ~ 13 times large beam. When the convolved resolution is ≤ 3 times larger than the original, two methods provide the same products. Meanwhile, the convolved resolution is ≥ 10 times larger than the original, the outer disk is significantly contaminated by the noises, while the inner disk has no significant contamination. Therefore, the beam convolution method is okay to use for matching the resolution of the data when the final convolved resolution is not much different from the original image. When the convolved resolution is $\sim$ 10 times larger than the original one, the baseline tapering method is better to improve the signal-to-noise ratios at the outer disk than the beam convolution method. I use the Gaussian beam convolution method because I focus on relatively inner disk ($r =$ 10-50 au) than the whole disk size ($r \sim 100$ au) even though the spatial resolution is different ~ 5.5 times between the images in the Band [7,6,4] and [9,6,4] set.

After matching the beam size of the images, I make the azimuthally-averaged de-projected intensity radial profiles. The top panel of Figure 4.6 presents the azimuthally-averaged de-projected intensity radial profiles with different colors; black for Band 4, blue for Band 6, green for Band 7, red for Band 9, and magenta for the intensity profile at 190 GHz obtained by the multi-frequency synthesis (MFS) method from the Band 4 and 6 data (Tsukagoshi et al. 2016). The solid lines indicate the radial profiles of high-resolution ($\sim 88.1 \times 62.1$ mas^2) data and the dashed lines indicate the profiles of low-resolution ($\sim 434 \times 247$ mas^2) data. The bottom panel of Figure 4.6 presents the dust brightness temperature profiles derived from the intensity radial profiles shown in the top panel of Figure 4.6 with the same color indications and line style indications.

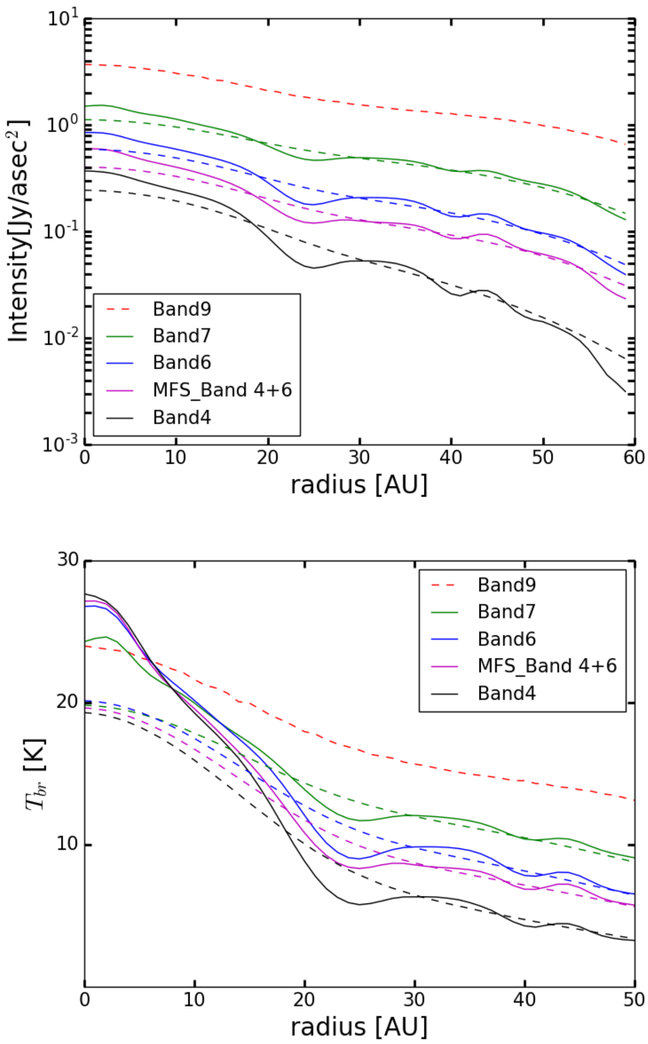

Figure 4.6. The azimuthally-averaged de-projected intensity radial profiles (top) and the brightness temperature derived from these intensity profiles (bottom). The different color indicates different ALMA band; Band 4 (black), 6 (blue), 7 (green), and 9 (red). The magenta indicates the profiles obtained by the multi-frequency synthesis (MFS) method from the Band 4 and 6 data (Tsukagoshi et al. 2016). The solid lines are the profiles of high-resolution data ($\sim 88.1 \times 62.1$ mas^2) and the dashed lines are the profiles of low-resolution data ($\sim 434 \times 247$ mas^2).

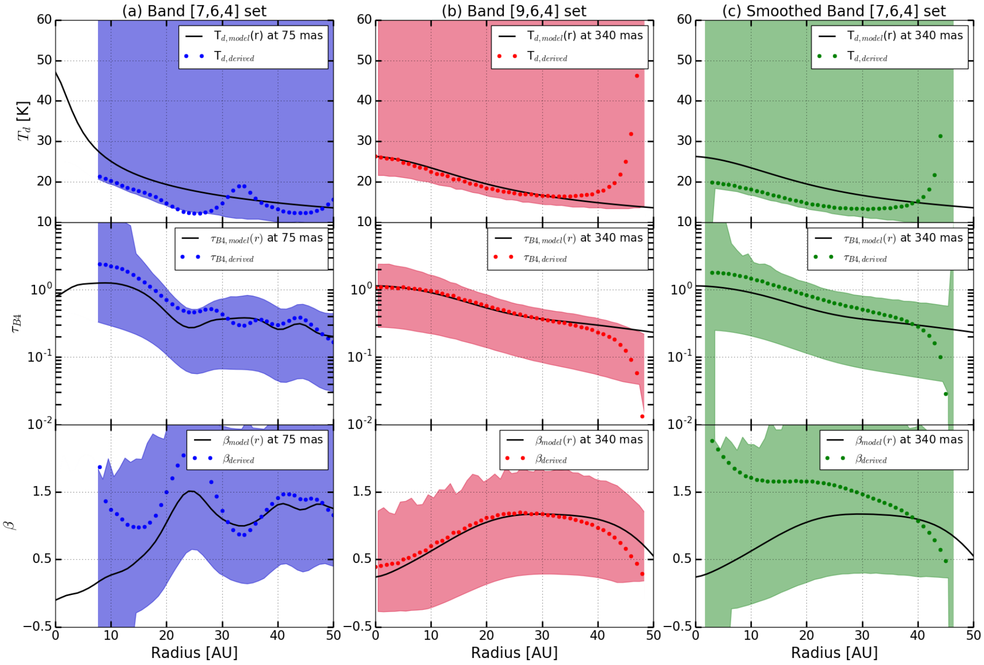

Figure 4.7. The constraints of $T_{\rm d}$ (top), $\tau_{\rm B4}$ (middle), and β (bottom) derived by the ALMA multiband analysis from the ALMA archival data. The dotted lines indicate the derived dust properties from the Band [7,6,4] set (left), the Band [9,6,4] set (center), and the smoothed Band [7,6,4] set (right). The black solid lines are the model profiles of $T_{\rm d,model}$, $\tau_{\rm B4,model}$, and $\beta_{\rm model}$ convolved by the $\sim$ 75 mas (left) and $\sim$ 340 mas (center and right) circular beam. The $T_{\rm d,model}$ profiles are smoothed from $T_{\rm d}(r) = 26\ {\rm K}\ (r/10\ {\rm au})^{-0.4}$ by the beam convolution. The model $\tau_{\rm B4,model}(r)$ and $\beta_{0,\rm model}(r)$ profiles are derived using the $T_{\rm d,model}(r)$ profile through the processes in Section 4.2.1. The color-shaded regions indicate the possible constraint ranges of the dust properties corresponding to the observational uncertainties of $\pm 10\%$ for Band 4 and 6, $\pm 15\%$ for Band 7, and $\pm 20\%$ for Band 9.

4.5.1 Application to Band [7,6,4] set

I apply the ALMA multiband analysis to the azimuthally-averaged de-projected intensity radial profiles of the Band [7,6,4] set. The dust properties are derived from the intensity at Band 7 (346 GHz) and the intensity and the spectral index α at 190 GHz obtained by the MFS method from the Band 4 and 6 data. The radial profiles of the $T_{\rm d}$, $\tau_{\rm B4}$, and β derived from the Band [7,6,4] set are shown in the left panels of Figure 4.7 as blue dotted lines. These dotted lines are used as the model profiles to derive the blue-shaded regions which indicate the possible constraint ranges of the derived dust properties corresponding to the observational uncertainties of $\pm 10\%$ for the Band 4 and 6 and $\pm 15\%$ for the Band 7. The black solid lines in the panels indicate the model profiles of the dust properties. The convolved $T_{\rm d,model}(r)$ profile is derived from the $T_{\rm d}(r) = 26$ K $(r/10$ au$)^{-0.4}$ profile by the beam convolution of ~ 75 mas circular beam, which is the mean value of $\sim 88.1 \times 62.1$ mas. The $\tau_{\rm B4,model}$(r) and $\beta_{\rm model}(r)$ profiles are derived with the convolved $T_{\rm d,model}(r)$ profile through the steps described in Section 4.2.1.

In the top panel, the dotted lines are lower than the model profile, $T_{\rm d}(r) \leq 20$ K at $r \gtrsim 10$ au, with a strange bump around $r \sim 33$ au. The temperature bump seems to appear because the uncertainty becomes large around $r \sim 33$ au due to the small β by the effect described in Section 4.4.2. The derived radial profile of the optical depth at Band 4, $\tau_{\rm B4}$, is close to the model $\tau_{\rm B4,model}$ profile, especially at $r > 35$ au, including the shallow drop at the gap locations, $r \sim 25$ au and $r \sim 41$ au. The derived $\tau_{\rm B4}$ values at $r > 20$ au are optically thin in the range of $0.1 \lesssim \tau_{\rm B4}(r) \lesssim 1$. The derived $\beta(r)$ profile is also similar to the model $\beta_{\rm model}$ profile, especially at $r > 30$ au, but the enhancement at the inner gap location ($r = 25$ au) is $\approx 40\%$ larger than the model. At $r \leq 15$ au where $\tau_{\rm B4}(r) \geq 2$, the deviation becomes very large.

In the inner disk of $r \leq 10$ au, the dust properties are not able to be constrained by the ALMA multiband analysis. In this region, the brightness temperatures derived by the intensities at Band 4 and 6 are higher than that at Band 7 as shown in the bottom panel of Figure 4.6. When the images are convolved with the beam size of $\gtrsim 0''.2$, this inversion of the brightness temperature disappears. One possible cause of this inversion is a significant phase noise of the Band 7 data. Since the phase noise makes a positional offset, the resultant image has been blurred and the peak intensity becomes smaller.

According to the interpretation of the synthetic ALMA multiband analysis, the Band [7,6,4] set is not a good band set because it does not satisfy two conditions for the good ALMA band sets. The $T_{\rm d}$, $\tau_{\rm B4}$ and β profiles derived from the Band [7,6,4] set seem to be sensitively affected by the observational uncertainties. These results are consistent with the synthetic ALMA multiband analysis results presented in Section 4.3. Also, the constraint range of $T_{\rm d}(r)$ profile derived from the Band [7,6,4] set is too broad to specify the dust temperature at all radii. Also, the constraint ranges of $\tau_{\rm B4}(r)$ and $\beta(r)$ profiles have relatively large uncertainties at all radii to discuss the small-scale variations in those properties.

4.5.2 Application to Band [9,6,4] set

I also apply the ALMA multiband analysis to the low-resolution dust continuum data set of the TW Hya disk, the Band [9,6,4] set. The dust properties are derived from the intensity at Band 9 (661 GHz) and the beam-convolved intensity and the spectral index α at 190 GHz obtained by the MFS method from the Band 4 and 6 data. I derive the radial profiles of $T_{\rm d}(r)$, $\tau_{\rm B4}(r)$, and $\beta(r)$ from those smoothed intensity radial profiles presented by the dashed lines in the top panel of Figure 4.6.

The center panels of Figure 4.7 present the derived $T_{\rm d}$, $\tau_{\rm B4}$, and β radial profiles as the red dotted lines. The format of the graphs are the same as the left panels of Figure 4.7. The $T_{\rm d,model}$ profile is derived from $T_{\rm d}(r) = 26$ K $(r/10\ \rm au)^{-0.4}$ convolved with ~ 340 mas circular beam, which is the mean value of $\sim 434 \times 247$ mas. The $\tau_{\rm B4,model}(r)$ and $\beta_{\rm model}(r)$ profiles are derived using this convolved $T_{\rm d,model}(r)$ profile through the steps described in Section 4.2.1.

As shown in the top-center panel of Figure 4.7, the derived $T_{\rm d}(r)$ profile from the Band [9,6,4] set follows the model profile well in the range of $T_{\rm d}(r) \approx$ 15-27 K in the disk region of $r \leq 40$ au. Similarly, the derived $\tau_{\rm B4}(r)$ and $\beta(r)$ profiles are also very close to the model $\tau_{\rm B4,model}(r)$ and $\beta_{\rm model}(r)$ profiles. Meanwhile, the derived dust properties deviate from the model in the outer disk region of $r > 40$ au, probably due to the rapid drop of β (see Section 4.4.2). The rapid drop of β in the outer disk region seems to be affected by the drop of α at 190 GHz, which is obtained by the MFS method. Also, in the disk region of $r > 50$ au, the SNRs of the observed intensities become small. By the convolution of large beam size, the noise at the very outer disk can contaminate to the disk region around $r \sim 40$ au.

The red shaded regions in each panel indicate the possible constraint ranges of the derived dust properties by assuming the derived red dotted line as the model profiles and considering the observational uncertainties of $\pm 10\%$ for the Band 4 and 6 and $\pm 20\%$ for the Band 9. While the constraint ranges of $T_{\rm d}(r)$ is still too broad at all radii, the constraint ranges of $\tau_{\rm B4}(r)$ and $\beta(r)$ profiles are relatively narrower than the ranges derived from the Band [7,6,4] set. It is because that the Band [9,6,4] set satisfies two conditions for the good band sets; It contains the Band 9 in the set and the large frequency intervals between the bands than the Band [7,6,4] set. Therefore, the results derived from the Band [9,6,4] set seems less affected by the observational uncertainties than those derived from Band [7,6,4] set, which is consistent with the synthetic ALMA multiband analysis results in Section 4.3.

The radial profiles of the derived dust properties in the center panels are smooth because the $T_{\rm d}$ bump at $r \sim 33$ au and the drop of $\tau_{\rm B4}$ and enhancement of β at the gap locations at $r \sim 25$ au and $r \sim 41$ au are smoothed out during the beam convolution process. It is because of the large difference between the beam sizes of the Band 9 and those of the Band 4 and 6. To check whether those small-scale structures are smoothed out by the large beam size, I derive the dust properties from the smoothed intensity radial profiles of the Band [7,6,4] set at $\sim 434 \times 247$ mas^2 beam size. The right panels of Figure 4.7 present the radial profiles of the dust properties derived from the smoothed intensity radial profiles of the Band [7,6,4] set as the green dotted lines. The derived $T_{\rm d}(r)$ profile has no bump around $r \sim 33$ au. The $\tau_{\rm B4}(r)$ and $\beta(r)$ profiles also have no structure at the gap location ($r \sim 25$ au and $r \sim 41$ au). It infers that the small-scale structures in the TW Hya disk are smoothed out by the convolution with the large beam. Therefore, I need a high spatial resolution observation at ALMA Band 9 or 10 for constraining the accurate ranges of the dust properties around the gap structures of the TW Hya disk using the ALMA multiband analysis in the future.

4.5.3 The possible origins of the gap structures in the TW Hya disk

In the previous subsections, I derived the dust properties from the ALMA Band [7,6,4] set and [9,6,4] set. In this subsection, I briefly discuss the possible origin of the observed gap structures using the derived dust properties in Figure 4.7. For the interpretation, I assume that the dotted lines in Figure 4.7 are the exact solutions of $T_{\rm d}$, $\tau_{\rm B4}$, and β because the uncertainties of the dust properties represented by the color shaded regions are too large to specify the values.

First possible mechanism is the planet-disk interaction (See Section 1.2.1). The enhancement of β inside the gap at $r \sim 25$ au and $r \sim 41$ au would be an indicator of the dust filtration. Some previous studies have estimated the planet masses at two gaps as $M_{\rm p} \sim$ 10-20 $M_{\oplus}$ from the observed gap depth and width depending on the different turbulence α values and gas temperatures (e.g., Tsukagoshi et al. 2016; Nomura et al. 2016; Matsuura & Okuzumi 2019). To examine the existence of the planet in the dust gap, the existence of the gas gap around the dust gap location would be good evidence. In addition, the spiral structures in the outer gas disk of $r \sim$ 70-200 au are observed recently in the ^{12}CO $J =$ 3-2 emission line (Teague et al. 2019). Since the gravitational perturbation on the disk by the embedded planet can make the spiral structures in the disk, the planet in the dust gap could be the origin of this gas spiral structures.

Second possible mechanism is the molecular snowlines (See Section 1.2.3; e.g., Zhu et al. 2012)The $T_{\rm d}$ derived from the Band [9,6,4] and [7,6,4] sets are $T_{\rm d} \sim$ 12-20 K within the radius ranges of 20 au $\leq r \leq$ 50 au. These temperature ranges are well matched to the sublimation temperatures of $T \sim$ 15-25 K for the CO and CH_4 molecules (Yamamoto 2017). Furthermore, the derived β values around $r \sim 25$ au and $r \sim 41$ au are $\beta \sim$ 1.5-1.7 which is similar to the ISM values. These features are consistent with the rapid grain growth model that the β enhancement inside the gap. These analyses are also consistent with the previous studies on the TW Hya disk (e.g., Nomura et al. 2016; Tsukagoshi et al. 2016).

I note that I consider two main uncertainties for the observational data, the calibration uncertainty and the random noises of the observations. For the synthetic ALMA multiband analysis, I assume that the calibration uncertainty dominates the random noises because the random noises are easily reduced by the data reduction techniques and the longer observing time. If the situation that the random noises dominate the total observational uncertainty, I can roughly estimate how small random noise is required to distinguish the enhancement of the temperature and β in the TW Hya disk for the high-resolution Band [7,6,4] set. The top-left panel of Figure 4.7 shows $\Delta\beta_{\rm model} \sim 0.5$ between the radius $r = 25$ au and $r = 33$ au, which are the dust gap and ring region in the TW Hya disk. To resolve the enhancements of $\beta_{\rm model}$ between the gap and ring regions as the 3σ detection, I need the sensitivity of the ALMA multiband analysis for $\Delta\beta_{\rm model} \sim 0.17$ corresponding to the observational uncertainties. If I set the $\pm1\%$ and $\pm3\%$ observational uncertainties of the ALMA Band [7,6,4] set instead of $\pm10\%$ for Band 4 and 6 and $\pm15\%$ for Band 7, the synthetic model calculation makes the uncertainties of $\Delta\beta_{\rm syn} \sim 0.13$ and ~ 0.25 at $r = 25$ au. It indicates that the dust continuum observations should have the SNR$\gtrsim 33$ for resolving the enhancements of the $\beta_{\rm model}$ in the dust properties of the TW Hya disk.

Chapter 5

Future aspects of the ALMA multiband analysis

In Chapter 4, I describe the synthetic ALMA multiband analysis to find the best three ALMA combination providing accurate constraint ranges of the dust properties from the observations. I also examine whether the synthetic ALMA multiband analysis is consistent with the real data by deriving the dust properties from the ALMA archival data at Band 4, 6, 7, and 9. The results indicate that the synthetic multiband analysis is well consistent with the archival data. However, the ALMA multiband analysis is tested for only one peculiar sample, the TW Hya disk which is an old population ($t \sim$ 3-10 Myr) but contains a substantial dust and gas materials of $M_{\rm disk} \geq 0.05\ M_{\odot}$ (Bergin et al. 2013). Furthermore, there are many assumptions for the simplicity of the calculations. In this chapter, I will discuss some future aspects of the ALMA multiband analysis, focusing on the applicability of this method to various disks and the possibility of breaking some assumptions used in the calculation.

5.1 The application to various protoplanetary disks

Although the ALMA multiband analysis makes successful results on the TW Hya disk, this method is still tested for only one sample yet. Therefore, I investigate whether the ALMA multiband analysis can be applied to the various disks in this section (Kim et al. 2019). I derive the $\pm1\sigma$ constraint ranges of the dust properties for the various model disk conditions of [$T_{\mathrm{d,model}}$, $\tau_{190\ \mathrm{GHz,model}}$, β_{model}] by generating the synthetic intensities to mimic the observations using the Monte-Carlo (MC) method, not restricted on the TW Hya disk. To do this analysis, I use the ALMA Band [10,6,3] set for minimizing the loss of the generated data because it is the best set of the synthetic multiband analysis for the TW Hya disk. I calculate the model intensities at ALMA Band 10, 6, and 3 based on the model dust properties using Equations 4.1 and 4.2. Then, I generate 1000 combinations of the synthetic intensity with the random observational uncertainties within $\pm10\%$ for the Band 3 and 6 and $\pm20\%$ for the Band 10. Finally, I derive the synthetic dust properties [$T_{\mathrm{d,syn}}$, $\tau_{190\ \mathrm{GHz,syn}}$, β_{syn}] by applying the ALMA multiband analysis to the generated 1000 combinations of the synthetic intensities.

For example, Figure 5.1 presents the 3-dimensional (3D) scatter plot of the [$T_{\mathrm{d,syn}}$, $\tau_{190\ \mathrm{GHz,syn}}$, β_{syn}] and their 2-dimensional (2D) scatter plots projected to each axis for the model values of [$T_{\mathrm{d,model}}$, $\tau_{190\ \mathrm{GHz,model}}$, β_{model}] = [20 K, 0.5, 1.5]. The red points in the 2D scatter plots indicate the model values. Since some intensity combinations do not have the solutions, The 825 black points are plotted from the generated 1000 combinations of the synthetic intensities. The black points are concentrated in a diagonal line in the 3D scatter plot of Figure 5.1. The 2D scatter plots of Figure 5.1 show the projected correlation between the dust properties. The blue ellipses in the 2D scatter plots indicate the 1σ confidence ellipse which contains $\sim$ 68% of the plotted points. They indicate the direction and strength of the correlations between the dust properties.

The ellipses are showing the negative correlations in the$T_{\rm d,syn} - \tau_{\rm 190\ GHz,syn}$ and the $T_{\rm d,syn} - \beta_{\rm syn}$ and the positive correlation in the $\tau_{\rm 190\ GHz,syn} - \beta_{\rm syn}$. And, the correlation between $T_{\rm d,syn} - \tau_{\rm 190\ GHz,syn}$ is the strongest correlation between them. These correlations can be explained by Equations 4.1 and 4.3. The τ_ν should decrease to cancel out the increment of $B_\nu(T_{\rm d})$ as $T_{\rm d}$ increases for a given intensity. At the same time, when $T_{\rm d}$ becomes higher, the deviation of the blackbody curve from the Rayleigh-Jeans limit gets smaller described in Section 4.4.3. To match the observed spectral index α, the β should decrease to cancel out the effect of $T_{\rm d}$ increase in Equation 4.3. Therefore, τ_ν and β have a positive correlation.

To examine the applicability of the ALMA multiband analysis, I derive the same results like Figure 5.1 using the same MC method for the various combinations of the model dust properties among $T_{\rm d,model}$ = [10 K, 20 K, 30 K, 50 K, 100 K, 150 K], $\tau_{\rm 190\ GHz,model}$ = [0.1, 0.25, 0.5, 1.0, 2.0, 3.0], and $\beta_{\rm model}$ = [0.5, 1.5]. Those model parameters cover a wide ranges of possible disk conditions, from cold (10 K) to hot (150 K), from optically thin ($\tau_{\rm 190\ GHz} \leq 0.5$) to thick ($\tau_{\rm 190\ GHz} \geq 1.0$), and with small grains ($\beta = 1.5$, $a_{\rm max} \lesssim 1$ mm) and large grains ($\beta = 0.5$, $a_{\rm max} \gtrsim 1$ cm) (e.g. Draine 2006). Then, I make the occurrence histogram of the derived [$T_{\rm d,syn}$, $\tau_{\rm 190GHz,syn}$, $\beta_{\rm syn}$] and pick the values at 16% (-1σ) and 84% ($+1\sigma$) of the histogram, as $T_{{\rm d,syn},\pm1\sigma}$ for example.

Figure 5.2 summarizes the normalized deviation of the $\pm1\sigma$ values from the model values, that is, $(T_{{\rm d,syn},\pm1\sigma} - T_{\rm d,model})/T_{\rm d,model}$, for example. These values are used to the quantitative comparisons for the accuracy of the derived synthetic dust properties at the different disk conditions. The normalized deviation of the $T_{{\rm d,syn},\pm1\sigma}$ (top row), $\tau_{{\rm 190\ GHz,syn},\pm1\sigma}$ (middle row), and $\beta_{{\rm syn},\pm1\sigma}$ (bottom row) are presented for a certain set of [$T_{\rm d,model}$,$\tau_{\rm 190\ GHz,model}$,$\beta_{\rm model}$] in each block. The x-axis indicates the $T_{\rm d,model}$

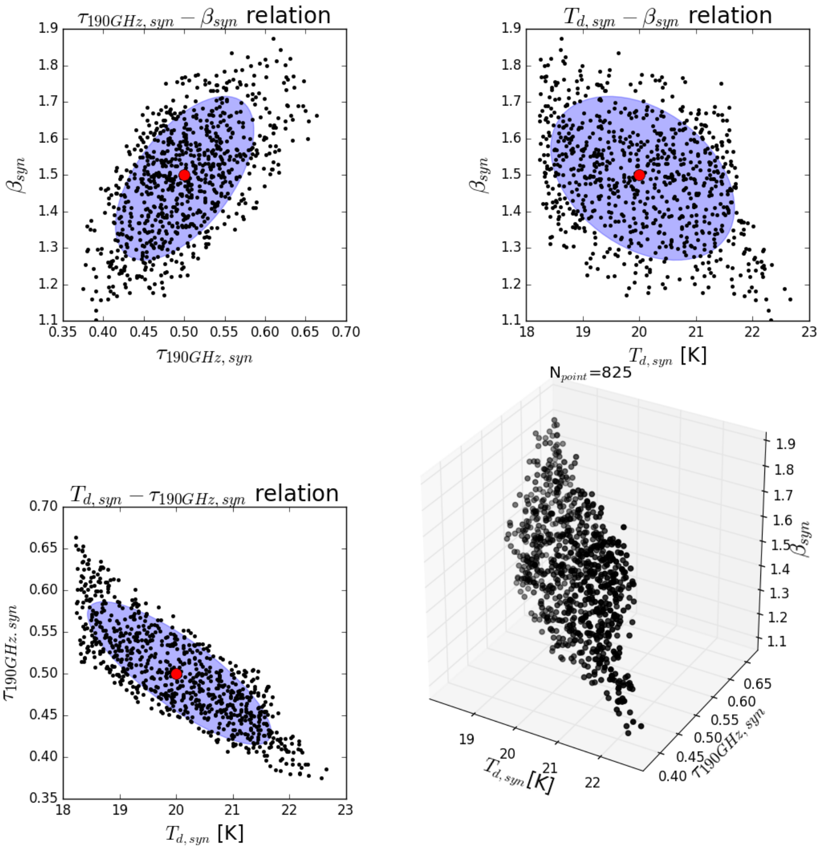

Figure 5.1. The 3D scatter plot of [$T_{\rm d,syn}$, $\tau_{\rm 190\ GHz,syn}$, $\beta_{\rm syn}$] derived from the randomly generated 1000 combinations of the synthetic intensities at ALMA Band [10,6,3] set (bottom-right) and their projected 2D scatter plots. The model dust properties of [$\rm T_{d,model}$, $\tau_{\rm 190\ GHz,model}$, $\beta_{\rm model}$] = [20 K, 0.5, 1.5] are plotted as red dot in the 2D scatter plots. The blue ellipses in the 2D scatter plots are the 1σ confidence ellipse which contains 68% of the plotted points. The points show the correlations between dust properties: $\tau_{\rm 190\ GHz,syn}$ and $\beta_{\rm syn}$ are getting smaller as $T_{\rm d,syn}$ becomes larger.

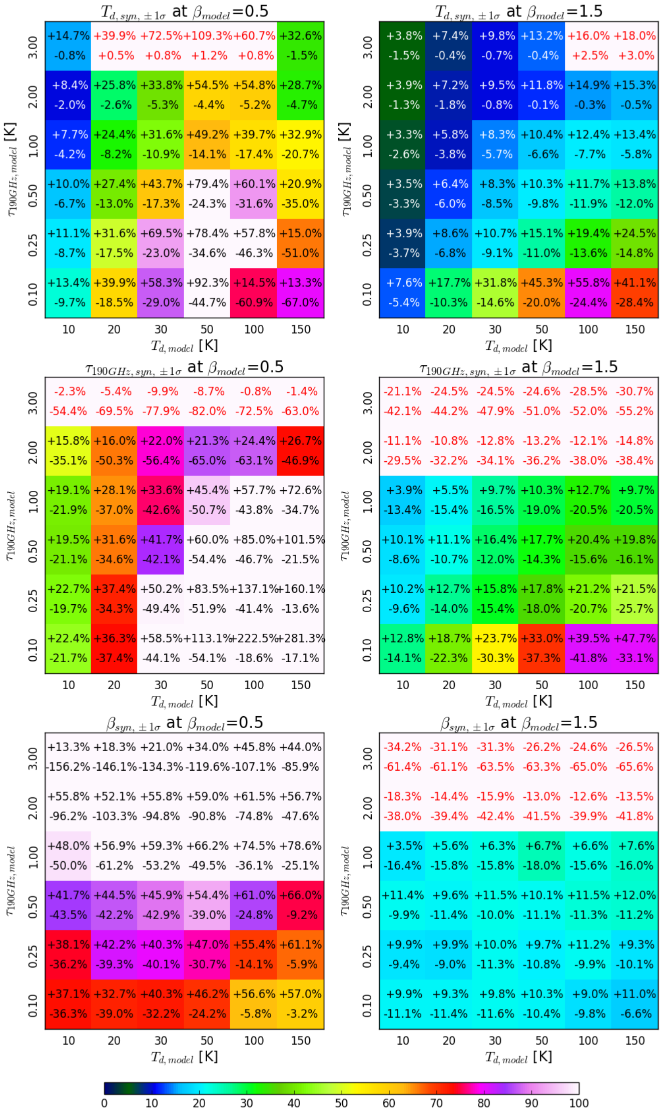

Figure 5.2. The $\pm 1\sigma$ values of the $T_{\rm d,syn}$ (top row), $\tau_{190\ \rm GHz,syn}$ (middle row), and $\beta_{\rm syn}$ (bottom row) derived from the scatter plots like Figure 5.1 for the various [$T_{\rm d,model}$, $\tau_{190\ \rm GHz,model}$, $\beta_{\rm model}$] values. In the panels, the x-axis indicates the $T_{\rm d,model}$ and the y-axis indicates the $\tau_{190\ \rm GHz,model}$. The left column indicates $\beta_{\rm model} = 0.5$ and the right column indicates $\beta_{\rm model} = 1.5$. The percentages written in each block indicate the normalized deviation of $+1\sigma$ (upper) and -1σ (lower) values from the model values. The red numbers indicate the cases that the model value is not included in the $\pm 1\sigma$ range. Background colors indicate the total width between $\pm 1\sigma$ values normalized by the model value.

and the y-axis indicates the $\tau_{190\ \mathrm{GHz,model}}$. The $\beta_{\mathrm{model}} = 0.5$ and 1.5 are used for the analysis of Figure 5.2 in the left and right columns, respectively.

The percentages written in each block indicate the normalized deviation of $+1\sigma$ (upper) and -1σ (lower) values from the model values. The red numbers in some blocks indicate the cases in which the model value is not included in $\pm 1\sigma$ range, that is, the model value is not reproduced by the ALMA multiband analysis. It occurs when large uncertainties exist in the derived dust properties, for example, in the case of large $\tau_{190\ \mathrm{GHz,model}}$. The background colors of the blocks correspond to the total width between the $+1\sigma$ and -1σ values normalized by the model value: $(A_{\mathrm{syn},+1\sigma} - A_{\mathrm{syn},-1\sigma})/A_{\mathrm{model}}$ where A is T_{d}, $\tau_{190\ \mathrm{GHz}}$, and β. For example, in the top-right panel of Figure 5.2, for the model values of [$T_{\mathrm{d,model}}$, $\tau_{190\ \mathrm{GHz,model}}$, β_{model}] = [20 K, 1.0, 1.5], the $T_{\mathrm{d,syn},+1\sigma} \approx 21.16$ K ($+5.8\%$) and $T_{\mathrm{d,syn},-1\sigma} \approx 19.24$ K (-3.8%). Then, the total width between the $\pm 1\sigma$ values normalized by the model value is 9.6%.

According to the derived numbers in Figure 5.2, I obtain the small constraint ranges of the dust properties with low $T_{\mathrm{d,model}}$, intermediate $\tau_{190\ \mathrm{GHz,model}}$, and high β_{model}. This is consistent with the interpretations of the ALMA multiband analysis in Section 4.4. In addition, the $\tau_{190\ \mathrm{GHz,model}}$ and β_{model} have more strict ranges for deriving the accurate dust properties corresponding to the observational uncertainties than $T_{\mathrm{d,model}}$. That is, selecting the combination of optically thick and thin bands is the primary factor for obtaining the accurate constraint ranges of the dust properties using the ALMA multiband analysis. For the cases of $\tau_{190\ \mathrm{GHz,model}} \geq 2.0$, the Band 10, 6 and 3 are all optically thick which is not suitable for constraining the optical depth accurately. Also, for the cases of $\tau_{190\ \mathrm{GHz,model}} \leq 0.25$, the Band 10, 6 and 3 are all optically thin which is not suitable for constraining the τ_{ν} and the T_{d} accurately due to the degeneracy of them in Equation 4.1.

This analysis result concludes that the ALMA multiband analysis can be applied to the various disks for deriving the accurate constraint ranges of the dust properties if I select the combination of optically thick and thin ALMA bands. Also, when the disk has the conditions of low $T_{\rm d}$ and high β, the ALMA multiband analysis has an advantage for constraining the accurate dust properties against the observational uncertainties.

5.2 Extension to ALMA Band 1

Section 4.4.4 presents the frequency intervals between the bands should be large enough for better constraints on the dust properties through the ALMA multiband analysis. It infers that I can obtain the better constraint ranges of the dust properties if I use a lower frequency ALMA band instead of the Band 3 ($\nu_{\rm rep} \sim 112$ GHz) in the band sets. Since ALMA Band 1 receiver has been developing (Huang et al. 2016), I examine whether the ALMA multiband analysis can obtain the narrower constraint ranges on the dust properties using the band sets including Band 1 ($\nu_{\rm rep} \sim 40$ GHz) (Kim et al. 2019).

Figure 5.3 presents the constraint ranges of the synthetic dust temperature $T_{\rm d,syn}$ (top), the synthetic dust optical depth at Band 1 $\tau_{\rm B1,syn}$ (middle), and the synthetic dust opacity power-law index $\beta_{\rm syn}$ (bottom), derived by the synthetic ALMA multiband analysis from five ALMA band sets including Band 1. The constraint ranges of the synthetic dust properties for different band sets are represented by different colors; yellow for the Band [9,7,1] set, purple for [9,6,1] set, blue for [10,7,1] set, red for [10,6,1] set, and green for [10,5,1] set. The black solid lines are the model profiles of $T_{\rm d}(r)$, $\tau_{\rm B1,model}(r)$, and $\beta(r)$ derived through the process described in Section 4.2.1. The derived constraint ranges of $T_{\rm d,syn}$ are narrower than the ones derived from the band sets including Band 3, such as the Band [10,6,3] set. Furthermore, the constraint ranges of $\tau_{\rm B1,syn}$ and $\beta_{\rm syn}$ also become much narrower than the constraint ranges shown in Figure

4.2. Since the band sets including Band 1 have larger frequency intervals between the bands in the set than Band 3, the dust properties are constrained more accurately by the ALMA multiband analysis. Therefore, the Band 1 observations toward the protoplanetary disks will improve the ALMA multiband analysis results by providing the narrower constraint ranges of the dust properties. The uncertainties of $\beta_{\rm syn}$ and $\tau_{\rm B1,syn}$ are less than 0.1 in the region $r \gtrsim 20$ au. Compared to Figure 4.2, those results can support the β enhancement inside the gap at $r \sim 25$ au and $r \sim 41$ au. The β enhancement can be used as the observational evidence of the planet-disk interaction or the molecular snowline scenarios.

5.3 The synthetic ALMA multiband analysis with four ALMA bands

I performed the synthetic multiband analysis for three ALMA bands for deriving the dust properties in the previous sections. In a mathematical approach, three inputs are enough to solve three unknowns with three equations. When I use four inputs into three equations to solve three unknowns, the unknowns could be constrained more strictly than the solutions derived by three inputs. In this section, I examine the synthetic multiband analysis results using four ALMA bands and whether they constrain the dust properties better than the results in Section 4.3.

The synthetic multiband analysis using four ALMA bands shows the same trends with the results derived from the three ALMA band combinations: the band sets including Band 9 or 10 and having enough large frequency intervals between the bands in the sets provide the narrow constraint ranges on the dust properties. I apply the synthetic ALMA multiband analysis to all the possible 70 combinations of four ALMA bands

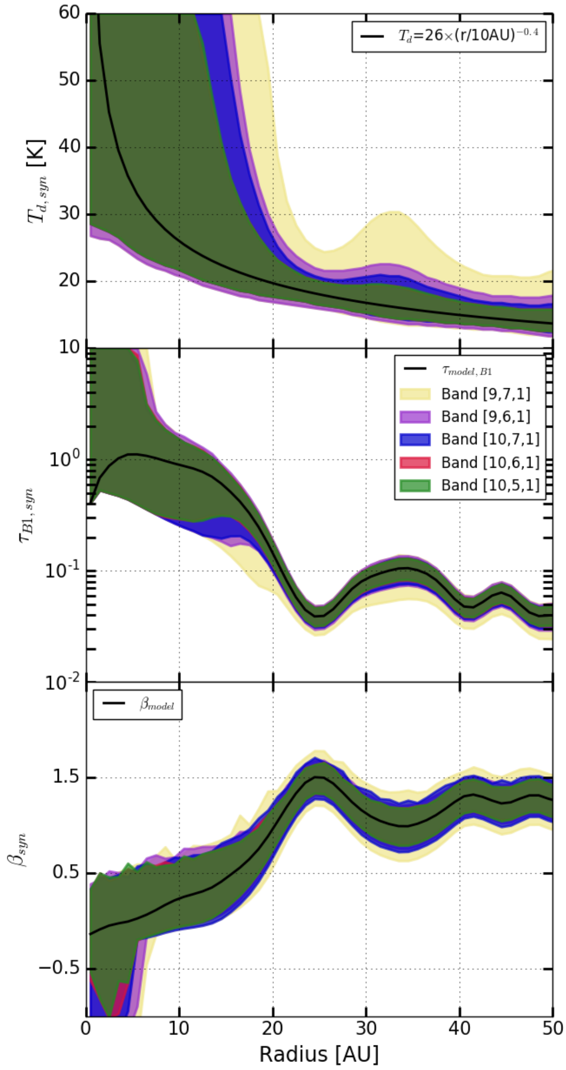

Figure 5.3. The constraint ranges of the synthetic dust temperature $T_{\rm d,syn}$ (top), the synthetic optical depth at ALMA Band 1 $\tau_{\rm B1,syn}$ (middle), and the synthetic opacity power-law index $\beta_{\rm syn}$ (bottom) derived from five ALMA band sets using the synthetic multiband analysis. The different colors represent the different ALMA band sets; the Band [9,7,1] set by yellow, [9,6,1] set by purple, [10,7,1] set by blue, [10,6,1] set by red, and [10,5,1] set by green. The black solid lines in each panel are the model radial profiles of $T_{\rm d,model}$, $\tau_{\rm B1,model}$, and $\beta_{\rm model}$. Compared with Figure 4.2, the band sets with Band 1 provide the better constraint ranges of the dust properties than the band sets with Band 3.

among the total of 8 ALMA bands from Band 3 to 10 to derive constraint ranges of the synthetic dust properties. For quantitative comparisons between the band sets, I calculate the normalized average deviation of the maximum synthetic dust temperature $T_{\rm d,syn,max}$ from the model dust temperature $T_{\rm d,model}$ within the radius range of 20 au $\leq r \leq$ 45 au, the parameter expressed by Equation 4.5 in Section 4.3.

Figure 5.4 presents the normalized average deviations of $T_{\rm d,syn,max}$ from $T_{\rm d,model}$ with the same format of Figure 4.1. The bottom-left triangle presents the normalized average deviations of the $T_{\rm d,syn,max}$ of the Band [10, x1, y1, 3] sets where x1=[9,8,7,6,5] and y1=[8,7,6,5,4]. The top-right triangle presents the deviations of the Band [9, x2, y2, 3] sets where x2=[8,7,6,5] and y2=[7,6,5,4]. The numbers in percentages at each block indicate the average deviation of $T_{\rm d,syn,max}$ normalized by the $T_{\rm d,model}$ within 20 au $\leq r \leq$ 45 au. The background colors represent the derived average normalized deviation values. The results derived from the Band [10,x1,y1,3] sets are very accurately constrained the dust temperature ($\lesssim 35\%$) except the Band [10,9,4,3] set. Meanwhile, the Band [9,x2,y2,3] sets have relatively higher deviations of $T_{\rm d,syn,max}$ from the model value than the Band [10,x1,y1,3] sets. It indicates that Band 10 is better to constrain the dust temperatures than Band 9. It is consistent with the interpretation in Section 4.4.3. Also, the Band [10,9,4,3] set and Band [9,8,4,3] set have an average deviation of 174$\%$ from the model dust temperature because the bands in the sets are very close making the large uncertainty of the spectral index α. This is consistent with the interpretation in Section 4.4.4 as well.

Figure 5.5 presents the constraint ranges of five examples of the four ALMA band combinations on the synthetic dust temperature $T_{\rm d,syn}$ (top), the synthetic dust optical depth at Band 3 $\tau_{\rm B3,syn}$ (middle), and the synthetic dust opacity power-law index $\beta_{\rm syn}$. The different color represents the different band combinations: the Band [8,6,5,3]

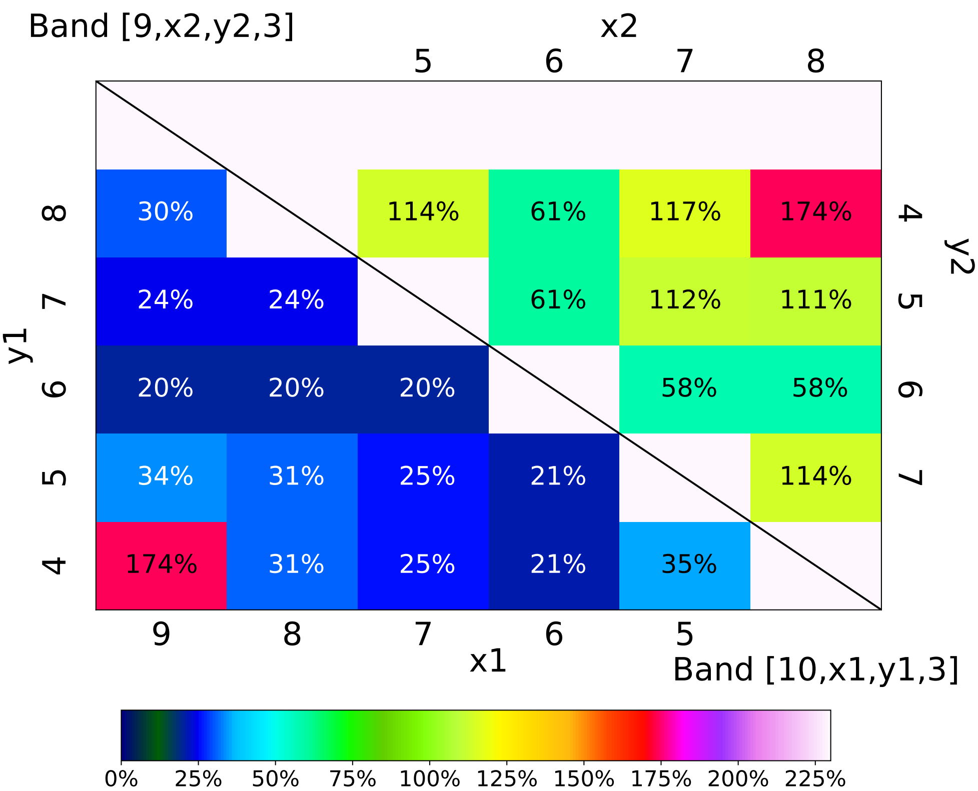

Figure 5.4. The average deviations of $(T_{\mathrm{d,syn,max}} - T_{\mathrm{d,model}})/T_{\mathrm{d,model}}$ within 20 au $\leq r \leq$ 45 au for the four ALMA band combinations. The left-bottom triangle presents the values derived from the Band [10, x1, y1, 3] sets where x1=[9, 8, 7, 6, 5] and y1=[8, 7, 6, 5, 4]. The right-top triangle presents the values derived from the Band [9, x2, y2, 3] sets where x2=[8, 7, 6, 5] and y2=[7, 6, 5, 4]. The background colors of the blocks represent the derived average deviation of $T_{\mathrm{d,syn,max}}$.

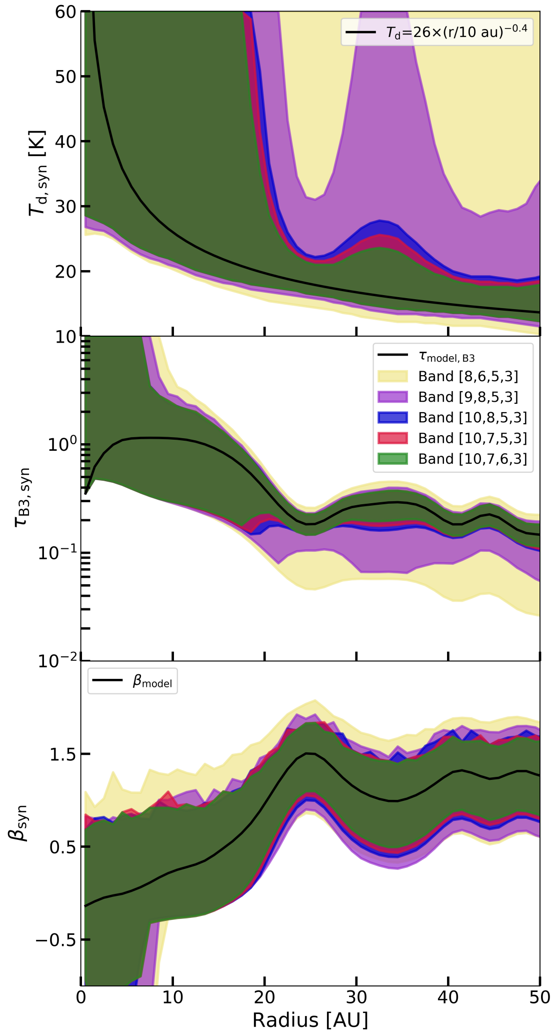

Figure 5.5. The constraint ranges of the synthetic dust temperature $T_{\rm d,syn}$ (top), the synthetic optical depth at ALMA Band 3 $\tau_{\rm B3,syn}$ (middle), and the synthetic opacity power-law index $\beta_{\rm syn}$ (bottom) derived from the five combinations of four ALMA bands using the synthetic multiband analysis. The different colors represent the different ALMA band sets; the Band [8,6,5,3] set by yellow, [9,8,5,3] set by purple, [10,8,5,3] set by blue, [10,7,5,3] set by red, and [10,7,6,3] set by green. The black solid line shows the model radial profile of $T_{\rm d,model}$, $\tau_{\rm B1,model}$, and $\beta_{\rm model}$ calculated by the process described in Section 4.2.1.

set by yellow, [9,8,5,3] set by purple, [10,8,5,3] set by blue, [10,7,5,3] set by red, and [10,7,6,3] set by green. The color-shaded regions indicate the possible constraint ranges of the synthetic dust properties corresponding to the observational uncertainties at each ALMA band considered in Section 4.2.2. As the same as Figure 4.2, the constraint ranges become narrower for the band sets including Band 9 or 10 and having large frequency intervals between the bands in the sets. The band sets which Band 8 is the highest frequency band in the set have very broad constraint ranges on the dust temperature. It is consistent with the interpretation of Section 4.4.3 for the three band combinations.

One interesting pattern in Figure 5.4 is the normalized average deviation of the $T_{\rm d,syn,max}$ derived by the four ALMA band combinations are comparable to the value of the best sub-combination of three ALMA bands among four bands in the sets. For example, the Band [10,9,6,3], [10,8,6,3], [10,7,6,3], [10,6,5,3], and [10,6,4,3] sets have $\sim$ 20-21% deviation of the $T_{\rm d,syn,max}$ from the model on average within the 20 au $\leq r \leq$ 45 au. It is comparable to the results of the Band [10,6,3] set in Figure 4.1, which is the best combination using three bands for the ALMA multiband analysis.

Figure 5.6 presents the possible constraint ranges of the synthetic dust temperature $T_{\rm d,syn}$ (top), the synthetic optical depth at Band 3 $\tau_{\rm B3,syn}$ (middle), and the synthetic opacity index $\beta_{\rm syn}$ derived by the synthetic ALMA multiband analysis from the Band [10,7,6,3] set and their sub-combinations of three bands: the Band [7,6,3] set by yellow, [10,7,3] set by blue, [10,6,3] set by red, and [10,7,6,3] set by green. The black solid lines in each panel indicate the model radial profiles of $T_{\rm d,model}$, $\tau_{\rm B3,model}$, and $\beta_{\rm model}$ following the procedures described in Section 4.2.1. As the same as Figure 5.5, all the color shaded regions are overlapped. The color shaded region of the Band [10,7,6,3] set is almost the same as the region of the Band [10,6,3] set. Consistently, the constraint ranges derived from a four band set largely follow the constraint ranges of the best sub-combination of three ALMA bands among their sub-combinations. It indicates that the ALMA multiband analysis results are comparable between the three band combinations and the four band combinations. Therefore, the three bands are enough to derive the dust properties in the protoplanetary disks using the ALMA multiband analysis with the present settings.

However, as I will discuss in the next section, I need to consider the dust temperature gradient along the disk vertical direction or the frequency dependency of β for making a more realistic disk model. If I adopt the parameterized equations of $T_{\rm d}(\nu) \propto \nu^{\gamma}$ for the model of the dust temperature gradient along the disk vertical direction or $\beta_{\nu}(\nu) \propto \nu^{\gamma}$ for the frequency dependence of β, I need one more observational data to derive four dust properties, $T_{\rm d}(\nu)$, τ_{ν}, β_{ν}, and γ. These are the next step to improve the ALMA multiband analysis in the future.

5.4 The limitation of the ALMA multiband analysis

The ALMA multiband analysis makes meaningful constraints on the dust properties from the observational data presented in Chapter 4. However, the calculation uses many assumptions for simplicity. In this section, I describe some assumptions of the disk structures and their possible improvement in the future (Kim et al. 2019).

5.4.1 The vertical structure of the disk

In the processes of the synthetic multiband analysis, I assume the homogeneous vertical structure of the disk. However, the realistic model of protoplanetary disks have gradients of the temperature and density structures along the disk vertical direction (e.g. Chiang & Goldreich 1997; Dullemond et al. 2002; Inoue et al. 2009). Furthermore, observationally, Teague et al. (2018) has reported that the gas temperature of $T_{\rm gas} \approx 40$

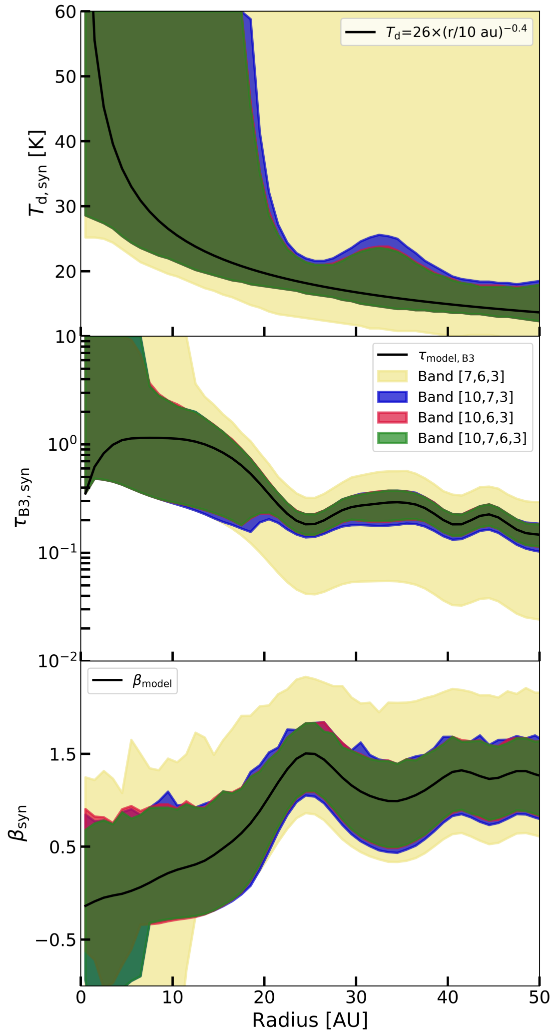

Figure 5.6. The constraint ranges of the synthetic dust temperature $T_{\mathrm{d,syn}}$ (top), the synthetic dust optical depth at ALMA Band 3 $\tau_{\mathrm{B3,syn}}$ (middle), and the synthetic dust opacity power-law index β_{syn} (bottom) derived from the Band [10,7,6,3] set and their sub-combinations of three bands using the synthetic multiband analysis. The different colors represent the different ALMA band sets; the Band [7,6,3] set by yellow, [10,7,3] set by blue, [10,6,3] set by red, and [10,7,6,3] set by green. The black solid lines in each panel are the model radial profiles of $T_{\mathrm{d,model}}$, $\tau_{\mathrm{B3,model}}$, and β_{model} described in Section 4.2.1. The results of the Band [10,7,6,3] set are almost the same with the results of the best sub-combination of three bands, the Band [10,6,3] set.

K in the inner region ($r \lesssim 100$ au) of the TW Hya disk derived from the multiple transition lines of CS molecule. Similarly, Loomis et al. (2018) also derive the rotational temperature of $T_{\rm rot} \approx 32$ K from the multiple transition lines of CH_3CN molecule in the TW Hya disk. Since those molecular lines are thought to be emitted from the upper disk surface layers, they indicate the vertical structure can exist in the TW Hya disk compared to the dust temperature of $T_{\rm d} \sim$ 20-30 K at the disk midplane derived from the ALMA multiband analysis.

If the dust continuum emission is optically thin, the emission is the result of integration throughout the vertical direction of the disk, and mainly traces the disk midplane since dust grains are concentrated near the midplane by settling. Therefore, the assumption of a homogeneous vertical structure would not affect the result very much. Meanwhile, if the dust continuum emission is optically thick, I need to be more careful about the disk vertical structure. Since the dust opacity generally increases with frequency, if the dust column density is high enough, the dust continuum emission becomes optically thick at different layers in the disk vertical direction depending on the observing frequencies. In this case, the assumption of the homogeneous vertical structure of dust temperature could affect the result of the synthetic multiband analysis.

If the irradiation from the central star is the dominant heating source, the dust temperature increases along the vertical direction. Figure 5.7 (Figure 2 of Inoue et al. 2009) presents the temperature profile as a function of the optical depth in the vertical direction of the disk. In the region where the Planck mean optical depth with the stellar effective temperature ($T_{*,\rm eff}$) of 3000 K is larger than the unity, the temperature is almost constant in the vertical direction, although it depends on the dust model. Hence, the optical depths at the ALMA Bands are $\sim$ 1-10^3 times smaller than the Planck mean optical depth at a given $T_{*,\rm eff}$, depending on the dust size (e.g. Miyake & Nakagawa 1993). For

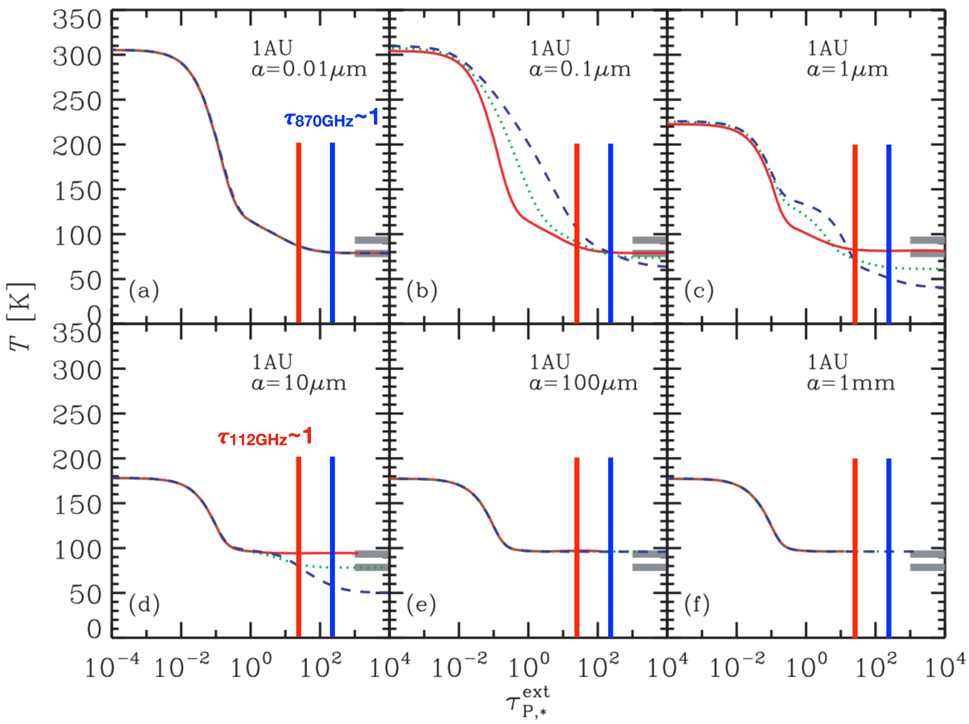

Figure 5.7. The vertical temperature structure model at 1 au with the different dust size from 0.01 μm to 1 mm (Figure 2 of Inoue et al. (2009)). The horizontal axis indicates the Planck mean extinction optical depth against the stellar radiation emitted from the effective temperature of 3000 K. The line styles indicate the different dust models: no scattering as solid lines, single scattering albedo of $\omega_0 = 0.9$ for small wavelength as dotted lines, and $\omega_0 = 0.99$ as dashed lines. I add the vertical solid lines to indicate the photosphere of ALMA Band 3 at 112 GHz (red) and Band 10 at 870 GHz (blue).

example, if I adopt the dust model with the dust size of 10 μm, the Planck mean optical depths at the photosphere ($\tau_\nu = 1$) of ALMA Band 3 at 112 GHz and Band 10 at 870 GHz are derived as $\tau_*^{\rm ext} \sim 33.3$ and $\tau_*^{\rm ext} \sim 250$. The red and blue solid vertical lines in Figure 5.7 indicates the photospheres at ALMA Band 3 and 10. The temperatures at both photospheres are almost the same at all dust models. Therefore, there might not be a gradient of the dust temperature in the region where the dust emission becomes optically thick at the ALMA bands. In this case, it could be reasonable to assume that the effect of the dust temperature gradient on the synthetic analysis is not very large.

Meanwhile, if the viscous heating is dominant, the dust temperature near the midplane increases. In this case, the temperature gradient could affect the result of the synthetic ALMA multiband analysis more significantly. According to the model calculations (e.g. D'Alessio et al. 1998), the viscous heating will be dominant only in the inner region ($r \lesssim 1$ au) if the accretion rate is small ($\dot{M} \sim 10^{-8}\ M_\odot$ yr^{-1}). The viscous heating also becomes dominant in the outer disk for larger accretion rates (e.g. Dullemond et al. 2007). Since this study focuses on the relatively outer disk (20 au$\leq r \leq 50$ au) and the TW Hya disk has small accretion rate, $\dot{M} \sim 10^{-8}\ M_\odot$ yr^{-1}, the viscous heating effect could be ignorable for applying the ALMA multiband analysis to the TW Hya disk.

The inclination of the disks could also affect the optical depths along the line-of-sight. If the disk is almost edge-on, the dust continuum emission becomes optically thick and the assumption of a homogeneous structure along the line-of-sight is no more valid. However, in the case of the TW Hya disk, the inclination is small ($i \sim 7^\circ$, Qi et al. 2008) and the line-of-sight direction is not very different from the vertical direction of the disk. Thus, additional observations at different frequencies will help us to constrain the dust properties when they have a non-uniform structure along the line-of-sight.

As I introduce briefly at the end of Section 5.3, I can consider the temperature gradient in the disk vertical direction when I use four ALMA bands with the parameterization of $T_{\rm d}(\nu) \propto \nu^{\gamma}$. Although the assumption of the homogeneous vertical disk is enough in this stage, I can improve the ALMA multiband analysis with a more realistic disk model in the future.

5.4.2 The frequency dependency of β

I assume the dust opacity is proportional to the frequency as $\kappa_{\nu} \propto \nu^{\beta}$ where β is independent of the frequency for the ALMA multiband analysis. This power-law index β is strongly related to the dust grain models in the disks: the dust size distribution, the size of the grains, the internal structure of the grains, and the composition of the grains. Therefore, I can infer the dust properties in protoplanetary disks by comparing the observed β value with the theoretical/experimental β values (e.g. Beckwith et al. 2000). The β of the grains in the interstellar clouds is observationally measured as $\beta \approx 1.7$. Meanwhile, many observations of PPDs show $\beta \leq 1$ (e.g. Beckwith & Sargent 1991), and the recent spatially resolved observations show β is smaller in the inner region of the disks (e.g. Pérez et al. 2012; Tsukagoshi et al. 2016), suggesting further grain growth close to the central stars. It is consistent with grain growth theory which leads to planet formation (e.g. Armitage 2010).

Theoretical/Experimental studies of dust opacity have reported that β can be varied depending on the frequencies and the dust properties, such as dust temperature, grain size distribution, and composition (e.g. Miyake & Nakagawa 1993; Mennella et al. 1998; Chihara et al. 2002; Draine 2006; Koike et al. 2006; Min et al. 2016; Woitke et al. 2016). Figure 5.8 (Figure 3 of Draine 2006) showing the β models for the different size distribution. Depending on the maximum grain size, the β varies in the frequency ranges of 10^2 GHz $\leq \nu \leq 10^3$ GHz which is the coverages of ALMA observations. Also, Demyk et al. (2017a,b) recently report the variations of β on the frequencies by the experimental measurements for the particles with the different dust temperatures ($T_{\rm d}$ = 10-300 K) and the chemical compositions (Mg-rich or Fe-rich amorphous silicates). They suggest that the β anti-correlates with $T_{\rm d}$ at a given frequency for $T_{\rm d} > 30$ K due to the additional absorption processes of the grains. They also find the complex β variations at $\lambda \geq 100$ μm for the different $T_{\rm d}$ and compositions.

Despite those theoretical/experimental studies on β with the dust grain models, it is difficult to fully understand the frequency dependence of β of actual grains in PPDs. Therefore, I simply assumed frequency-independent β in the ALMA multiband analysis. If I take into account the β variation on the frequencies by adopting the equation $\beta_\nu \propto \nu^\gamma$, I need additional observations at different frequencies to make the combinations of four ALMA bands in the future.

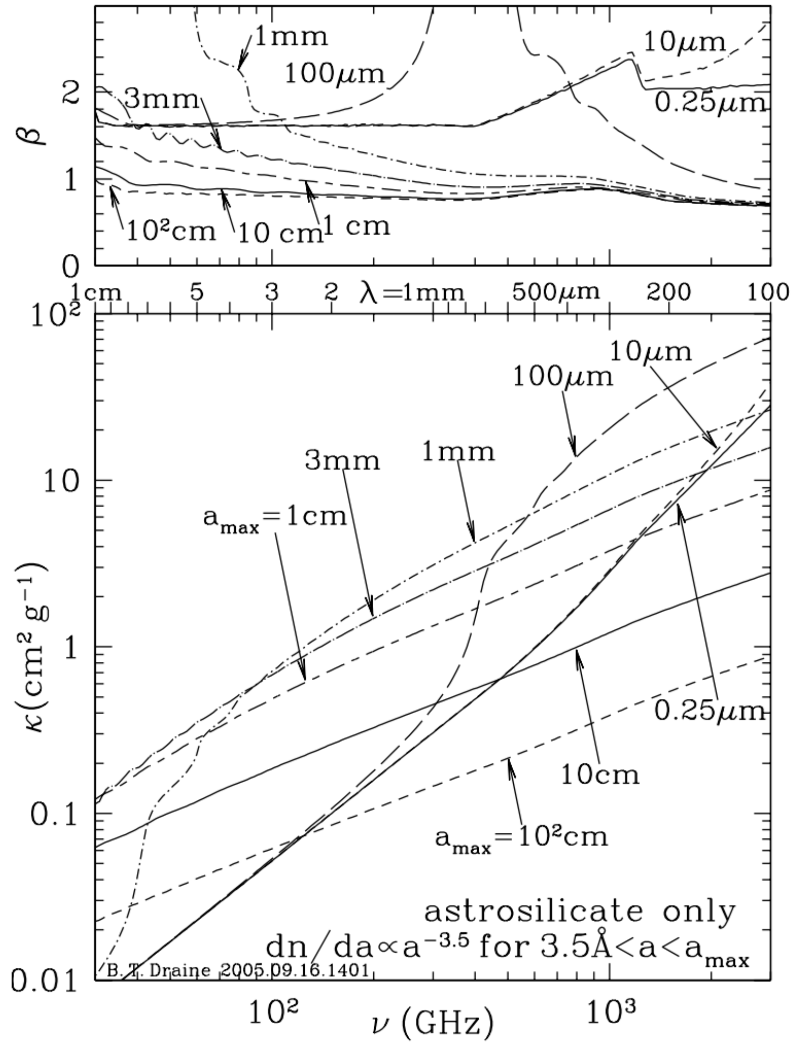

Figure 5.8. The dust opacity κ_ν and the opacity power-law index β_ν models for the amorphous silicate spheres with the size distribution of $dn/da \propto a^{-3.5}$ for $3.5\mathring{A} < a < a_{\max}$ (Figure 3 of Draine 2006). The β_ν model varies along the frequency and the maximum size $a_{\max}$.

Chapter 6

Summary

Since the axisymmetric ring-gap structure is thought to be a signpost of a forming planet in protoplanetary disks, the origin of this structure is one of the important topics to understand the planet formation theories. Although the theoretical/numerical studies suggest some possible mechanisms to explain their origin described in Section 1.2, the observational supports have not been provided enough to distinguish which mechanism is the most plausible for the gap structure. Therefore, I try to study the origin of the axisymmetric ring-gap structures in protoplanetary disks using the ALMA observational data in this thesis. I derive the dust and gas properties from the single wavelength ALMA data of the CR Cha disk and multiwavelength ALMA data of the TW Hya disk to provide the observational evidence for distinguishing the gap origins in those disks.

In Chapter 2, I present the images of the dust continuum at 225 GHz and the CO isotopologue $J = 2$-1 emission lines of the CR Cha disk. The observed dust continuum image presents a dust gap at $r \sim 90$ au and a faint dust ring at $r \sim 120$ au. It is the first time to resolve the disk substructure in the CR Cha disk. The Gaussian fitting on the dust surface density around the gap structure indicates that the dust gap is located at $r = 91.47$ au and has a gap depth of $\sim 20\%$ with ~ 8 au width on average. The CO isotopologue $J = 2$-1 emission lines in the CR Cha disk present that the gas disk is smoothly extended up to ~ 240 au, which is much larger than the dust disk. The ratios between the CO line intensities are larger than 0.2 at all radii, larger than the typical abundance ratios of the CO isotopologue molecules in the protoplanetary disks. It indicates that the ^{12}CO and ^{13}CO lines are optically thick so that those lines can be used to derive the gas temperature. I make the azimuthally averaged peak intensity radial profiles of the ^{12}CO and ^{13}CO lines without dust continuum subtraction because they are optically thick lines. The peak intensity profile of the ^{13}CO line shows a small bump around r ~130 au, which may indicate the temperature bump in the ^{13}CO line emitting region.

In Chapter 3, I investigate two possible mechanisms to explain the origin of the observed disk substructures in Chapter 2: (1) a gap opening by a planet and (2) dust trapping at the gas pressure bump. First, for the gap opening scenario by a planet, I compare the observed dust surface density distribution around the gap structure to the model dust surface density obtained by Kanagawa et al. (2017). The planet mass of $M_{\rm p} \approx (0.99 \pm 0.15) M_{\rm J} \, (\alpha/0.01)^{1/2}$, where α is the dimensionless turbulent viscous parameter, can reproduce the observed dust surface density around the gap. However, this value has large uncertainties: the synthesized beam size comparable to the gap width only constrains the upper limit of the gap depth and the gas gap structure may not be traced well by the observed dust gap structure. Thus, this value should be considered as a very rough estimation. After the gap is opened by a planet, the outer wall of the gap is heated by the stellar radiation making a temperature bump at the outer edge of the gap structure like the observed temperature bump in the ^{13}CO line.

Second, the dust trapping scenario is the creation mechanism of the dust ring structure at the outside of the dense dust disk. For investigating this scenario, I run the radiative transfer calculation to calculate the gas temperature distribution in the disk. The disk structure is adopted the observed dust surface density and $C^{18}O$ column density to consider the situation that the dust disk becomes more compact than the gas disk by the radial drift of the dust grains. And, two population grain model is adopted: the small and large dust grains. The calculated temperature distribution shows the temperature bump at the outer edge of the dust disk. It may be caused by the steep decreasing gradient of the dust surface density around the outer edge of the dust disk. It makes the efficient heating by the irradiation from the hot disk upper surface to the small dust grains than the large dust grains. Also, the gas temperature bump beyond the dust disk is produced because the small dust grains are coupled with the gas. It can make the pressure bump at the outer edge of the dust disk. Then, the dust grains may be trapped at the gas pressure bump making a dust ring structure. Since the optical depth of the ^{13}CO line emission is smaller than that of the ^{12}CO line, it traces the temperature at the layer close to the midplane where a temperature bump is seen at $r \sim 130$ au. Meanwhile, the ^{12}CO line does not show a bump structure because this line traces a very hot upper layer where has a smooth temperature distribution.

Although two possible mechanisms I investigate could explain the observed disk substructures well, the dust sintering effect and the secular gravitational instability also may explain the observed dust ring-gap structure and the gas temperature bump beyond the dust gap. However, I need further investigation on the grain size distribution for distinguishing the origin of the disk substructure in the CR Cha disk more clearly in the future.

The study on the CR Cha disk has a limitation on the derivation of the dust and gas properties because the single wavelength data cannot break the degeneracy in the radiative transfer equation, $\mathrm{I}_\nu = \mathrm{B}_\nu(\mathrm{T_d})\,[1-\exp(-\tau_\nu)]$. Therefore, the multiwavelength analysis is needed to break this degeneracy. To find the best ALMA band set providing the accurate constraint ranges of the dust properties, I perform the synthetic ALMA multiband analysis to the ALMA archival data of the TW Hya disk with the Equations 4.1−4.3 in Chapter 4. The synthetic ALMA multiband analysis results of all the possible 56 combinations of three ALMA bands among Band 3 to 10 indicate that the Band [10,6,3] set is the best combination for obtaining the most accurate constraint ranges of $\mathrm{T_d}$, τ_ν, and β in the TW Hya disk, considering the observational uncertainties of $\pm10\%$ for Band 3, 4, 5, and 6, $\pm15\%$ for Band 7 and 8, and $\pm20\%$ for Band 9 and 10. Also, I find two common conditions for the good ALMA band sets from the results that (1) Band 9 or 10 is included in the band sets and (2) the frequency intervals between the bands in the set are large enough. Through the examinations of the effects of dust properties on the synthetic ALMA multiband analysis, these conditions are converted to the combination of optically thick and thin bands, high β values, and low dust temperature at high-frequency bands.

To check whether the synthetic ALMA multiband analysis is consistent with the observational data, I apply the ALMA multiband analysis to the ALMA archival data of the TW Hya disk, the Band [7,6,4] set as high-resolution data set and the Band [9,6,4] set as low-resolution data set. The dust properties derived from the Band [7,6,4] set has some deviations from the model values, while the dust properties derived from the Band [9,6,4] set are well-matched with the model values. Also, the constraint ranges of the dust properties derived from the Band [9.6.4] set are narrower than the ranges derived from the Band [7,6,4] set. Since the Band [9,6,4] set is satisfying two conditions for the good ALMA band sets, Band 9 is included in the set and the frequency intervals between the bands are large enough, it can constrain more accurate dust properties from the observations than the Band [7,6,4] set.

Chapter 5 describe the future aspects of the ALMA multiband analysis. First, since the TW Hya disk is a quite peculiar object, I need to examine the applicability of the ALMA multiband analysis to various disks having different conditions. Therefore, I derive the accuracy of the constraint ranges of the dust properties using the Monte-Carlo method for the various model dust properties. According to the results, I obtain the good constraint ranges on the dust properties with low $T_{\rm d,model}$, intermediate $\tau_{190\ {\rm GHz,model}}$ and high $\beta_{\rm model}$. This conclusion is consistent with the synthetic analysis results for the TW Hya disk and indicates that I should select the optically thick and thin bands for obtaining the accurate constraints of the dust properties. That is, I can apply the ALMA multiband analysis not only to the TW Hya disk but also to the various protoplanetary disks if I select a proper combination of wavelengths for the protoplanetary disks. It can be extended to the other research topics such as the statistical studies of the relation between the dust properties in the protoplanetary disks and the gap structures or the missing links between the gap structures and the morphology of the exoplanetary systems detected by various survey projects like the Kepler mission.

However, there are some limitations to the ALMA multiband analysis as well. First, I assume the vertical structure of the disk is homogeneous in the calculation but the real disks might have the gradient of temperature and/or density profiles along the vertical direction. Second, the frequency dependence of β is not taken into account in the calculation while the theoretical/experimental studies have reported the possible dependence of β on the frequency and temperature. For improving the ALMA multiband analysis, I need to update some assumptions for making a more realistic disk model in the calculation steps. If I make a parameter for taking into account the disk vertical structure of the temperature as $\rm T_{d,z} \propto T_{d,0}(\nu/\nu_0)^{\gamma}$ or the frequency dependence of β

as $\beta_\nu \propto \beta_0(\nu/\nu_0)^\gamma$, I need four bands to constrain the dust properties by the ALMA multiband analysis because the numbers of the unknowns and equations are increased as four from three. This is one of the good ways to improve the ALMA multiband analysis in the future.

Also, recent studies on the dust self-scattering effect in the optically thick region suggest that the optical depth can be dominated by the scattering opacity rather than the absorption opacity (e.g., Zhu et al. 2019). This effect is depending on the grain size distributions. Therefore, if I include this effect in the ALMA multiband analysis in the future, the results can provide evidence on the constraint of the dust grain sizes. Then, eventually, the improved ALMA multiband analysis can provide more accurate constraints on the dust properties which can be used as observational evidence for distinguishing the gap origins.

Bibliography

Akiyama, E., Muto, T., Kusakabe, N., et al. 2015, ApJ , 802, L17

Andre, P., & Montmerle, T. 1994, ApJ , 420, 837

Andre, P., Ward-Thompson, D., & Barsony, M. 1993, ApJ , 406, 122

Andrews, S. M., & Williams, J. P. 2007, ApJ , 659, 705

Andrews, S. M., Wilner, D. J., Espaillat, C., et al. 2011, ApJ , 732, 42

Andrews, S. M., Wilner, D. J., Hughes, A. M., Qi, C., & Dullemond, C. P. 2009, ApJ , 700, 1502

Andrews, S. M., Wilner, D. J., Hughes, A., et al. 2011, ApJ , 744, 162

Andrews, S. M., Wilner, D. J., Hughes, A. M., et al. 2012, ApJ , 744, 162

Andrews, S. M., Wilner, D. J., Zhu, Z., et al. 2016, ApJ , 820, L40

Andrews, S. M., Huang, J., Pérez, L. M., et al. 2018, ApJ , 869, L41

Armitage, P. J. 2010, Astrophysics of Planet Formation (Cambridge University Press)

—. 2015, ArXiv e-prints, arXiv:1509.06382

Attard, M., Houde, M., Novak, G., et al. 2009, ApJ , 702, 1584

Avenhaus, H., Quanz, S. P., Meyer, M. R., et al. 2014, ApJ , 790, 56

Bae, J., Zhu, Z., & Hartmann, L. 2017, ApJ , 850, 201

Batalha, N. M. 2014, Proceedings of the National Academy of Sciences, 111, 12647

Beaulieu, J. P., Bennett, D. P., Fouqué, P., et al. 2006, Nature, 439, 437

Beckwith, S. V. W., Henning, T., & Nakagawa, Y. 2000, Dust Properties and Assembly of Large Particles in Protoplanetary Disks (University of Arizona Press), 533, astro-ph/9902241

Beckwith, S. V. W., & Sargent, A. I. 1991, ApJ , 381, 250

Beckwith, S. V. W., Sargent, A. I., Chini, R. S., & Guesten, R. 1990, AJ , 99, 924

Benedict, G. F., McArthur, B. E., Forveille, T., et al. 2002, ApJ , 581, L115

Bergfors, C., Brandner, W., Daemgen, S., et al. 2012, MNRAS , 428, 182

Bergin, E. A., Cleeves, L. I., Gorti, U., et al. 2013, Nature, 493, 644

Birnstiel, T., Fang, M., & Johansen, A. 2016, Space Science Reviews, 205, 41

Birnstiel, T., Klahr, H., & Ercolano, B. 2012, A&A , 539, A148

Borucki, W. J., Koch, D., Basri, G., et al. 2010, Science, 327, 977

Bouvier, J., Bertout, C., Benz, W., & Mayor, M. 1986, A&A , 165, 110

Brauer, F., Dullemond, C. P., Johansen, A., et al. 2007, A&A , 469, 1169

Carpenter, J. M., Hillenbrand, L. A., Skrutskie, M. F., & Meyer, M. R. 2002, AJ , 124, 1001

Chiang, E. I., & Goldreich, P. 1997, ApJ , 490, 368

Chihara, H., Koike, C., Tsuchiyama, A., Tachibana, S., & Sakamoto, D. 2002, A&A , 391, 267

Cuzzi, J. N., Hogan, R. C., & Shariff, K. 2008, ApJ , 687, 1432

D'Alessio, P., Calvet, N., & Hartmann, L. 2001, ApJ , 553, 321

D'Alessio, P., Calvet, N., Hartmann, L., Franco-Hernández, R., & Servín, H. 2006, ApJ , 638, 314

D'Alessio, P., Cantö, J., Calvet, N., & Lizano, S. 1998, ApJ , 500, 411

D'Antona, F., & Mazzitelli, I. 1994, ApJS , 90, 467

de Juan Ovelar, M., Min, M., Dominik, C., et al. 2013, A&A , 560, A111

Debes, J. H., Poteet, C. A., Jang-Condell, H., et al. 2017, ApJ , 835, 205

Demyk, K., Meny, C., Lu, X.-H., et al. 2017a, A&A , 600, A123

Demyk, K., Meny, C., Leroux, H., et al. 2017b, A&A , 606, A50

Dong, R., & Fung, J. 2017, ApJ , 835, 146

Dong, R., Hall, C., Rice, K., & Chiang, E. 2015a, ApJ , 812, L32

Dong, R., Li, S., Chiang, E., & Li, H. 2017, ApJ , 843, 127

Dong, R., Zhu, Z., & Whitney, B. 2015b, ApJ , 809, 93

Dong, R., Rafikov, R., Zhu, Z., et al. 2012, ApJ , 750, 161

Draine, B. T. 2006, ApJ , 636, 1114

Dullemond, C. P., Hollenbach, D., Kamp, I., & D'Alessio, P. 2007, Models of the Structure and Evolution of Protoplanetary Disks (University of Arizona Press), 555–572, astro-ph/0602619

Dullemond, C. P., van Zadelhoff, G. J., & Natta, A. 2002, A&A , 389, 464

Eisner, J. A., Plambeck, R. L., Carpenter, J. M., et al. 2008, ApJ , 683, 304

Everett, M. E., Howell, S. B., Silva, D. R., & Szkody, P. 2013, ApJ , 771, 107

Favre, C., Cleeves, L. I., Bergin, E. A., Qi, C., & Blake, G. A. 2013, ApJ , 776, L38

Fedele, D., Tazzari, M., Booth, R., et al. 2018, A&A , 610, A24

Feigelson, E. D., Casanova, S., Montmerle, T., & Guibert, J. 1993, ApJ , 416, 623

Flock, M., Ruge, J. P., Dzyurkevich, N., et al. 2015, A&A , 574, A68

Frank, A., Ray, T., Cabrit, S., et al. 2014, Protostars and planets VI, 1, 451

Furlan, E., Watson, D. M., McClure, M. K., et al. 2009, ApJ , 703, 1964

Gaia Collaboration, Brown, A. G. A., Vallenari, A., et al. 2016, A&A , 595, A2

—. 2018, A&A , 616, A1

Gauvin, L. S., & Strom, K. M. 1992, ApJ , 385, 217

Girart, J. M., Rao, R., & Marrone, D. P. 2006, Science, 313, 812

Goldreich, P., & Tremaine, S. 1980, ApJ , 241, 425

Greene, T. P. 2001, American Scientist, 89, 316

Guenther, E. W., Esposito, M., Mundt, R., et al. 2007, A&A , 467, 1147

Guilloteau, S., Dutrey, A., Piétu, V., & Boehler, Y. 2011, A&A , 529, A105

Gundlach, B., Skorov, Y. V., & Blum, J. 2011, Icarus, 213, 710

Haikala, L. K., Harju, J., Mattila, K., & Toriseva, M. 2005, A&A , 431, 149

Haisch, Karl E., J., Lada, E. A., & Lada, C. J. 2001, ApJ , 553, L153

Hashimoto, J., Tsukagoshi, T., Brown, J. M., et al. 2015, ApJ , 799, 43

Heim, L.-O., Blum, J., Preuss, M., & Butt, H.-J. 1999, PhRvL, 83, 3328

Herbig, G. H. 1978, Some aspects of early stellar evolution that may be relevant to the origin of the solar system., ed. S. F. Dermott, 219–235

Hernández, J., Hartmann, L., Calvet, N., et al. 2008, ApJ , 686, 1195

Hernández, J., Hartmann, L., Megeath, T., et al. 2007, ApJ , 662, 1067

Huang, J., Andrews, S. M., Cleeves, L. I., et al. 2018, ApJ , 852, 122

Huang, Y. D., Morata, O., Koch, P. M., et al. 2016, in Proceedings of the SPIE, Vol. 9911, Modeling, Systems Engineering, and Project Management for Astronomy VI, 99111V

Hussain, G. A. J., Collier Cameron, A., Jardine, M. M., et al. 2009, MNRAS , 398, 189

Inoue, A. K., Oka, A., & Nakamoto, T. 2009, MNRAS , 393, 1377

Isella, A., Guidi, G., Testi, L., et al. 2016, PhRvL, 117, 251101

Isella, A., Huang, J., Andrews, S. M., et al. 2018, ApJ , 869, L49

Jang-Condell, H., & Turner, N. J. 2012, ApJ , 749, 153

Johansen, A., Klahr, H., & Henning, T. 2011, A&A , 529, A62

Johansen, A., & Youdin, A. 2007, ApJ , 662, 627

Kalas, P., Graham, J. R., Chiang, E., et al. 2008, Science, 322, 1345

Kanagawa, K. D., Muto, T., Tanaka, H., et al. 2016, PASJ , 68, 43

Kanagawa, K. D., Tanaka, H., Muto, T., & Tanigawa, T. 2017, PASJ , 69, 97

Kataoka, A., Tsukagoshi, T., Pohl, A., et al. 2017, ApJ , 844, L5

Kataoka, A., Muto, T., Momose, M., et al. 2015, ApJ , 809, 78

Keppler, M., Benisty, M., Müller, A., et al. 2018, A&A , 617, A44

Kim, S., Nomura, H., Tsukagoshi, T., Kawabe, R., & Muto, T. 2019, ApJ , 872, 179

Kim, S., Takahashi, S., Nomura, H., et al. 2020, ApJ , 888, 72

Kim, S.-H., Martin, P. G., & Hendry, P. D. 1994, ApJ , 422, 164

Kitamura, Y., Momose, M., Yokogawa, S., et al. 2002, ApJ , 581, 357

Koike, C., Mutschke, H., Suto, H., et al. 2006, A&A , 449, 583

Krist, J. E., Stapelfeldt, K. R., Ménard, F., Padgett, D. L., & Burrows, C. J. 2000, ApJ , 538, 793

Lada, C. J., & Wilking, B. A. 1984, ApJ , 287, 610

Laibe, G. 2013, MNRAS , 437, 3037

Latter, H. N., & Rosca, R. 2017, MNRAS , 464, 1923

Li, R., Youdin, A. N., & Simon, J. B. 2019, ApJ , 885, 69

Lin, D. N. C., & Papaloizou, J. 1979, MNRAS , 186, 799

Long, F., Herczeg, G. J., Pascucci, I., et al. 2017, ApJ , 844, 99

Long, F., Herczeg, G. J., Harsono, D., et al. 2019, ApJ , 882, 49

Loomis, R. A., Cleeves, L. I., Öberg, K. I., et al. 2018, ApJ , 859, 131

Luhman, K. L. 2004, ApJ , 602, 816

—. 2008, in Handbook of Star Forming Regions, ed. B. Reipurth, Vol. II (Astronomical Society of the Pacific), 169

Manara, C. F., Fedele, D., Herczeg, G. J., & Teixeira, P. S. 2016, A&A , 585, A136

Mangum, J. G., & Shirley, Y. L. 2017, PASP , 129, 069201

Matsuura, T., & Okuzumi, S. 2019, in AAS/Division for Extreme Solar Systems Abstracts, Vol. 51, AAS/Division for Extreme Solar Systems Abstracts, 324.08

Mayor, M., & Queloz, D. 1995, Nature, 378, 355

Meakin, P. 1991, Reviews of Geophysics, 29, 317

Mennella, V., Brucato, J. R., Colangeli, L., et al. 1998, ApJ , 496, 1058

Michikoshi, S., Kokubo, E., & Inutsuka, S.-i. 2012, ApJ , 746, 35

Min, M., Rab, C., Woitke, P., Dominik, C., & Ménard, F. 2016, A&A , 585, A13

Miyake, K., & Nakagawa, Y. 1993, Icarus, 106, 20

Morbidelli, A., & Raymond, S. N. 2016, Journal of Geophysical Research (Planets), 121, 1962

Müller, H. S. P., Thorwirth, S., Roth, D. A., & Winnewisser, G. 2001, A&A , 370, L49

Musiolik, G., Teiser, J., Jankowski, T., & Wurm, G. 2016a, ApJ , 818, 16

—. 2016b, ApJ , 827, 63

Natta, A., Meyer, M. R., & Beckwith, S. V. W. 2000, ApJ , 534, 838

Nomura, H., Tsukagoshi, T., Kawabe, R., et al. 2016, ApJ , 819, L7

Öberg, K. I., Qi, C., Fogel, J. K. J., et al. 2010, ApJ , 720, 480

—. 2011, ApJ , 734, 98

Okuzumi, S. 2009, ApJ , 698, 1122

Okuzumi, S., Momose, M., Sirono, S.-i., Kobayashi, H., & Tanaka, H. 2016, ApJ , 821, 82

Okuzumi, S., Tanaka, H., Kobayashi, H., & Wada, K. 2012, ApJ , 752, 106

Okuzumi, S., & Tazaki, R. 2019, ApJ , 878, 132

Ormel, C. W., & Liu, B. 2018, A&A , 615, A178

Pascucci, I., Testi, L., Herczeg, G. J., et al. 2016, ApJ , 831, 125

Pérez, L. M., Carpenter, J. M., Chandler, C. J., et al. 2012, ApJ , 760, L17

Pérez, L. M., Chandler, C. J., Isella, A., et al. 2015, ApJ , 813, 41

Pinilla, P., Birnstiel, T., Ricci, L., et al. 2012, A&A , 538, A114

Qi, C., D'Alessio, P., Öberg, K. I., et al. 2011, ApJ , 740, 84

Qi, C., Wilner, D. J., Aikawa, Y., Blake, G. A., & Hogerheijde, M. R. 2008, ApJ , 681, 1396

Qi, C., Ho, P. T., Wilner, D. J., et al. 2004, ApJ , 616, L11

Rapson, V. A., Kastner, J. H., Millar-Blanchaer, M. A., & Dong, R. 2015, ApJ , 815, L26

Reipurth, B., Pedrosa, A., & Lago, M. T. V. T. 1996, A&AS , 120, 229

Ribas, Á., Espaillat, C. C., Macías, E., et al. 2017, ApJ , 849, 63

Robrade, J., & Schmitt, J. H. M. M. 2006, A&A , 449, 737

Rosotti, G. P., Juhasz, A., Booth, R. A., & Clarke, C. J. 2016, MNRAS , 459, 2790

Safronov, V. S. 1972, Evolution of the Protoplanetary Cloud and Formation of the Earth and the Planets (Israel Program for Scientific Translations Jerusalem)

Santos, N. C., Israelian, G., Mayor, M., Rebolo, R., & Udry, S. 2003, A&A , 398, 363

Schegerer, A., Wolf, S., Voshchinnikov, N. V., Przygodda, F., & Kessler-Silacci, J. E. 2006, A&A , 456, 535

Schöier, F. L., van der Tak, F. F. S., van Dishoeck, E. F., & Black, J. H. 2005, A&A , 432, 369

Schwarz, K. R., Bergin, E. A., Cleeves, L. I., et al. 2016, ApJ , 823, 91

Seager, S. 2008, Exoplanet Transit Spectroscopy and Photometry, ed. O. Botta, J. Bada, J. Gómez Elvira, E. Javaux, F. Selsis, & R. Summons (Springer), 345

Shakura, N. I., & Sunyaev, R. A. 1973, A&A , 500, 33

Steinpilz, T., Teiser, J., & Wurm, G. 2019, ApJ , 874, 60

Sterzik, M. F., Alcalá, J. M., Covino, E., & Petr, M. G. 1999, A&A , 346, L41

Suyama, T., Wada, K., & Tanaka, H. 2008, ApJ , 684, 1310

Takahashi, S. Z., & Inutsuka, S.-i. 2014, ApJ , 794, 55

—. 2016, AJ , 152, 184

Takeuchi, T., & Lin, D. N. C. 2005, ApJ , 623, 482

Tanii, R., Itoh, Y., Kudo, T., et al. 2012, PASJ , 64, 124

Tazaki, R., Tanaka, H., Muto, T., Kataoka, A., & Okuzumi, S. 2019, MNRAS , 485, 4951

Tazzari, M., Testi, L., Ercolano, B., et al. 2016, A&A , 588, A53

Teague, R., Bae, J., Huang, J., & Bergin, E. A. 2019, ApJ , 884, L56

Teague, R., Henning, T., Guilloteau, S., et al. 2018, ApJ , 864, 133

Testi, L., Birnstiel, T., Ricci, L., et al. 2014, in Protostars and Planets VI, ed. H. Beuther, R. S. Klessen, C. P. Dullemond, & T. Henning, 339

Tominaga, R. T., Takahashi, S. Z., & Inutsuka, S.-i. 2019, ApJ , 881, 53

Toomre, A. 1964, ApJ , 139, 1217

Tsukagoshi, T., Nomura, H., Muto, T., et al. 2016, ApJ , 829, L35

Tsukagoshi, T., Muto, T., Nomura, H., et al. 2019, ApJ , 878, L8

Turner, N. J., Choukroun, M., Castillo-Rogez, J., & Bryden, G. 2012, ApJ , 748, 92

Ubach, C., Maddison, S. T., Wright, C. M., et al. 2012, MNRAS , 425, 3137

—. 2017, MNRAS , 466, 4083

Udry, S., & Santos, N. C. 2007, A&ARv , 45, 397

Varga, J., Ábrahám, P., Chen, L., et al. 2018, A&A , 617, A83

Villebrun, F., Alecian, E., Hussain, G., et al. 2019, A&A , 622, A72

Voirin, J., Manara, C. F., & Prusti, T. 2018, A&A , 610, A64

Wada, K., Tanaka, H., Suyama, T., Kimura, H., & Yamamoto, T. 2007, ApJ , 661, 320

—. 2008, ApJ , 677, 1296

—. 2009, ApJ , 702, 1490

Wagner, K., Follete, K. B., Close, L. M., et al. 2018, ApJ , 863, L8

Ward, W. R. 2000, On Planetesimal Formation: The Role of Collective Particle Behavior, ed. R. M. Canup & K. Righter (University of Arizona Press), 75–84

Warmels, R., Biggs, A., Cortes, P. A., et al. 2018, ALMA Technical Handbook, ALMA Doc. 6.3, Ver. 1.0 (ISBN 978-3-923524-66-2)

Weaver, E., Isella, A., & Boehler, Y. 2018, ApJ , 853, 113

Weidenschilling, S. J. 1977, Ap&SS , 51, 153

Weinberger, A. J., Becklin, E. E., Schneider, G., et al. 2002, ApJ , 566, 409

Whitney, B. A., Indebetouw, R., Bjorkman, J. E., & Wood, K. 2004, ApJ , 617, 1177

Whitney, B. A., Robitaille, T. P., Bjorkman, J. E., et al. 2013, ApJS , 207, 30

Whitney, B. A., Wood, K., Bjorkman, J. E., & Cohen, M. 2003a, ApJ , 598, 1079

Whitney, B. A., Wood, K., Bjorkman, J. E., & Wolff, M. J. 2003b, ApJ , 591, 1049

Whittet, D. C. B., Kirrane, T. M., Kilkenny, D., et al. 1987, MNRAS , 224, 497

Woitke, P., Min, M., Pinte, C., et al. 2016, A&A , 586, A103

Wood, K., Wolff, M. J., Bjorkman, J. E., & Whitney, B. 2002, ApJ , 564, 887

Yamamoto, S. 2017, Introduction to Astrochemistry: Chemical Evolution from Interstellar Clouds to Star and Planet Formation (Springer)

Yang, C. C., Johansen, A., & Carrera, D. 2017, A&A , 606, A80

Youdin, A. N. 2011, ApJ , 731, 99

Zhang, K., Blake, G. A., & Bergin, E. A. 2015, ApJ , 806, L7

Zhu, Z., Nelson, R. P., Dong, R., Espaillat, C., & Hartmann, L. 2012, ApJ , 755, 6

Zhu, Z., Zhang, S., Jiang, Y.-F., et al. 2019, ApJ , 877, L18

Zuckerman, B., Webb, R., Schwartz, M., & Becklin, E. 2001, ApJ , 549, L233